# COMMUNICATION AND SYNCHRONIZATION OF CIRCADIAN RHYTHM IN NEUROSPORA CRASSA

by

XIAO QIU

(Under the Direction of Jonathan Arnold)

## ABSTRACT

A “big chamber” microfluidic experiment as well as a microfluidic experiment were designed to demonstrate that communication existed among cells. At the macroscopic limit (~150,000 cells), there was a high degree of phase synchronization between cells in the artificial tissue. In the microwell experiment, single cells in individual wells showing phase synchronization provided strong evidence for the quorum sensing hypothesis and some information about the communication parameters that quantitate quorum sensing. The measurement of averages over single cell trajectories in the microwell device supported a deterministic quorum sensing model identified by ensemble methods for clock phase synchronization. A strong inference framework was used to test the communication mechanism in phase synchronization of quorum sensing versus cell-to-cell contact, suggesting support for quorum sensing. In addition, a microfluidic chip with serpentine channels was fabricated to capture individual hypha. Fluorescence of a mCherry recorder gene driven by a clock-controlled gene-2 promoter (ccg-2p) was measured simultaneously along hyphae for every half an hour for at least 6 days. Furthermore, hyphae also displayed temperature compensation properties, where the period of oscillations were stable over a physiological range of temperatures from 24 °C to

30 °C (Q 10 = 1.00-1.10). Hyphae tracked in individual serpentine channels were highly synchronized (K=0.60-0.78). A clock model developed was able to mimic hyphal growth observed in the serpentine chip. Finally, a density-dependent metabolic switch model involving in Ethanol production in a qa-x background in Neurospora crassa was developed to test whether available RNA profiling and Continuous in vivo Metabolism-NMR data are consistent with the hypotheses that: (1) quorum sensing (QS) in Ethanol production is the QS mechanism in phase synchronization of the clock; (2) the QS signal is (are) an aromatic alcohol(s); (3) the gene (NCU03643) encodes the quorum sensing regulator. Ensemble methods were used to fit this hypothesis successfully to RNA profiling and CIVM-NMR data in four experiments at high and low density in qa-x and Wildtype genetic backgrounds. In this way a detailed biochemical mechanism is put forward to explain the phase synchronization of single cells in Neurospora crassa.

INDEX WORDS: Neurospora crassa, circadian rhythm, phase synchronization, single cells, hyphae, metabolism, quorum sensing, signaling molecule

# COMMUNICATION AND SYNCHRONIZATION OF CIRCADIAN RHYTHM IN NEUROSPORA CRASSA

by

XIAO QIU

BS, Tongji University, 2011

MS, Shanghai Institute of applied mathematics and mechanics, 2015

A Dissertation Submitted to the Graduate Faculty of The University of Georgia in Partial Fulfillment of the Requirements for the Degree

DOCTOR OF PHILOSOPHY

ATHENS, GEORGIA

2022

# COMMUNICATION AND SYNCHRONIZATION OF CIRCADIAN RHYTHM IN NEUROSPORA CRASSA

by

XIAO QIU

| | |
|---|---|
| Major Professor: | Jonathan Arnold |
| Committee: | Leidong Mao |
| | Heinz-Bernd Schuttler |
| | Arthur Edison |

Electronic Version Approved:

Ron Walcott
Vice Provost for Graduate Education and Dean of the Graduate School
The University of Georgia
August 2022

ACKNOWLEDGEMENTS

First, I would like to express my special thanks to Dr. Mao and Dr. Arnold, who offered me this great opportunity to do single cell study in their lab and guided me over the past five years. Dr. Mao helped me a lot in doing the image process and gave me tuns of great suggestions on single cell tracking. Dr. Arnold helped me a lot involving in building models, trouble shooting for running models, and paper writing. Without their help and support, it would be impossible for me to finish my degree in five years. In addition, I would like to thank Dr. Schuttler. Dr. Schuttler helped me a lot in building the ensemble models and gave me a lot of super helpful suggestions on my code debugging. And I truly appreciate Dr. Edison as he helped me a lot in building the metabolic switch model. Next, I would like to say thanks to my great labmate and my best friend, Jiahui Cheong. Without you great effort, my research is just a pie in the sky. Finally, I would like to express my gratefulness to my father Weiqing Qiu, my mother Qiuqing Zhu, and my girlfriend Zehua Cui for their continuous and endless support for me.

TABLE OF CONTENTS

Page

ACKNOWLEDGEMENTS ..... iv

LIST OF TABLES ..... viii

LIST OF FIGURES ..... ix

CHAPTER

1 INTRODUCTION ..... 1

2 THE MACROSCOPIC LIMIT TO SYNCHRONIZATION OF CELLULAR CLOCKS IN SINGLE CELLS OF NEUROSPORA CRASSA ..... 6

Abstract ..... 7

Significance ..... 7

Results ..... 13

Discussion ..... 40

Conclusion ..... 43

Materials and Methods ..... 44

3 THE CLOCK IN GROWING HYPHAE AND THEIR SYNCHONIZATION IN NEUROSPORA CRASSA ..... 49

Abstract ..... 50

Significance ..... 50

Results ..... 54

Discussion ..... 81

Conclusion .....83
Materials and Methods .....84
4 IN VIVO METABOLOMIC AND RNA PROFILING DATA SUPPORT AN AROMATIC ALCOHOL AS A QUORUM SENSNING SIGNAL FOR PHASE SYNCHRONIZATION OF THE CLOCK IN SINGLE CELLS OF NEUROSPORA CRASSA .....89
Abstract .....90
Significance .....90
Model .....93
Results .....96
Discussion .....109
Conclusion .....110
Materials and Methods .....111
5 CONCLUSIONS .....113
REFERENCES .....115
APPENDICES
A SUPPLEMENTARY MATERIALS FOR THE MACROSCOPIC LIMIT TO SYNCHRONIZATION OF CELLULAR CLOCKS IN SINGLE CELLS OF NEUROSPORA CASSA .....124
B SUPPLEMENTARY MATERIALS FOR THE CLOCK IN GROWING HYPHAE AND THEIR SYNCHONIZATION IN NEUROSPORA CRASSA .....130
C SUPPLEMENTARY MATERIALS FOR IN VIVO METABOLOMIC AND RNA PROFILING DATA SUPPORT AN AROMATIC ALCOHOL AS A QUORUM

SENSNING SIGNAL FOR PHASE SYNCHRONIZATION OF THE CLOCK IN SINGLE CELLS OF NEUROSPORA CRASSA.....137

LIST OF TABLES

Page

Table 1.1: Measures of synchronization (K) between 5 different fields of view (FOV) along a transect through the artificial tissue in Fig. 3a exceed 0.97 using the Kuramoto K .....17

Table 1.2: The moments of the rate constants across the ensemble for the quorum sensing hypothesis derived from a microwell experiment. .....28

Table 2.1: The signal to noise ratio of a bundle of hyphae overlapped with that of race tubes with a luminescent strain.....67

Table 2.2: Measures of synchronization (K) between 6 segments of different serpentine channels along the serpentine chip .....71

Table 2.3: Temperature Coefficient $Q_{10}$ over a physiological range of temperatures (T1) provided evidence of temperature compensation. Standard Errors (SE) for temperature coefficient were computed using the propagation of error method .....74

Table S1.1: The rate constants for the quorum sensing (column 3) are similar to isolated single cells[1] (column 2) and those at the macroscopic limit of $10^7$cells per ml[2] (column 4) .....124

Table S3.1: The rate coefficients of the quorum sensing model as null hypothesis are tabulated. Ensemble means and ensemble standard errors are reported for each rate coefficient in Fig. 3.1 .....137

LIST OF FIGURES

Page

Figure 1.1: Two microfluidic devices .....11

Figure 1.2: Periodogram of experiments done with MFNC9[3] conidial cells placed in different media solutions while running a 10 day long experiment in the big chamber microfluidic device .....13

Figure 1.3: Pairwise phase trajectories of 5 fields of view in a transect across the artificial tissue in the big chamber device are highly correlated. Cells were grown in Media 5.....15

Figure 1.4: The trajectories of [CCG-2] fluorescence over all 5 fields of view in Fig. 3a aligned almost perfectly.....16

Figure 1.5: Quorum sensing and contact models for synchronizing clocks in single cells .....19

Figure 1.6: Data from CCG-2 trajectories fitted to an ensemble of deterministic model.....23

Figure 1.7: The model ensemble fitted to fluorescence of MFNC9[3] cells with a *ccg-2* promoter in the microwell device averaged over two clusters of single cell trajectories initially with different phase (Fig. 3a) supported the quorum sensing hypothesis in a MCMC experiment.....26

Figure 1.8: Periodogram or power spectrum of clock mutants and the noise model control .....30

Figure 1.9: The model ensemble fitted to fluorescence of MFNC9[3] cells with a *ccg-2* promoter in the microwell device integrated over two fields of view (Fig. 3a) did not support the contact model in a MCMC experiment.....33

Figure 1.10: The standard error in fluorescence of single cells is significantly higher than that of multiple cells in the microwell device .....35
Figure 1.11: Microwell-based microfluidic chip with varying cell density gradient .....36
Figure 2.1: Schematic representation of experimental setup for the acquisition of fluorescence signal from serpentine chip .....53
Figure 2.2: A growing hypha idealized as a cylinder is shown above with the velocity distribution of nuclei along the hypha shown below .....56
Figure 2.3: Genetic network for the clock in *N. crassa* .....59
Figure 2.4: Fluorescent images of hyphae stained with calcofluor white demarcate 1-4 hyphae in a channel .....61
Figure 2.5: Several hyphal tracking methods were developed with CellProfiler .....63
Figure 2.6: A single hypha of MFNC9 .....66
Figure 2.7: Fluorescence intensity pattern varies along positions in the serpentine channel .....68
Figure 2.8: Single hyphae display temperature compensation properties .....72
Figure 2.9: Light-dark (L/D) entrainment detrended fluorescent intensity data.....75
Figure 2.10: Overview of velocity profiles obtained with nuclei tracking in serpentine channel .76
Figure 2.11: The nuclear density, velocity profile, and food distribution .....79
Figure 2.12: The hyphal clock model displays the “bands” observed in race tubes and the periodicity of the serpentine device .....80
Figure 2.13: Microfluidic platform that was used to track hyphae growth .....85
Figure 3.1: Metabolic model with allosteric clock regulation .....92
Figure 3.2: The Monte Carlo Experiment to fit the quorum sensing model to 1128 mRNA and metabolite measurements appears well equilibrated.....95

Figure 3.3: The RNA profiles of the *qa* gene cluster are well fitted by the quorum sensing model for all for experiments on the *qa-x* mutant at low (a) and high density (b) .....100

Figure 3.4: The observed metabolic profiles by CIVM-NMR (dotted lines) for 8 metabolites in a *qa-x* mutant at low density are well fitted by the quorum sensing model (solid lines) ...101

Figure 3.5: The observed metabolic profiles from CIVM-NMR (dotted lines) for 8 metabolites in a *qa-x* mutant at high density are well fitted by the quorum sensing model .....102

Figure 3.6: The RNA profiles (dotted lines) for the *qa* cluster genes in WT are well fitted by the null hypothesis of the quorum sensing model (solid lines) by the same rate coefficients at (a) low and (b) high density .....103

Figure 3.7: The metabolic profiles from CIVM-NMR for 8 metabolites in WT at low density are well fitted by the quorum sensing model (Fig. 1).....104

Figure 3.8: The metabolic profiles from CIVM-NMR for 8 metabolites in WT at high density are well fitted by the quorum sensing model (Fig. 1).....105

Figure 3.9: The RNA profiling data and CIVM-NMR data are consistent with *qa-x* being a structural gene in QA metabolism as in Fig. 1 or as an alternative regulator of QA metabolism.....107

Figure 3.10: There is little to distinguish among aromatic alcohols as a quorum sensing signal based on the overlapping chi-squared distributions across the ensembles for each hypothesis with the signal being: (T) Tyrosol (null hypothesis); (Tr) Tryptophol; or (P) Phenylethanol.....108

Figure S1.1: Mean single cell trajectories from the chamber microfluidic device tracked the whole field of view average intensity very well .....126

Figure S1.2: Average Phase of single cells tracks phase of a field of view across 10 fields of view in the big chamber device .....127
Figure S1.3: While the phase curves do track each other, they also fan out over time .....128
Figure S1.4: There is limited information about the diffusion parameters ($\eta$ and $\eta_{ext}$) for communication under the quorum sensing model as indicated by the chi-squared statistic surface as a function of $\eta$ and $\eta_{ext}$. .....129
Figure S2.1: Numerical simulation of flow profiles within the channels using COMSOL Multiphysics software.....130
Figure S2.2: Fluorescence trajectories of three individual hyphal tips tracked.....131
Figure S2.3: Fluorescence trajectories of seven individual segments of hyphae in serpentine channels.....132
Figure S2.4: Fluorescence trajectories of four individual of hyphae in serpentine channels .....133
Figure S2.5: Image of luminescence band in a race tube[4]. .....134
Figure S2.6: Image of the segment (segment 2) consisting of six serpentine channels tracked to calculate Kuramoto K values in Table 2.2.....135
Figure S2.7: Hilbert phase of 127 trajectories of generated white noise for a period of 240h ....136
Figure S3.1: Metabolic model with QA-X as a regulator.....142
Figure S3.2: Metabolic model with phenylethanol as signaling molecule .....143
Figure S3.3: Metabolic model with tryptophol as signaling molecule .....144
Figure S3.4: Ensemble simulation result for Tyrosol .....145

# CHAPTER 1

# INTRODUCTION

Collective behavior is a form of social behavior involving the coordinated behavior of large group of similar individuals without central coordination. It occurs on a variety of scales of biological organization from fish schooling to human gathering, and from bees swarming to swimming bacteria[5]. Single-celled bacteria and fungi collectively detect chemical signals generated by close neighbors to synchronize their motion. The study of synchronization of circadian rhythm in single cells constitutes building blocks of understanding collective behavior.

Circadian rhythm is a roughly 24-hour cycle in the physiological process of most living things, including animals, plants, and microbes [6]. It responds to light and dark primarily and is regulated by biological clocks which are organisms' natural timing devices. Circadian rhythm is central to many cellular activities such as carbon metabolism and cell cycle, and is the internal clock in our bodies that is linked to biological activities such as sleeping and feeding patterns, hormone production, cell regeneration, and etc. [7,8]. Changes in our body and environmental factors can affect our circadian rhythms and cause the natural light-dark cycle to be out of synchronization. And abrupt changes to circadian rhythms in our body can result in the dysfunction of metabolic pathways, and may lead to many diseases such as cancer, cardiovascular diseases, diabetes, obesity, and metabolic syndrome. Circadian rhythms also play a part in the reticular activating system, which is crucial for maintaining a state of consciousness. A reversal in the sleep–wake cycle may be a sign or complication of uremia or azotemia [9,10]. It is essential for us to gain more insight

regarding genes that are responsible for circadian rhythms to significantly advance treatment and therapy for these diseases associated with circadian rhythms. Detailed understanding of circadian rhythms would also be crucial to maximize the efficiency of drugs and treatments for diseases [11].

Much of what we know about circadian rhythms at the molecular levels comes from the study of *Neurospora crassa*. *Neurospora crassa* is a type of red bread mold of the phylum Ascomycota. It is widely used as a model organism because it is easy to grow and has a haploid life cycle that makes genetic analysis simple. Most measurements on the biological clock of *Neurospora crassa* are made on millions of cells to understand the mechanism of telling time [12].

Previously, many studies have been done on cell communication at the macroscopic level [13], but few have been done so on the single cell level. Single cell analysis is becoming a primary research method to study how circadian rhythms affect our biological clock [14-16]. Preliminary data indicates that single cells of *Neurospora crassa* do have an intrinsic rhythm, but it tends to be very noisy and stochastic [17,18]. However, when the circadian rhythms of small (2-3 cell) clusters are observed, there is a noticeable increase of the signal-to-noise ratio in the system. Recent researchers have shown that both communication hypothesis and stochastic resonance are viable for explaining the phase synchronization in single cells [18-20], and here we want to focus on how the communication mechanism of individual cells help to sidestep the stochastic and damping behaviors of single cells using existing experimental equipment[21]. **This knowledge is important to fully understand:**

**1) How do single cells communicate to overcome their stochasticity and synchronize their circadian rhythm with each other?**

**2) Do growing cells have a clock and can these cells synchronize their circadian rhythm with each other?**

**3) What is the signaling molecule that single cells use to communicate with each other and how does the signaling molecule affect the clock?**

Here we introduce novel microfluidics platforms to address these challenges. Microfluidic techniques provide a feasible and efficient way to conduct research on the single cell level[17]. By using new microfluidic technology, individual cells are encapsulated in microwells or chambers, and tagged with a fluorescent protein, providing scientists with a stable platform to track tens of thousands of cells with single-cell precision [17,18]. This technology allows us to collect data on thousands of single cells simultaneously for up to 10 days, while in the past scientists were only able to gather averaged data from individual cells for approximately 48 hours [22]. A serpentine device is also designed and fabricated in our research to isolate the growing filaments in single serpentine channels to study the communication and synchronization of growing filaments of *Neurospora crassa* on the single filament level.

The objective of this research is to investigate how single cells of the model filamentous fungus, Neurospora crassa, synchronize their circadian rhythm as a first step to the same problem in more complex eukaryotes with a clock. With a good understanding of the circadian rhythm of cells, we can apply our findings to many areas such as exploiting the biological clock of algae to make biofuel reactors more efficient [23,24], understanding the synchronization phenomenon of agricultural pests such as locusts to control them [25], as well as increasing the efficacy of medical treatment in human beings and reducing drug toxicity or adverse reactions dependent on time of

delivery of pharmaceuticals [26]. The research is based on preliminary data demonstrating that: 1) the genetic network of *Neurospora crassa* can be used to study the synchronization of single cells; 2) single cells of *N. crassa* do have a clock [18]. Based on these data, **the central hypothesis is that single cells of *Neurospora crassa* communicate and synchronize with each other through exchanging certain signaling molecules.** There are two paths that a signal molecule can take from one cell to another. The first path is that the signal molecule diffuses directly from one cell to the other cell. The second path is that the signal molecule first diffuses from the intracellular space to the extracellular space, and then diffuses from the extracellular space into intracellular space. In this research, we define the two communication mechanisms in single cells as direct contact communication and quorum sensing communication, respectively.

To fully understand the communication and synchronization mechanism of ***Neurospora crassa***, we choose numerical simulations combined with controlled laboratory experiments as our method. The following is the structure of this dissertation:

1) Studying the communication and synchronization of single cells of ***Neurospora crassa*** using a quorum sensing genetic network and a contact genetic network, and ensemble simulation method. A microwell microfluidic device to trap individual cells is designed and fabricated to study single cells communication and synchronization and test the quorum sensing model versus the contact model.
2) A filament model of ***Neurospora crassa*** is developed to simulate the communication and synchronization of circadian rhythm in growing filaments of ***Neurospora crassa***. A serpentine device to isolate filaments is designed and fabricated to study the communication and synchronization of growing filaments of ***Neurospora crassa.***

3) A metabolic switch model is developed to simulate the qa metabolic pathway in ***Neurospora crassa*** to find out the potential signaling molecule that single cells use to communicate with each other, and to understand how the signaling molecule involves in phase synchronization of the clock.

# CHAPTER 2

# THE MACROSCOPIC LIMIT TO SYNCHRONIZATION OF CELLULAR CLOCKS IN SINGLE CELLS OF NEUROSPORA CRASSA[27]

[27] Qiu, X., Cheong J H, et al. (2022) (Scientific Report) 12(1): 1-19. Reprinted here with permission of the publisher.

**Abstract**. We determined the macroscopic limit for phase synchronization of cellular clocks in an artificial tissue created by a "big chamber" microfluidic device to be about 150,000 cells or less. The dimensions of the microfluidic chamber allowed us to calculate an upper limit on the radius of a hypothesized quorum sensing signal molecule of 13.05 nm using a diffusion approximation for signal travel within the device. The use of a second microwell microfluidic device allowed the refinement of the macroscopic limit to a cell density of 2166 cells per fixed area of the device for phase synchronization. The measurement of averages over single cell trajectories in the microwell device supported a deterministic quorum sensing model identified by ensemble methods for clock phase synchronization. A strong inference framework was used to test the communication mechanism in phase synchronization of quorum sensing versus cell-to-cell contact, suggesting support for quorum sensing. Further evidence came from showing phase synchronization was density dependent.

**Significance**. Describing and explaining the emergence of coherence in biological oscillators is a central unsolved problem in Collective Behavior[28]. Using microfluidics, the authors have experimentally described when the synchronization process happens as noisy single cell oscillators transition to the macroscopic limit of tissues and whole organisms. Using an artificial tissue created by microfluidics the authors observed how the clocks in single cells transitioned to a deterministic, macroscopic limit. This limit was refined by a second microwell device, which provided phase information about the oscillators through single cell tracking. Both microscopic single cell data together with macroscopic data integrated over the field of view on an artificial tissue were used to document the synchronization process. The macroscopic data identified two communication mechanisms that are possible with earlier macroscopic data from a variety of

sources including RNA profiling, protein profiling, and physiological measurements on the clock through race tubes. A strong inference framework was used to test quorum sensing vs. a contact model of communication underlying phase synchronization of cellular clocks.[29] The approaches here provide a model for a method to use single cell data to explain emergent properties of tissues and whole organisms, such as circadian rhythms, and a test of two mechanisms of coherence between cellular oscillators at the macroscopic limit.

Collective behavior occurs on a variety of scales of biological organization, from the collective attack of viruses on bacterial cells[30] and synchronization of clocks in single cells[31] to collective behavior of flocks[32], schools[33], herds[34], troops of primates[35], and whole communities of organisms[36]. Some forms of collective behavior lead to synchronized oscillations, whether the system is cells synchronizing their clocks or fire flies synchronizing their flashing[37]. A fundamental problem in collective behavior is understanding the synchronization of biological oscillators[28]. The focus here is on the phase synchronization of clocks in single cells[31]; the problem of understanding synchronized oscillators arises in the study of other signaling systems as well[38,39]. At the single cell level there is substantial stochastic intercellular variation in the phase of cellular clocks[17], but as these cells transition to the macroscopic limit of $10^7$ cells per milliliter (ml), the clocks become synchronized and display coherent circadian rhythms on the macroscopic scale of $10^7$ cells/ml[2,4]. Our goal here is to understand both experimentally and theoretically how this phase transition to synchronized behavior takes place in moving from cells to tissues to whole organisms[21,40].

There are a variety of theories on how this transition to the macroscopic limit takes place. One hypothesis is that some form of cellular communication, such as quorum sensing[41-43] or cell-to-cell contact[44], allows the clocks in different cells to synchronize[45]. Models have been proposed for how this might happen[46-48]. A second possibility is that stochastic intracellular noise plays a positive role in synchronization[49]. In previous work it has been demonstrated that stochastic intracellular noise can lead to periodic behavior[50,51], but these models do not address subsequent synchronization of oscillators. There is a possibility that noise could play a positive role in synchronizing the cellular clocks with respect to their phase when genetically identical cells share a common random environment as a synchronizing agent[52]. This hypothesis converges on a physical hypothesis known as Stochastic Resonance[19], in which stochastic intracellular noise helps to solidify periodic behavior as well as oscillator synchronization. One of the earliest examples of invoking Stochastic Resonance to explain the origin of the clock is in the model clock system, *Neurospora crassa*[53]. Recently in the same clock system it has been shown from single cell data that there is one stochastic resonance predicted under a variety of Light/Dark regimens[1,54].

The advent of microfluidics[55] allows researchers to capture and manipulate single cells to address experimentally the problem of cellular synchronization[36,56]. In order to study this interesting phase transition from cells with substantial phase variation[31] to a state of substantial phase locking, two microfluidic platforms (Fig. 1.1), the “big chamber device” and microwell device, were developed. The purpose of the big chamber device was to reproduce the transition in synchronization behavior of conidial cells at the macroscopic limit of $10^7$/ml. Nakashima[22] developed the liquid culture assay used in most molecular studies of the clock in *Neurospora*

*crassa*[57-60]. The definition of the macroscopic limit used here throughout is reproducing the behavior of these Nakashima liquid cultures and the synchronization of the cellular oscillators in such cultures. One of the features of these liquid conidial cultures is that the clock at the macroscopic limit can only be observed over a 48-hour (h) window (Fig. 1.1d). On the micro-scale of single cells this limit on observation of circadian rhythms over 48 h can be removed fortunately[17]. The big chamber device also provides information about the size of the signaling molecule as discussed below. The purpose of the second microwell device (Fig. 1.1e-f) in contrast allows tracking of the oscillations of individual cells over 10 days and the manipulation of the conidial cell environment, such as density. In this way a more detailed study of phase synchronization can be made over 240 h.

First, the big chamber device was used to pack conidial cells of the model clock system (Fig. 1.1b), *N. crassa*, into one artificial tissue so that the emergence of circadian rhythms could be studied both macroscopically and microscopically simultaneously. The media was selected to minimize formation of filaments and cell fusion to simplify the modes of communication between cells[17,61]. The purpose of this report is to characterize this transition from disorder to order in an ensemble of cellular clocks in an artificial tissue. In previous work evidence was provided that single conidial cells have clocks and that most of their stochastic intracellular variation was in phase[31]. Using a second microwell device, in one experiment three hypotheses are tested: (1) phase synchronization; (2) density effect on phase synchronization; (3) contact model hypothesis. We demonstrate that phase synchronization takes no more than 829 cells or a cell density of 2166 cells per fixed area of the device and is density-dependent. Contact hypothesis is also evaluated as an alternative to quorum sensing. Two models for how this phase

synchronization takes place are developed, evaluated, and compared against the aggregate behavior of cells in this artificial tissue or in a microwell device. This would allow us to make more refined predictions on when phase synchronization would occur to guide future microfluidic experiments[2].

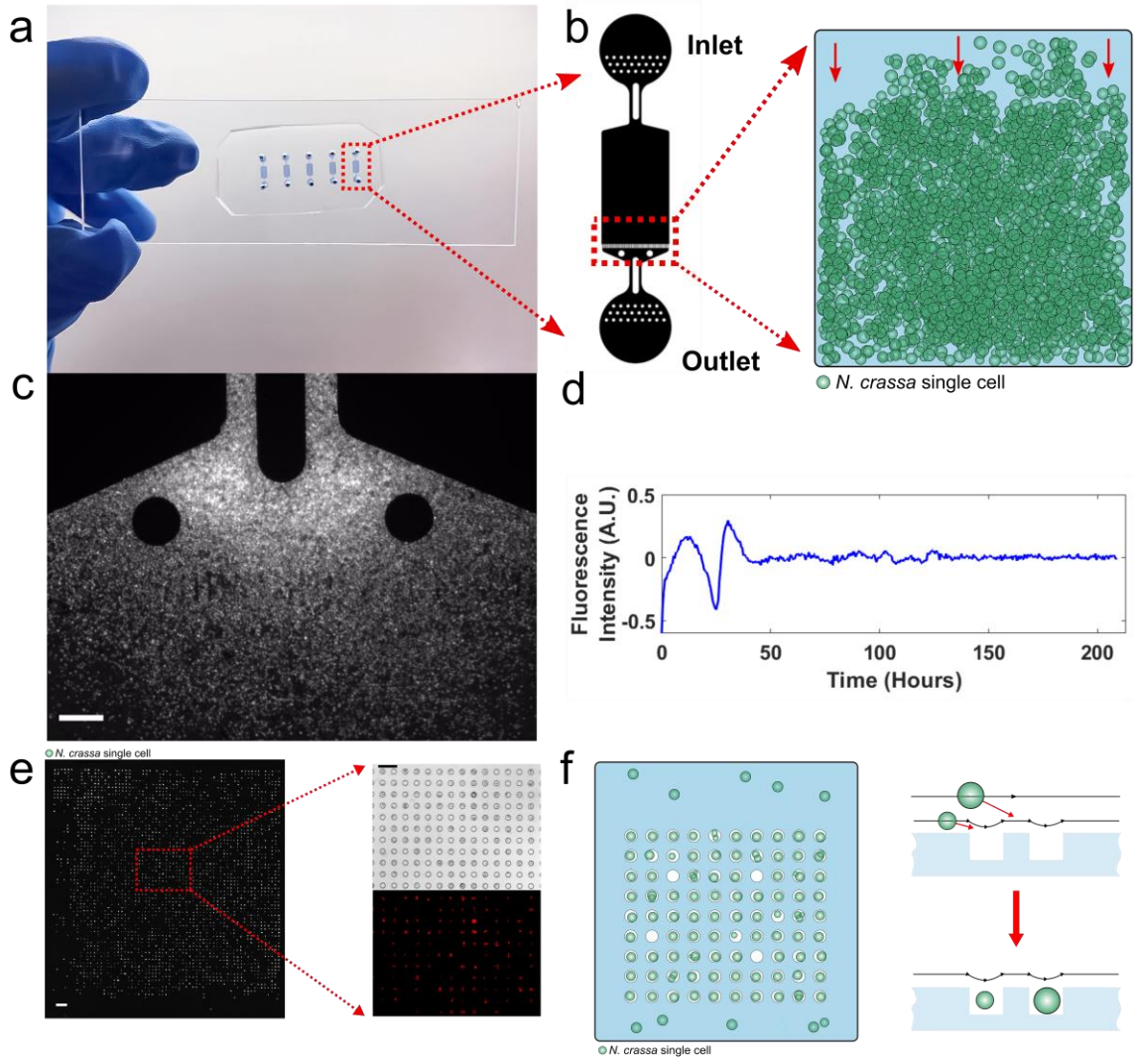


**Fig. 1.1** Two microfluidic devices, the "big chamber device" and microwell device, are used to characterize the synchronization of cellular oscillators on the macro-scale and micro-scale. A microfluidic "big chamber device" is developed to pack ~150,000 cells into an artificial tissue to

examine the macroscopic limit to synchronization of cellular clocks in media 5[17]. The big chamber enables the fluorescence detection of conidial cells (strain MFNC9[3]) through an mCherry recorder driven by *clock-controlled gene-2* (*ccg-2*) promoter both in aggregate and individually[3]. Time fluorescence measurements were taken every half hour over 10 days. **(a**) An image of a microfluidic device that houses 5 big chamber devices for experiments. (**b**) Schematic of the big chamber device consisting of an inlet and outlet where cells (green circles) flow into the device from the inlet end and are gradually trapped at the barriers present at the outlet end. The dimensions of a main chamber are 1800 x 1150 x 10 (height) $\mu m$. (**c**) Fluorescence image of the cells trapped in the big chamber device. Scale bar: 50$\mu m$. (**d**) The detrended fluorescence for around 140,000 cells is shown over 209 h. **The plots were created in MATLAB_R2020B (**https://www.mathworks.com/products/matlab.html). (e) A microwell microfluidic device to trap individual cells is constructed to test the quorum sensing model versus the contact model. Left: fluorescence image of MFNC9 cells in the microwell device. Scale bar: 100µm. Right: visualization of MFNC9 cells trapped in individual microwells at 20x magnification. (Top: bright field; bottom: fluorescence). Scale bar: 50µm. (**f)** Schematic of cells (in green) seeded in individual microwells of 10µm in diameter.

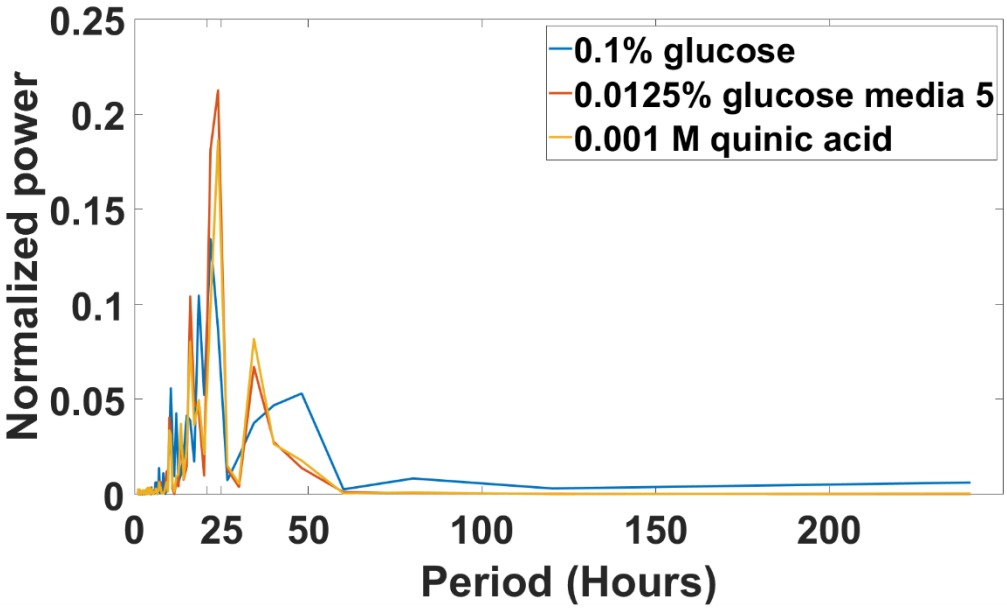


**Fig. 1.2** Periodogram of experiments done with MFNC9[3] conidial cells placed in different media solutions while running a 10 day long experiment in the big chamber microfluidic device. Periodograms were generated with ~145,000 cells for each experiment. **The plots were created in MATLAB_R2020B (**https://www.mathworks.com/products/matlab.html).

**Results**

**Packing single cells into an artificial tissue with a "big chamber" microfluidic device.**

In order to determine experimentally the macroscopic limit to the synchronization of cellular clocks, a "big chamber" microfluidic device with chamber dimensions 1800 x 1150 x 10 (height) $\mu m$ was designed (Fig. 1.1a). The device trapped ~150,000 cells near a barrier to create an artificial tissue (Fig. 1.1c). Both fluorescence measurements on individual cells and aggregate measurements on five fields of view with ~1700 cells each were obtained. What is remarkable is that time-lapse photography (supplementary video) demonstrated circadian rhythms to the naked eye. The video is summarized in Fig. 1.1d, showing the circadian rhythm with period of 21 h in

agreement to race tube experiments and liquid culture experiments beyond the macroscopic limit[2]; moreover, the oscillations are limited to 2 periods as in Nakashima liquid cultures[22] (Fig. 1.1d). Aggregation of cells over fields of view and over individual cells yielded similar estimates of the period as well as the Hilbert phase curves (see Materials and Methods) (supplementary Fig. S1.1). Three different media for conidial growth were tried in the big chamber with similar results (Fig. 1.2).

**The artificial tissue has about ~150,000 cells and places an upper limit of 13.5 nm on a hypothesized quorum sensing signal molecule's radius for cellular clock synchronization.**

From the supplementary video and supplementary Fig. S1.2 and S1.3 it is clear that we are obtaining synchronized oscillations by cells over the dimensions of the device (1800 x 1150 x 10 $\mu m$). This synchronous behavior is captured in the phase trajectories of a fluorescent strain MFNC9 with a mCherry recorder fused to the *clock-controlled gene*-2 promoter (ccg-2P)[3] (see Materials and Methods for calculating phase) across different fields of view of the artificial tissue (Fig. 1.3)[62].

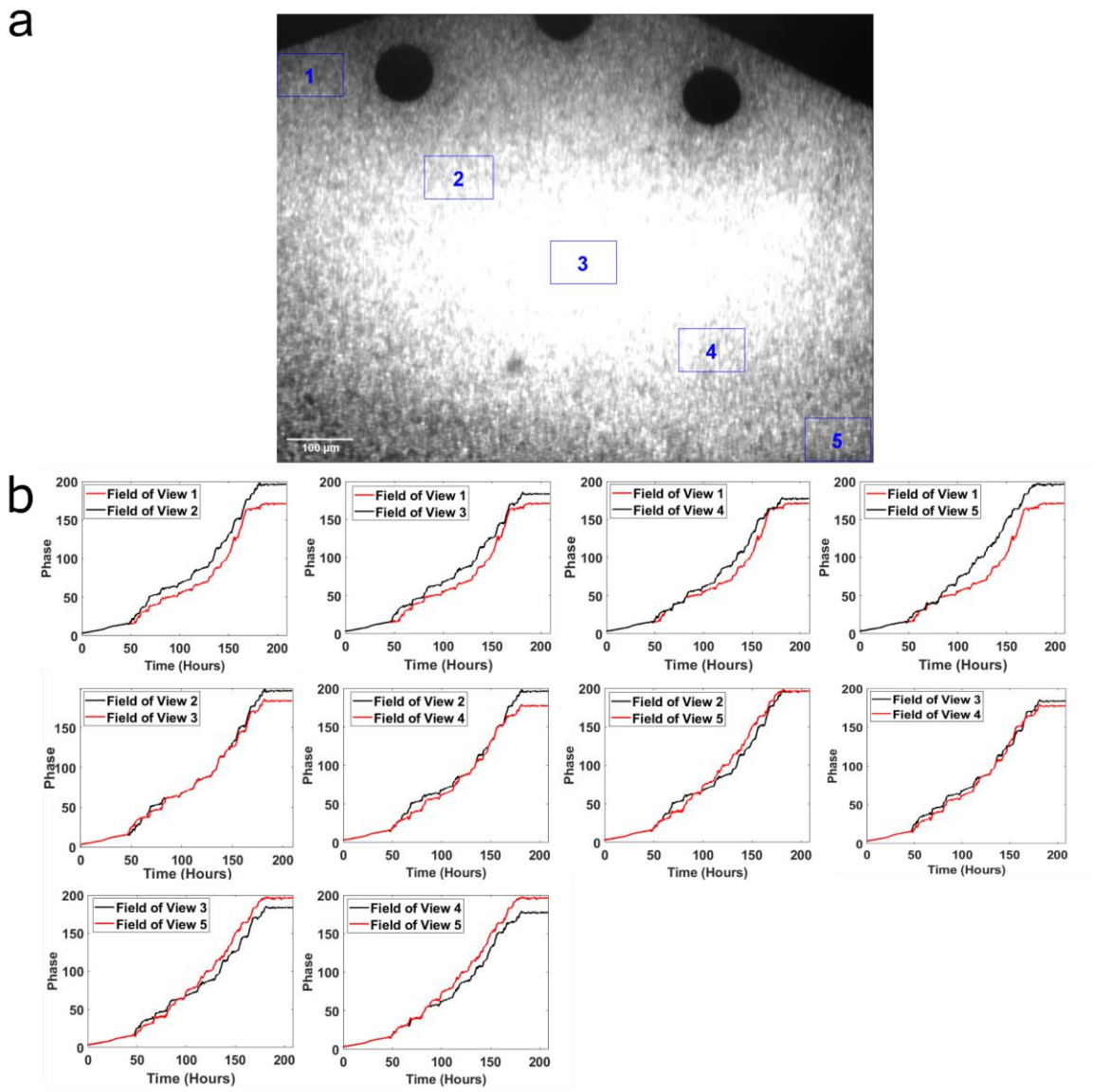


**Fig. 1.3** Pairwise phase trajectories of 5 fields of view in a transect across the artificial tissue in the big chamber device are highly correlated. Cells were grown in Media 5[17]. (**a**) Fields of view are shown in the artificial tissue. Each field of view contains ~1700 cells. (**b**) The phases between all pairs of fields of view are graphed over 10 days in the big chamber device[62], and their computation is described in Materials and Methods. **The plots were created in MATLAB_R2020B (**https://www.mathworks.com/products/matlab.html).

The fields of view (as displayed in Fig. 1.3a for spatial location within the tissue) were highly coherent (*e.g.*, phase synchronized) with each other as shown in Fig. 1.3b) and supplementary Fig. S1.2. This was measured by phase measures[62] between different fields of view on the tissue (Fig. 1.3b) as well as by measures of sychronization[63]. For example, the synchronization measure known as the Kuramoto order parameter (K) between different fields of view is defined as:

$$K = \left\langle \left| n^{-1} \sum_{j=1}^{n} \exp(i\mathrm{M}_j) - \left\langle n^{-1} \sum_{j=1}^{n} \exp(i\mathrm{M}_j) \right\rangle \right| \right\rangle$$

where the brackets denote an expectation over time and $M_j$ is the phase of the jth "giant cell". The quantity n is the number of oscillators being compared (*e.g.*, n = 2 for two fields of view) and $i = \sqrt{-1}$. If the fields of view were perfectly synchronized, the Kuramoto K would be 1.00, and if the fields of view were unsynchronized, the Kuramoto K would be 0.00. The synchronization measure (K) observed between any two fields of view was over 0.97 (Table 1.1) in a transect across the artificial tissue.

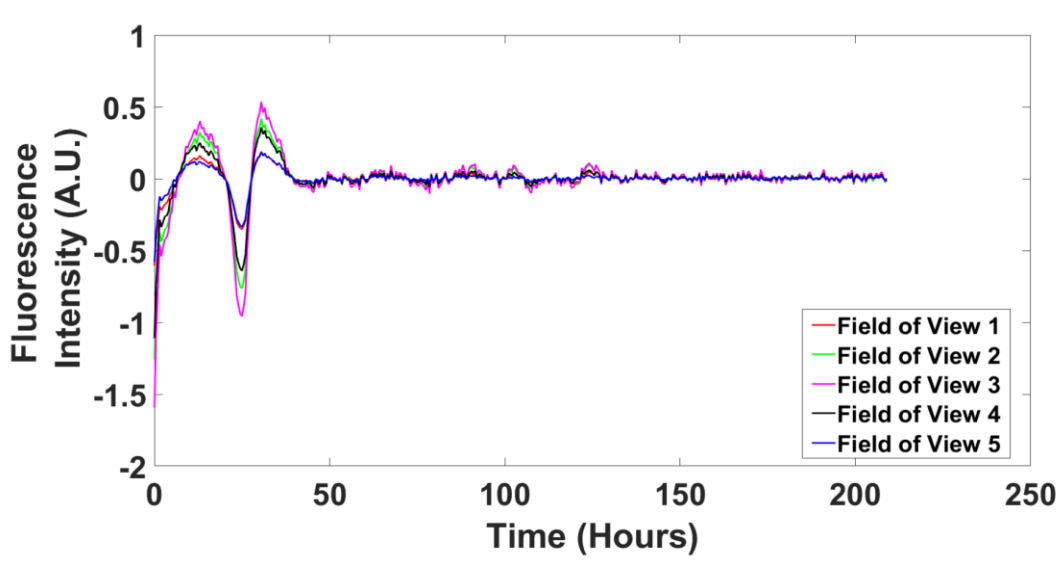


**Fig. 1.4** The trajectories of [CCG-2] fluorescence over all 5 fields of view in Fig. 1.3a aligned almost perfectly. The fluorescent intensity was normalized and detrended with a 24 h moving

average over time. **The plots were created in MATLAB_R2020B (**https://www.mathworks.com/products/matlab.html).

The trajectories of CCG-2 recorder for different fields of view aligned with each other, showing similar fluorescent trajectories over time (Fig. 1.4), a result recapitulated in three other experiments done with different media conditions (Fig. S1.4). (The use of the term trajectory is used to invoke the connection of the data on CCG-2 with the dynamic models considered below, but the cells themselves may or may not be moving). All of these views on the phase at different locations in the tissue suggest a high degree of phase synchronization across the tissue over an 1800 x 1150 $\mu m$ area (supplement Fig. S1.3). A video is available showing how a quorum sensing signal in a model will synchronize cells in a tissue completely over time[31]. As the phase evolves, there is a fan shape in the spread of phase curves and averages over single cells[1] (supplement Fig. S1.3).This can be explained by stochastic intracellular variation that will result in phase variation, as well as a quorum sensing signal that synchronizes cells to the phase mean.

Table 1.1. Measures of synchronization (K) between 5 different fields of view (FOV) along a transect through the artificial tissue in Fig. 1.3a exceed 0.97 using the Kuramoto K[63].

| K | FOV 1 | FOV2 | FOV3 | FOV4 |
|---|---|---|---|---|
| FOV1 | - | - | - | - |
| FOV2 | 0.9563 | - | - | - |
| FOV3 | 0.9373 | 0.9531 | - | - |
| FOV4 | 0.9318 | 0.9474 | 0.9513 | - |
| FOV5 | 0.9182 | 0.9262 | 0.9267 | 0.9441 |

If this synchronization is enabled by a chemical signal diffusing in the media between cells in the artificial tissue, then diffusion theory can be used to calculate an upper limit on the size of the communication signal (See Materials and Methods) of 13.05nm. This includes the possibility of the signal being a protein[64].

**A quorum sensing deterministic model predicts circadian oscillations of the artificial tissue at the macroscopic limit.**

As the macroscopic limit is approached, the full stochastic network describing the clock in single cells goes to a deterministic limit[1], and a deterministic model can be used to describe the behavior of the clock under a quorum sensing hypothesis[17]. Each field of view that contains around 1700 cells (Fig. 1.3a) can be thought of as one giant cell. The molecular counts of genes and their cognate products are large in number with little stochastic intracellular variation in molecular counts of species in Fig. 1.5. Under the quorum sensing hypothesis, the clock reaction network is specified in Fig. 1.5a. This clock reaction network has a substantial body of empirical support at both the macroscopic and microscopic levels[1,2,17,31,54,65-67]. The three clock mechanism genes are *white-collar-1* (*wc-1*), *white-collar-2* (*wc-2*), and *frequency* (*frq*). The genes *wc-1* and *wc-2* are the positive elements in the clock network, and the *frq* gene is the negative element[6]. Meanwhile, the gene *frq* encodes the oscillator[68]. The concentration of the encoded protein FRQ, provides to the cell, the time of day. The FRQ protein is the pendulum on the clock, while the transcription factor complex WCC = WC-1/WC-2 is the hand that starts the pendulum FRQ moving[69]. The negative effect by FRQ occurs by its action as a cyclin to recruit a kinase/phosphatase pair to deactivate WCC[60]. This results in a negative feedback loop that explains in part how the clock mechanism produces oscillations[65]. The description of the

dynamics of the clock mechanism genes and their encoded products have been identified in earlier work[65].

In addition to the clock mechanism genes, there are two *clock-controlled genes* (*ccg*) as outputs of the clock mechanism. The hypothetical gene *ccg* encodes the quorum sensing signal CCG, and the gene *ccg-2* encodes a hydrophobin CCG-2, whose promoter is being used as the hands on the clock mechanism[3]. The gene *ccg-2* also happens to be the best characterized *clock-controlled gene*[70]. The dynamics (*e.g.*., rate constants) of the *clock-controlled genes* are given in previous work as well[67,71]. All of the rate constants in these pieces of the model have been identified[2], including transcription rates denoted with an S, translation rates, with an L, and decay reactions for mRNAs and proteins, with a D. The new piece in the model with unknown parameters identified here by ensemble methods[72] (Fig. 1.5) is the communication between cells involving the quorum sensing signal[17].

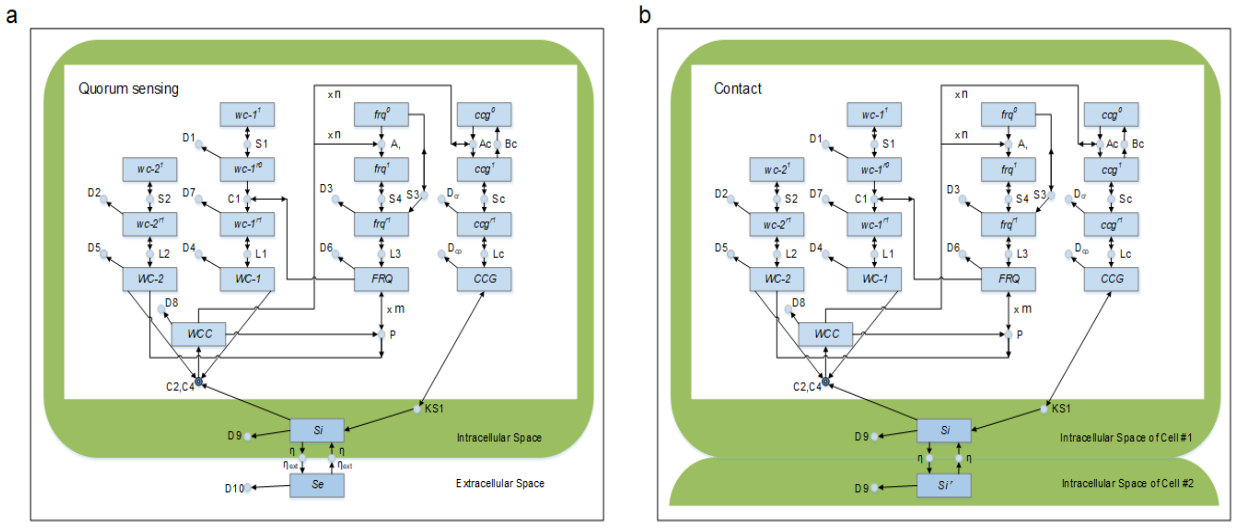


**Fig. 1.5** Quorum sensing and contact models for synchronizing clocks in single cells: (**a**) quorum sensing model. This is a modification of Fig. 1.4a in previous work[17]; (**b**) contact model.

The quorum sensing model rests on a "mean-field" assumption where the quorum sensing signal $S_e$ diffuses instantaneously and uniformly within the big chamber microfluidic device so that all cells experience the same concentration of the signal $[S_e]$ in the device. This assumption is supported by the data (Fig. 1.1d). The signal in a cell $S_j$ itself is encoded and ultimately produced by the *ccg* gene at a rate $K_{S1}$ and decays in the media at a rate D10 and at a rate D9 in a cell. This signal diffuses in or out of a giant cell, respectively, at a rate $\eta$ or $\eta_{ext}$. Depending on the concentration inside ($[S_j]$) or outside ($[S_e]$) of the cell and on volumes of the field of view and of the cell with 8 $\mu m$ diameter[73]. This diffusion assumption about the signals has been successfully used, for example, in modeling the synctitium of nuclei of the Drosophila developing blastoderm[74]. Since the field of view and cell diameter are basically the same, the areas of the field of view and of the tissue in the field of view determine the diffusion. In previous work a reasonable way for the quorum sensing signal to interact with WCC was determined, and the interaction was argued to be a negative effect on WCC production[17]. With these assumptions the diagram in Fig. 1.5a specifies the following system of ordinary differential equations (ODEs)[75] to describe the clock dynamics at the macroscopic limit:

1. $\frac{d[wc-1^0]}{dt} = 0$

2. $\frac{d[wc-1^{r0}]}{dt} = S1 * [wc - 1^0] - D1 * [wc - 1^{r0}] - C1 * [wc - 1^{r0}] * [FRQ]$

3. $\frac{d[wc-1^{r1}]}{dt} = C1 * [wc - 1^{r0}] * [FRQ] - D7 * [wc - 1^{r1}]$

4. $\frac{d[WC-1]}{dt} = L1 * [wc - 1^{r1}] - D4 * [WC - 1] - (C2 - C4 * [Sj]) * [WC - 2] * [WC - 1]$

5. $\frac{d[wc-2^0]}{dt} = 0$

6. $$\frac{d[wc-2^r]}{dt} = S2 * [wc - 2^0] - D2 * [wc - 2^r]$$

7. $$\frac{d[WC-2]}{dt} = L2 * [wc - 2^r] - D5 * [WC - 2] - (C2 - C4 * [Sj]) * [WC - 2] * [WC - 1] + P * [WCC] * [FRQ]^m$$

8. $$\frac{d[frq^0]}{dt} = -A * [frq^0] * [WCC]^n + \bar{A} * [frq^1]$$

9. $$\frac{d[frq^1]}{dt} = A * [frq^0] * [WCC]^n - \bar{A} * [frq^1]$$

10. $$\frac{d[frq^r]}{dt} = S3 * [frq^0] + S4 * [frq^1] - D3 * [frq^r]$$

11. $$\frac{d[FRQ]}{dt} = L3 * [frq^r] - D6 * [FRQ]$$

12. $$\frac{d[WCC]}{dt} = -n * A * [frq^0] * [WCC]^n + n * Abar * [frq^1] - D8 * [WCC] + (C2 - C4 * [S_j]) * [WC - 2] * [WC - 1] - P * [WCC] * [FRQ]^m$$

13. $$\frac{d[ccg^0]}{dt} = -Ac * [ccg^0] * [WCC]^n + Bc * [ccg^1]$$

14. $$\frac{d[ccg^1]}{dt} = Ac * [ccg^0] * [WCC]^n - Bc * [ccg^1]$$

15. $$\frac{d[ccg^r]}{dt} = Sc * [ccg^1] - Dcr * [ccg^r]$$

16. $$\frac{d[CCG]}{dt} = Lc * [ccg^r] - Dcp * [CCG]$$

17. $$\frac{d[ccg-2^0]}{dt} = -Ac2 * [ccg - 2^0] * [WCC]^n + Bc2 * [ccg - 2^1]$$

18. $$\frac{d[ccg-2^1]}{dt} = Ac2 * [ccg - 2^0] * [WCC]^n - Bc2 * [ccg - 2^1]$$

19. $$\frac{d[ccg-2^r]}{dt} = Sc2 * [ccg - 2^1] - Dcr2 * [ccg - 2^r]$$

20. $$\frac{d[CCG-2]}{dt} = Lc2 * [ccg - 2^r] - Dcp2 * [CCG - 2]$$

21. $$\frac{d[S_j]}{dt} = -D9 * [S_j] + K_{s1} * [CCG] + \eta * (-[S_j] + [\![S]\!]_e)$$

22. $$\frac{d[Se]}{dt} = -D10 * [S_e] + \eta_{ext} * \sum([S_j] - [S_e])$$

For simplicity the subscript for a field of view *j* on all molecular species in (1)-(20) has been suppressed. The Hill cooperativity coefficients n and m were taken as 4 in fitting models below based on previous work[65]. This deterministic model falls in the class of transcriptional repression models[76].

The big chamber device is not sufficient to test this quorum sensing model due to the loss of phase information between cells in each field of view within the big chamber device (Fig. 1.1a-d). Hence, a new microfluidic device called a "microwell device" was constructed (see Materials and Methods) (Fig. 1.1e-f). There are up to 15,876 wells within this device. Each well is 10 $\mu$m deep and 10 μm in diameter to trap one conidial cell of average size. Individual cells are easily tracked over 10 days, and their phase information about their individual clocks can be recovered[62].

Following the example of the classic work characterizing glycolytic oscillations in *Saccharomyces cerevisiae* with a mixing experiment[77], two populations of cells that were 12 hours out of phase were then mixed together[31], and then their synchronization was observed over time (Fig. 1.6d). The 240 cells were clustered by their single cell trajectories (from 0 to 30 h) into two separate clusters known as $CCG_1$ and $CCG_2$. An average of the cluster is taken to create an equivalent of a field of view, but the phase information of each single cell trajectory is preserved. The averages of the single cell trajectories in cluster 1 ($CCG_1$) and cluster 2($CCG_2$) for the CCG-2 recorder construct[3] are in good agreement with their model ensemble averages for the quorum sensing model (Fig. 1.6a-b). An examination of the observed trajectories or the

expected trajectories of the CCG-2 recorder[3] also reveals that the clusters of trajectories become synchronized in the first 80 hours (Fig. 1.6c-d). The use of the microwell device has then refined the estimate of the macroscopic limit from ~150,000 cells to 15,876 cells per device area, at which phase synchronization of cellular oscillators is achieved.

As a control, these two cell populations used in the mixing experiment (Fig. 1.6) were loaded separately into 2 microwell devices with one population receiving an additional 12 h of light before shifting to the dark and observed over ten days. These two isolated populations were then mixed *in computer* and clustered as in the real experiment (see Materials and Methods). The artificial mixture was then clustered, and over 80% of the cells in the mixture on the computer were correctly assigned to their true subpopulation membership.

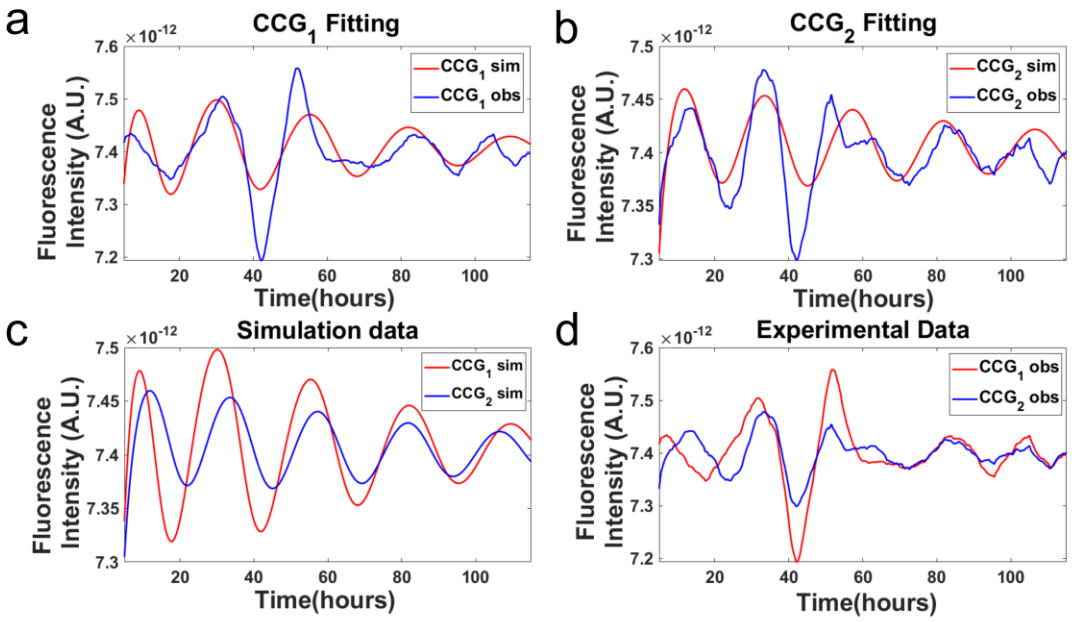


**Fig. 1.6** Data from CCG-2 trajectories fitted to an ensemble of deterministic model. (**a-b**) The trajectories of the fluorescent recorder are observed to synchronize in the first 80 hours, and in

the best model in the fitted model ensemble (supplement Table S1.1) under quorum sensing synchronization was observed as well. Single cell trajectories were clustered into two groupings. Then the 240 single cell trajectories were averaged to create a "field of view" similar to the big chamber device. These two clusters of trajectories were then fitted by the ensemble method to the quorum sensing model in Fig. 1.5a[65]. (**c-d**) Plots of the simulation data and experimental data shows trajectories that are synchronized. **The plots were created in MATLAB_R2020B (**https://www.mathworks.com/products/matlab.html).

To test the quorum sensing hypothesis at the macroscopic limit an ensemble of deterministic models specified by Eqns (1-22) was fitted to two CCG-2 trajectories for two clusters of cells in the microwell device (Fig. 1.6) (See Materials and Methods with all tests reported below being omnibus except as noted). All parameters in the model were estimated (Table 1.2). The purpose of the ensemble method is to identify models consistent with the data in Fig. 1.6 when the number of measurements is limited, but the number of parameters (Fig. 1.5) is large. Ensemble methods were originally developed by Boltzmann[78,79] and were first introduced into systems biology in 2002[72,80]. While an individual model in the fitted ensemble may be a poor predictor of the system, the average over all 40,000 models in the ensemble is quite a good predictor of system behavior (see Materials and Methods). Not only does it allow prediction of how the system behaves (Fig. 1.6a-b), but it also tells us what we know and don't know about the clock network, for example. For example, in Table 1.2 the estimated lifetime of the FRQ protein (1/D6 in Table 1.2) is about 1.7 h. The estimated value is a little shorter than the value at the macroscopic limit of 4-7 h[59]. The estimated lifetime of the stabilized *wc-1*$^{r1}$ is a critical parameter in maintaining stable circadian rhythms[65]. Here its estimated lifetime is 1/D7 = 24 h

(Table 1.2), while the measured value of 128 h was also long[65]. In general there was concordance between estimates of the rates (Fig. 1.5a) at the single cell level and macro scales[1]. In addition to the estimated parameters informing how the oscillations is sustained, the model identification through the standard errors (Table 1.2) tells us which rates are well specified by the data and which are not well specified. Both decay rates, D6 and D7, are well specified; however, there are other rates below that are not as well constrained by the data. The focus below is on the new parameters related to communication between cellular oscillators.

As a control on this Markov Chain Monte Carlo (MCMC) experiment, the chi-squared statistic $\chi^2$ was plotted as a function of sweeps (Fig. 1.7a), *i.e.*, a visit on average of once to each of the 71 parameters (*i.e.*, 28 rate constants and 43 initial conditions of molecular species) in the model (Fig. 1.5a). The MCMC experiment has equilibrated by sweep 2431 (Fig. 1.7a). The equilibration run yielded an ensemble of models with a good fit with $\chi^2 = 2016$ to n = 442 time points or $\frac{\chi^2}{n}$ = 4.56. The only departure of the model ensemble from data appears in the amplitude predicted for peak 3. So, the equilibration run was successful in converging to a well-fitting ensemble (Fig. 1.7a) and implies that the deterministic models collected in the accumulation run will fit the field of view data very well. As a second control, the communication parameters were plotted as a function of sweep (Fig. 1.7b) in the accumulation phase of MCMC. As expected, there was no systematic trend in the diffusion coefficient $\eta$ with sweep.

The MCMC experiment is summarized in Fig. 1.7c. The model average over the ensemble was used to predict successfully the two clusters of CCG-2 trajectories over time in

each field of view, $CCG_1$ and $CCG_2$. The fitted ensemble predicted the cluster 1 data quite well at the macroscopic limit. Some of the behavior of the ensemble is shown for the hypothetical signaling molecule concentrations inside and outside a cell. The signal concentrations $[S_j]$ in each giant cell j ($S_1$ and $S_2$) of the hypothetical quorum sensing signal is clearly oscillating and driving the oscillations within each giant cell in a field of view (Fig. 1.7d). The media concentration of $[S_e]$ also appears to be oscillating. Our resulting model suggests that the signal concentrations in each cell appear to synchronize with the signal concentration in the media.

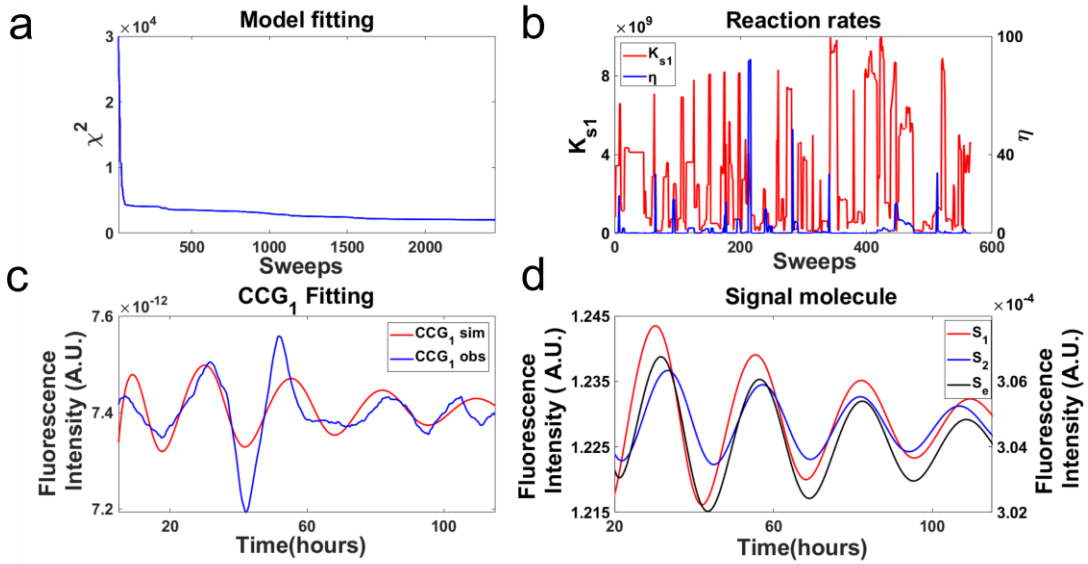


**Fig. 1.7** The model ensemble fitted to fluorescence of MFNC9[3] cells with a *ccg-2* promoter in the microwell device averaged over two clusters of single cell trajectories initially with different phase (Fig. 1.3a) supported the quorum sensing hypothesis in a MCMC experiment. (**a**) As a control on the MCMC experiment the chi-squared statistic $\chi^2$ was plotted as a function of sweeps, *i.e.*, a visit on average to all 71 parameters in the model. The large chi-squared statistics for sweeps 1-29 were removed to allow the rest of the chi-squared plot to be resolved. (**b**) As a second control two of the communication parameters were plotted as a function of sweeps to

check that there is no trend with sweep in the MCMC experiment. (**c**) The MCMC experiment demonstrated that the measured fluorescence on one field of view fitted the quorum sensing model. (**d**) The quorum sensing signals within the two giant cells did oscillate, and they appeared to converge. **The plots were created in MATLAB_R2020B (**https://www.mathworks.com/products/matlab.html).

Summary statistics across the fitted ensemble for the 28 rate constants (their means and standard errors) are given (Table 1.2), and the best fitting model with initial conditions is found in supplement Table S1.1. There are four key parameters in the clock mechanism[65], the rate of activation of the oscillator gene FRQ by WCC (A), the rate of deactivation of the oscillator gene FRQ by WCC(Ā), the rate of deactivation of FRQ (P), and the rate of decay (D7) of the stabilized *wc-1* mRNA (*wc-1*$^{r1}$). All of these values are in good agreement with their inference from previous data sets on a macroscopic and microscopic scale (supplement Table S1.1).

The new information is the inference about the communication parameters, $K_{S1}$, C4, D9, $\eta$, $\eta_{ext}$, and D10. The product of the rate of production of signal ($K_{S1}$) and the effect of the signal on WCC (C4) are constant. So, only one of these two parameters can vary independently. There is limited information about the diffusion rates as seen by plotting the chi-squared surface as a function of the diffusion coefficients, $\eta$ and $\eta_{ext}$, with the rest of the parameters at their best values (Supplement Fig. S1.5). There is a lower bound on $\eta$ of around 20 and little information about $\eta_{ext}$. The chi-squared surface supports smaller values of $\eta_{ext}$ and larger values of $\eta$ for the diffusion rates. The rate of production of the quorum sensing signal ($K_{S1}$) is large as expected[17]. The decay rate of the signal within the cell (D9) is predicted to be quite large (D9 =

10.484 $h^{-1}$) with a lifetime of 0.1 h, and the decay rate outside of the cell (D10) is predicted to be quite large (D10 = 2.375 $h^{-1}$) with a lifetime of 0.42 h.

Table 1.2. The moments of the rate constants across the ensemble for the quorum sensing hypothesis derived from a microwell experiment

| **Rate Constant** | **Ensemble mean for each rate under quorum sensing for the microwell D/D experiment** | **Ensemble Standard error (SE) of rate across ensemble computed under quorum sensing for the microwell D/D experiment** |
|---|---|---|
| A | 6.946009E-03 | 3.313135E-06 |
| Ā | 9.969590E-02 | 8.297570E-05 |
| S1 | 3.320978E+01 | 1.923567E-02 |
| S3 | 1.041769E-03 | 2.155980E-04 |
| S4 | 1.951816E+01 | 8.880192E-03 |
| D1 | 1.164574E+00 | 9.405917E-04 |
| D3 | 1.870605E+00 | 6.546756E-04 |
| C1 | 1.665926E-03 | 1.348076E-06 |
| L1 | 4.165664E+01 | 2.685045E-02 |
| L3 | 5.276481E+00 | 3.137782E-03 |
| D4 | 5.395039E-01 | 2.537757E-04 |
| D6 | 5.761848E-01 | 2.585495E-04 |
| D7 | 4.217466E-02 | 3.477031E-05 |

| | | |
|---|---|---|
| D8 | 4.741010E-05 | 8.957513E-06 |
| C2 | 3.580439E+00 | 2.470929E-03 |
| P | 9.767857E+01 | 5.976836E-02 |
| $A_c$ | 1.064269E+01 | 5.098955E-02 |
| $B_c$ | 9.094971E-01 | 2.667601E-03 |
| $S_c$ | 1.490714E-03 | 2.502344E-06 |
| $L_c$ | 1.145927E-08 | 3.711730E-11 |
| $D_{cr}$ | 5.943974E+01 | 1.366934E-01 |
| $D_{cp}$ | 4.044340E-01 | 6.436382E-04 |
| $K_{S1}$ | 2.408651E+09 | 2.156671E+08 |
| C4 | 1.234348E+00 | 5.422941E-02 |
| $\eta$ | 2.038943E+00 | 7.304766E-01 |
| $\eta_{ext}$ | 2.466155E+01 | 2.222896E+00 |
| D9 | 1.484148E+01 | 2.340141E-01 |
| D10 | 2.374897E+00 | 7.021016E-01 |

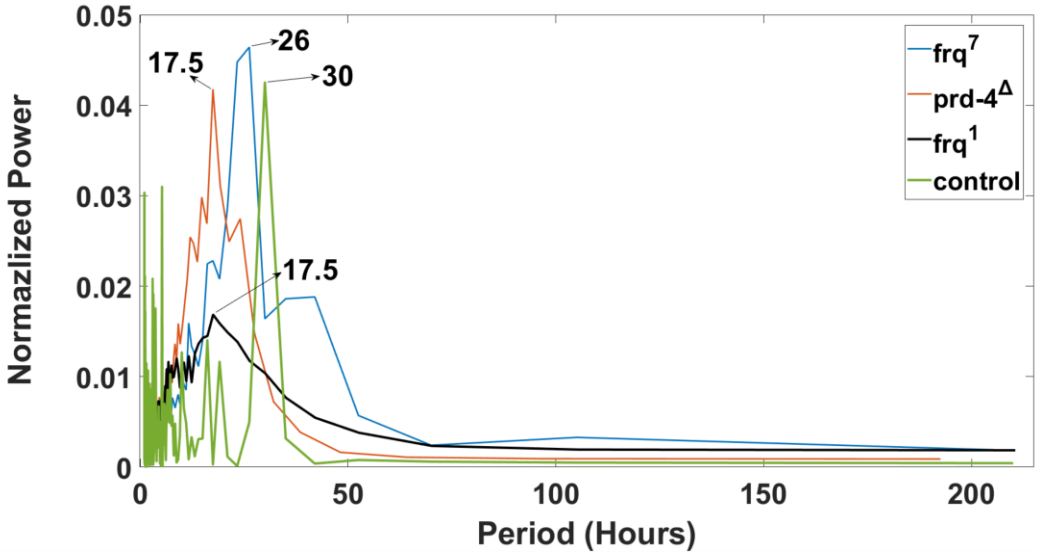


**Fig. 1.8 Periodogram or power spectrum of clock mutants and the noise model control**. Validating the circadian signal obtained in single cells in a microwell device with clock mutants of different period. The periodograms are reported for 3 mutants in the microwell device. All detrending was done with a 24 h sliding window except for *frq*$^{7}$ with its 26h observed period. A 30-hour sliding window was used for *frq*$^{7}$. An artificial dataset for a sinusoid of 30 period was also created to check that the moving averaging detrending behaved appropriately to generate the simulated period of 30 h. **The plots were created in MATLAB_R2020B** (https://www.mathworks.com/products/matlab.html).

A variety of clock mutants exist in the biological clock of *N. crassa*. Some of the clock mutants (e.g., *period-4* (*prd-4*, 18 h; *frq-1*, 16 h)[81] have shorter periods than MFNC9 (21 h)[17]; others have longer periods (e.g., *frq-7*, 29 h)[81]. These mutants provide an independent validation of the circadian signals seen in single cells using fluorescent strains of these mutants. Here we measured the period of these clock mutants in single cells over 10 days (Fig. 1.8). The resulting

periods (Fig. 1.8) agree with mutants observed in race tubes[81]. This is another example of circadian behavior in microwell devices being consistent with measurements on the macro scale.

**A contact model is also used to predict the circadian oscillations of an artificial tissue at the macroscopic limit.**

An alternative to the quorum sensing hypothesis is cell-to-cell communication or a cell contact hypothesis (Fig. 1.5b). This mechanism operates in cell aggregation of *Myxococcus xanthus*[44,82]. Under this hypothesis only cells in physical contact (as in the tissue in Fig. 1.1c) can share their communication signal. Meanwhile, the cell contact model is much more straightforward because there is no signal and no decay of signal present in the medium (Fig. 1.5b vs. 5a). The diffusion coefficients, $\eta$ and $\eta_{ext}$, are replaced with one diffusion coefficient D of the signal between cells. So, there are 4 more parameters in the quorum sensing model (Fig. 1.5a), $[S_e]$ at time 0, D10, $\eta$, and $\eta_{ext}$, than are in the contact model and one added diffusion coefficient (D) between cells in the contact model; therefore, the contact model has 3 degrees of freedom less than the quorum sensing model. The model is captured in Fig. 1.5b and specifies the same system of ODEs in equations (1)-(20) but with equations (21-22) replaced by (23):

$$23. \qquad \frac{d[S_j]}{dt} = -D9 * [S_j] + K_{s1} * [CCG] + \eta * (-2[S_j] + [S_{j+1}] + [S_{j-1}])], j \neq 1, n$$

To test the contact hypothesis at the macroscopic limit an ensemble of deterministic models specified by Eqs. (1-20, 23) was fitted to two CCG-2 trajectories for two fields of view in the microwell device (See Materials and Methods)[65]. As a control on this MCMC experiment the chi-squared statistic $\chi^2$ was plotted as a function of sweep (Fig. 1.9a). The equilibration run

yielded an ensemble of models with $\chi^2 = 4372$ or $\frac{\chi^2}{n}$ = 9.89, after 3,187 sweeps compared to previous results[65]. So, the equilibration run was not successful in converging to a well-fitting ensemble (Fig. 1.9a) and implies that models collected in the accumulation run do not explain the field of view data as well as the quorum sensing hypothesis. The MCMC fitting experiment is summarized in Fig. 1.9c. The model average over the ensemble was used to predict successfully the measured $CCG_2$ trajectory over the first cycle (Fig. 1.9c), but not $CCG_1$. Some of the behavior of the ensemble is shown for the hypothetical signaling molecule concentrations inside two giant cells. The hypothetical quorum sensing signal concentrations within a cell are clearly not oscillating in a sustained way and not driving the oscillations within each giant cell (Fig. 1.9d). As a consequence, the model had problems in fitting the first field of view as the communication between fields of view was not rapid enough for the convergence of the fluorescent cycles ($CCG_1$ and $CCG_2$). As a second control, the communication parameters were plotted as a function of sweep (Fig. 1.9b) in the accumulation phase of MCMC. The parameters displayed little trend, indicating further equilibration was not needed.

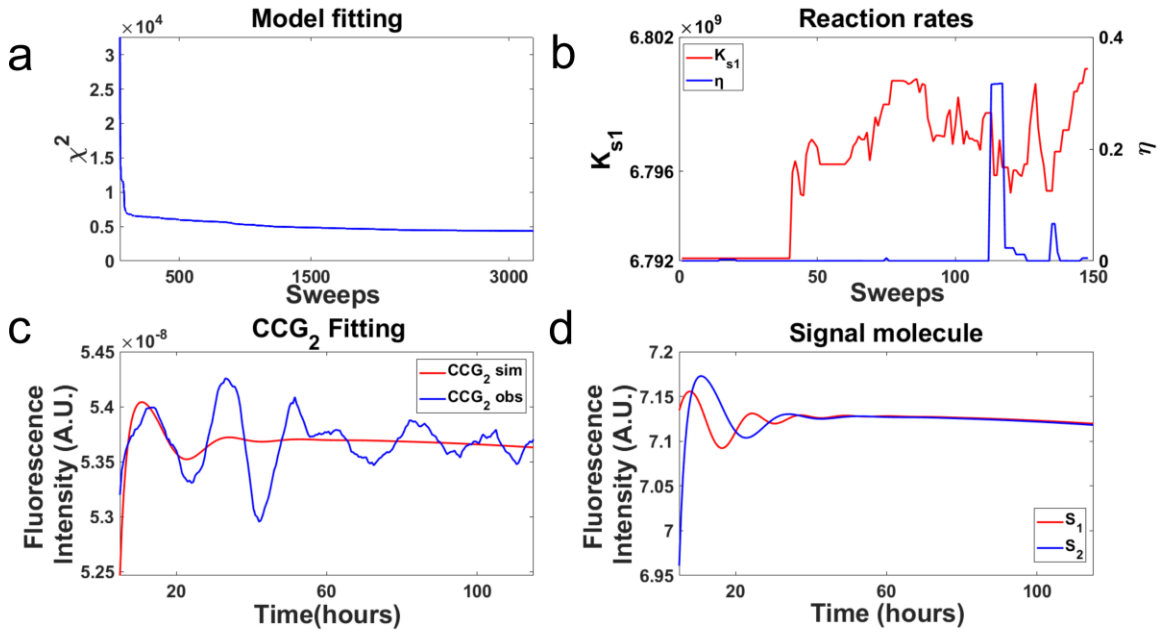


**Fig. 1.9** The model ensemble fitted to fluorescence of MFNC9[3] cells with a *ccg-2* promoter in the microwell device integrated over two fields of view (Fig. 1.3a) did not support the contact model in a MCMC experiment. (**a**) As a control on the MCMC experiment the chi-squared statistic $\chi^2$ was plotted as a function of sweep, *i.e.*, a visit on average to all 67 parameters in the model. The large chi-squared statistics for sweeps 1-50 were removed to allow the rest of the chi-squared plot to be resolved. (**b**) As a second control two of the communication parameters were plotted as a function of sweep to check for the presence of a trend in the MCMC experiment. (**c**) The MCMC experiment demonstrated that the measured fluorescence on one field of view fitted the contact model for one oscillation. (**d)** The quorum sensing signals ($S_1$ and $S_2$) within the two giant cells did oscillate in a damped way. **The plots were created in MATLAB_R2020B (**https://www.mathworks.com/products/matlab.html).

**Direct Test of the Contact Model versus quorum sensing hypothesis.**

The microwell microfluidic device provides the opportunity to test the quorum sensing hypothesis against cell-to-cell communication or contact hypothesis. Based on the single cell data alone, the final chi-squared goodness of fit of the two models were significantly different ($\chi^2$(contact) – $\chi^2$(quorum)) = 4373-2019 =2354, df = 3, P<0.0001). Relevant to distinguishing quorum sensing from a contact hypothesis, some of the microwells contain 2-3 cells, and other wells contain only 1 cell. If single cells are truly isolated and require physical contact for synchronization as in the big chamber device, the prediction is that the isolated single cells should not synchronize under the contact model. A second prediction is that under both quorum sensing and contact models there should be less variation and more synchronization in the fluorescent cells with 2 or more neighbors in a well. The results of this test are shown in Fig. 1.10.

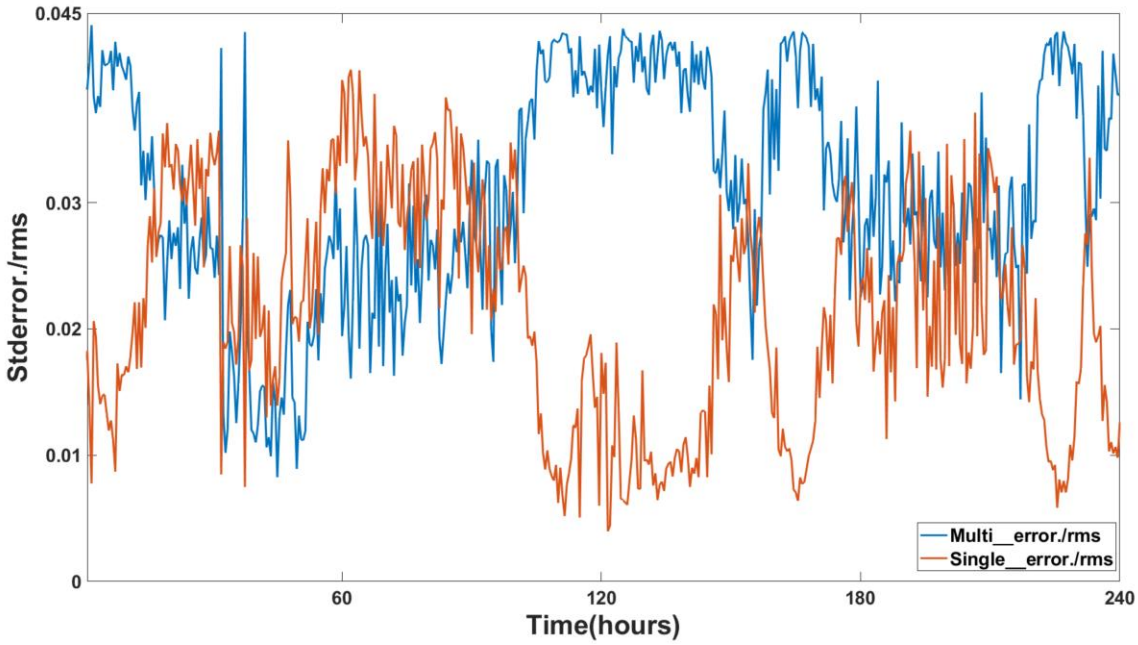

**Fig. 1.10** The standard error in fluorescence of single cells is significantly higher than that of multiple cells in the microwell device. There were 178 single cells in microwells, and 23 cells that were not isolated from each other. 1000 bootstrap samples were taken at each time point and used to calculate a variance (and hence standard error) at each time point. At each time point a root mean square error for single cells (X) and multiple cells (Y) was calculated with n = (178 + 23): $\sqrt{\sum \left[\left(\frac{1}{n}\right)\left(\sum X^2 + \sum Y^2\right)\right]}$ and used to normalize the standard errors for single and multiple cells. **Plots was created in MATLAB_R2020B (**https://www.mathworks.com/products/matlab.html).

The F-ratio comparing the variances across time was highly significant ($F_{479,479}$ = 14.5144, P < 0.00001). The normalized standard error of single cells uniformly exceeded that of multiple cells in a well. This is consistent with there being less synchronization in single cells than between wells with multiple cells. The synchronization is also computed for the two cell populations to answer the question whether there is significant synchronization in single cells.

As a negative control the Kuramoto order parameter K was calculated on 1,644 conidial cells isolated in droplets in a flow-focusing microfluidic device[17]. The resulting Kuramoto K in 1-cell droplets in the flow-focusing device was K = 0.0322 ± 0.0007[62]. In contrast, the synchronization measure K in 1-cell microwells and multi-cell microwells were 0.7018 ± 0.0066 (n = 178 in Kuramoto K) and 0.7220 ± 0.0055 (n = 23 in Kuramoto K) respectively, which are significantly greater than the negative control. The conclusion is that single cells in microwells are showing synchronization without physical contact with other cells. This observation provides support for quorum sensing. The two Kuramoto K values for 1-cell/microwell and multiple

cells/microwell are also significantly different ((z ≈ $t_{1998}$ = 45.7035, P < 0.00001). It is possible that the slightly larger Kuramoto order parameter could be due to both a contact hypothesis and quorum sensing acting in synchrony. Hence, the contact hypothesis cannot be completely eliminated.

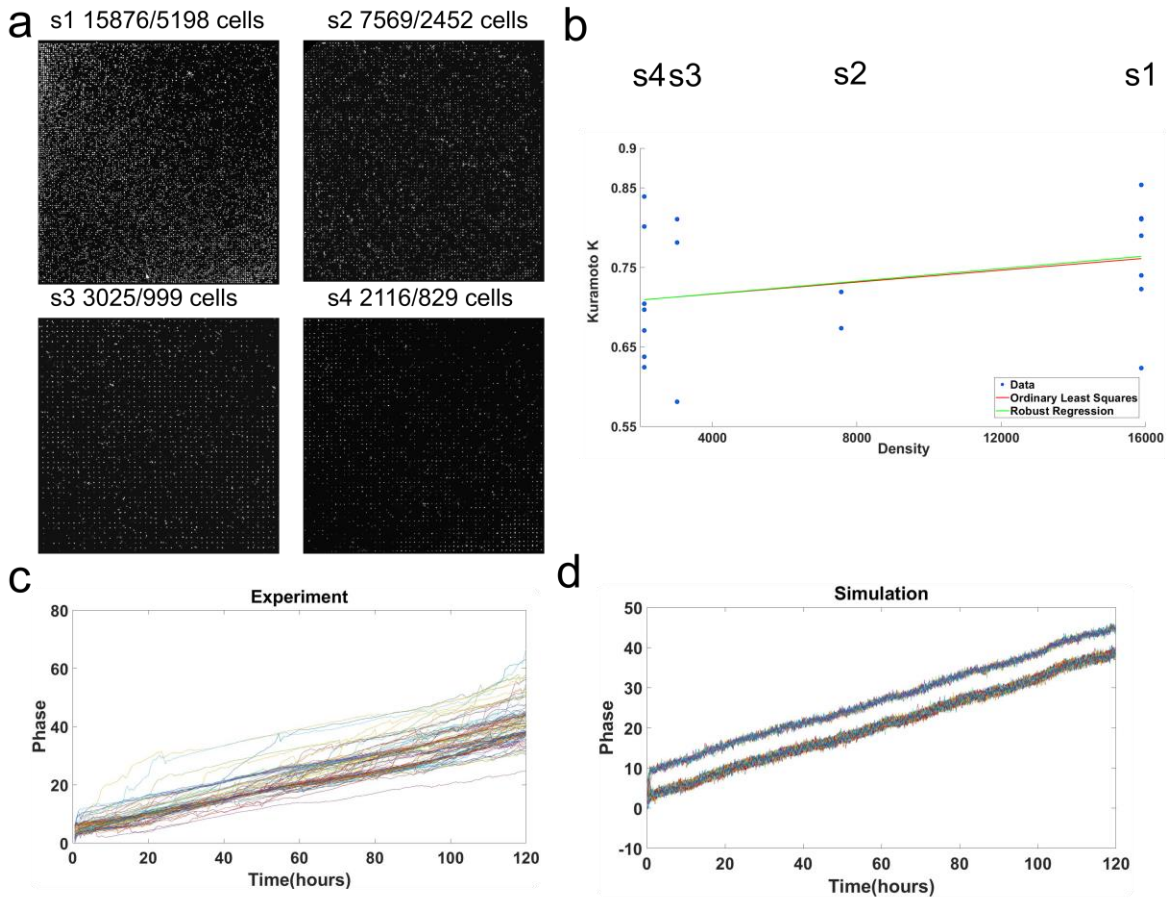


**Fig. 1.11** Microwell-based microfluidic chip with varying cell density gradient. (**a**) Fluorescence images of four chambers containing varying microwells of 15876(S1), 7569(S2), 3025(S3), 2116(S4) respectively. The number of cells that was able to be tracked with Cell Profiler were 5198(S1),2452(S2),999(S3) and 829(S4) cells. Scale bar: 100µm. (**b**) Robust Regression of Kuramoto K on density of cells for each microwell chamber using an M-estimator[83] from 5

separate and independent microwell experiments. The predicted robust regression line is K = 0.70 + (3.96 $\pm$ 3.40) ($10^{-6}$) x density ($t_{17}$ = 1.2814, P = 0.1086). The test was one-sided because the expectation is that K would increase with density. Almost the same regression line was obtained with ordinary straight line regression. At least 5,000 cells were tracked in each microwell experiment. In all 5 replicates by themselves each experiment produced a positive slope between Kuramoto K and density. A sign test for a positive slope in the 5 replicates has a P = $(½)^5 = 0.03$. Bootstrap resampling of 100 single cells was carried out to obtain the standard deviation (SE). The SE for each microwell chamber are 0.0015(S1), 0.0030(S2), 0.0039(S3), 0.0058(S4). (**c**) Plot of the experimental results of phase vs. time (5 days) with the data used in Fig. 1.6. (**d**) Simulation results of the ensemble method used to obtain the Hilbert phase trajectories in Fig. 1.6. It displays the synchronization of two different group of cells. Plots **was created in MATLAB_R2020B (**https://www.mathworks.com/products/matlab.html).

**Cell density and signal concentration affect cellular clock phase synchronization**.

With evidence for quorum sensing one prediction of the quorum sensing hypothesis was tested. A hallmark of quorum sensing is a density dependent effect on the behavior. For example, induction of Conidial Anastomosis Tubes or CATs in *N. crassa* appears to be a quorum sensing behavior, which is density dependent[84]. In *N. crassa* one hypothesis is that cell density should have an effect on communication between cellular clocks and hence their synchronization[85].

The microwell device in Fig. 1.1e-f had a cell density of 15,876 wells per area or volume of the microwell chamber, which is kept constant. The second microwell device with five chambers was constructed on the same slide with four densities of 15,876, 7569, 3025 and 2116

wells in separate chambers; the remaining chamber was reserved for mCherry beads as a control. This would allow us to measure simultaneously whether the collective behavior, such as synchronization of cellular oscillators displays quorum sensing, *i.e.*, a cell density dependence of quorum as evidenced by cellular clock synchronization (Fig. 1.11). This experiment was replicated 5 times successfully to yield the relation in Fig. 1.11b. As the density increases, so does the synchronization of cellular clocks as measured by the Kuramoto K (Fig. 1.11b). In each of these 5 replicate experiments yielding the relation in Fig. 1.11b, the slope was always positive. By a nonparametric sign test on the 5 slopes[86], this implies the P-value is $\left(\frac{1}{2}\right)^5 = 0.0325$, which is significant at the 0.05 level. These measurements begin to chart out the phase transition to synchronization. The conclusion is that collective behavior of synchronization depicts quorum sensing behavior.

It is natural to ask whether or not other properties of cellular clocks have a relation to density as found in the cell density-dependent glycolytic oscillations in *S. cerevisiae*[85]. If cellular oscillators were in phase, they might be expected to reinforce the circadian signal. In fact, there also appears to be a significant relation between the average amplitude of cellular clocks (as measured by the maximum in the periodogram or power spectrum) and their density in the microwell device as they synchronize (Fig. S1.6a), but not with period (Fig. S1.6b) in contrast to glycolytic oscillations[85].

While the quorum sensing model has a substantial body of empirical support at both the macroscopic and microscopic levels[1,2,17,31,54,65-67], it is sometimes useful to consider a simpler heuristic model at the center of both collective behavior[37] and statistical physics[46,87], namely the

Kuramoto model of phase synchronization, to highlight how phase synchronization is taking place. The model shares some features with our clock model of quorum sensing, such as a mean-field assumption about the quorum sensing signal. This Kuramoto model also focuses entirely on phase synchronization being described here and has been used previously to elucidate the clock model[17].

In this model there are n oscillators with constant intrinsic frequencies $\omega_i$ and measured variable Hilbert phases $\phi_i$. Kuramoto connected these in a system of ODEs to which stochastic intracellular noise has been added:

$$\frac{d\phi_i}{dt} = \omega_i + K\sum_{j=1}^{n}\sin(\phi_j - \phi_i) + \epsilon_i, i = 1, \dots, n,$$

where K is the unknown coupling constant between all of the n oscillators and $\epsilon_i$ is the stochastic intracellular white noise in the cellular clock with mean 0 and variance $\sigma^2$. A stochastic Runge-Kutta Method(SDEs)[88] and Markov chain Monte Carlo (MCMC) were applied to identify the Kuramoto model. The ensemble method was used to fit the phase trajectories of the stochastic Kuramoto model to the measured Hilbert phase trajectories of each of the oscillators in Fig. 1.7 to examine the phase synchronization. In carrying out the fitting the initial Hilbert phase of each of the n oscillators at time 0 ($\phi\_i\ (t = 0)$) and the coupling constant K were the parameters to be identified. The initial frequencies $\omega_i$ were sampled from the measured frequencies from a periodogram of isolated cells[31]. The fit was excellent with a chi-squared per data point of $\chi^2$/n = 0.69. The resulting coupling constant of K = 10.0094 +/- 0.0018 was substantial, which provides

another line of evidence of the phase synchronization of the oscillators through a quorum sensing signal in Fig. 1.11d. Furthermore, the spread over time in Hilbert phases of the oscillators graphically portrays the tug of war between the quorum sensing signal to synchronize the oscillators and the noise $\epsilon_i$ decoupling them.

**Discussion**

In previous work we have shown that by varying the microfluidic device and hence the cellular environment that there is the potential to test each of three hypotheses about the cause of the transition to phase synchronization of cellular oscillators[1,54]. One, there is a possibility that stochastic intracellular noise by itself can play a positive role in phase synchronization of cellular oscillators[54]. Experimental evidence for this neutral model was recently provided with a flow-focusing microfluidic device that isolated cells in droplets in previous work[1,54]. A second possibility is that a chemical signal could play a role in phase synchronization[17] of cellular clocks[31]. Prior evidence for this hypothesis has been provided as well[31,63]. A strong inference framework was entertained for this second signaling hypothesis[29], a signal diffusing in the media to cause synchronization[17] versus the other alternative hypothesis involving cell-to-cell contact as a means to synchronization[44]. The final possibility is that cell cycle coupling with circadian rhythms could provide an explanation[89,90] for phase synchronization of cellular oscillators. This hypothesis has yet to be tested in *N. crassa*. By varying the microfluidic device design each of these hypotheses can be tested[1] and used to extract information about a putative quorum sensing signal.

A big chamber microfluidic device was designed here to create an artificial tissue that allowed observation of single cell oscillators in the macroscopic limit of 150,000 cells (Fig. 1.1b). This cell number was sufficient to reveal the emergence of circadian rhythms (Fig. 1.1d). Over the dimensions of the device a high degree of phase synchronization was observed (Fig. 1.3, Table 1.1). In fact, the dimensions of the device allowed the estimation of a bound on the putative quorum sensing signal radius of 13.05 nm. The synchronization recapitulated the behavior of Nakashima liquid cultures at the macroscopic limit[22]. It is possible that by increasing the size of the big chamber device to limit diffusion, phase variation in spatio-tempral patterns across the device could be seen[91]. In synthetic quorum sensing systems, spatio-temporal dynamics, such as waves, were observed over on a 400 $\mu$m scale, but there are other factors including the lifetime of the hypothesized quorum sensing signal S in the media (1/D10 = 0.42 h) in *N. crassa* that may have led to different behavior in the big chamber device over 1800 $\mu$m.

In order to refine the specification of the cell density at which a phase transition to synchronization takes place experimentally and to test whether collective behavior of synchronization was a quorum sensing behavior, a second microfluidic device known as a microwell device was designed to trap individual cells at varying densities. The quorum sensing model against a contact model of communication (Fig. 1.1e-f) was also tested. This device mimics a microtiter plate at a microscale for trapping single cells. Initially a total of up to 15,876 cells in wells in the microwell device could be individually tracked and measured for their fluorescence over ten days (Fig. 1.6). Averaging over the single cell trajectories permitted the examination of phase synchronization in the macroscopic limit while preserving the phase information of individual trajectories (Fig. 1.7 and 9). Both the quorum sensing and contact

models were fitted to experimental data. The results favored the quorum sensing model as cells were able to synchronize at a faster pace. The single cell measurements in the microwell device were also validated by the use of mutants with varying period microscopically, and the measurements in a microwell device were concordant with those at the macroscopic scale[81] (Fig. 1.8). Yet even the quorum sensing model is a simplification. Those systems displaying quorum often utilize not one signal, but multiple signals[92]. *N. crassa* quorum is likely to be more complex than hypothesized here. Some improvements in measuring phase synchronization in these new microfluidic devices should be possible with better single cell tracking methods[93]. While the microwell device is an elegant design that allows simultaneous testing of phase synchronization, density-dependence of quorum sensing, and the contact hypothesis, it has limitations. It is possible to envision other more specialized designs that more strongly test the contact hypothesis, and these designs should be pursued. Implementing the microwell design required 11 trials with 5 successes to overcome problems with number of cells tracked less than 5,000 (3 experiments failed to meet this criterion), cells growing as a failure (2), or an image stitching problem (1).

Several results support the quorum sensing hypothesis: (Fig. 1.7) fitting of the quorum sensing mode; (Fig. 1.10) greater variance in single cells vs. multiple cells in microwells; (Fig. 1.11) density effect on phase synchronization; (Fig. S1.6) density effect on amplitude. There was also one additional piece of data that was supportive of the quorum sensing hypothesis. Wells with single isolated cells in the microwell device still displayed phase synchronization (Fig. 1.10). This observation can be explained by the theory of the existence of a diffusible signal, but not solely with a contact model hypothesis. This result, however, does not rule out the possibility

that both quorum sensing and contact could still be playing a role in chemical communication between cellular clocks.

To test directly whether synchronization of cellular clocks was a quorum sensing behavior as in CAT induction in *N. crassa*[84], the density of cells was varied in one microwell device with multiple chambers at different cell densities (Fig. 1.11a). Synchronization was density-dependent as measured by the Kuramoto K order parameter and appeared to represent a second order continuous phase transition. Synchronization appeared to be occurring over the range of densities from 2166 to 15,876 wells with cellular clocks (Fig. 1.11a). That raises the question of how density-dependence enters into the quorum sensing model. A specific hypothesis of how this arises will be addressed with new approaches in metabolomics of living systems in real time[94].

While conidial cells are relatively easy to manipulate, a remaining challenge is the study and manipulation of the filamentous stage in the fungal syncytium with microfluidic devices[95-97]. It is very likely that by considering other life stages in the fungal syncytium, other mechanisms of cellular communication will be uncovered and found to be involved in the phase transition to synchronization of cellular oscillators[98].

**Conclusion**

A “big chamber” microfluidic experiment was fabricated to demonstrate that communication existed between cells in an artificial tissue of ~150,000 cells. At this macroscopic limit there was a high degree of phase synchronization between cells in the artificial

tissue. The dimensions of the "big chamber device" provided an upper bound on of 13.05 nm radius for the putative quorum sensing signal, which includes the possibility that the signal is a protein. In a second microfluidic experiment utilizing a microwell device housing ~15,876 wells, the phase of individual cells could be captured. This enabled a refinement of phase synchronization occurring with no more than 15,876 wells per chamber. A microwell with varying microwell arrays assisted in confirming that cells were able to synchronize with lower well density of 2116 per chamber in a microwell device. With the resulting single cell fluorescence trajectories of single cells in the microwell device, a strong inference framework[29] was established to test a quorum sensing hypothesis versus a contact hypothesis for communication using ensemble methods. The ability to isolate single cells in individual wells showing phase synchronization provided strong evidence for the quorum sensing hypothesis and some information about the communication parameters that quantitate quorum sensing. Using the microwell devices, the collective behavior of synchronization was shown to be density-dependent and hence a quorum sensing behavior.

## Materials and Methods

### Device design and fabrication.

Microfluidic devices were made of polydimethylsiloxane (PDMS) using standard soft lithography techniques. The microfluidic "big chamber" device consisted of one inlet and one outlet for sample loading, an empty chamber with 1150 μm in width, 1800 μm in length and 10 μm in height. The microwell microfluidic device was composed of a microwell array that are 10 μm in diameter and 10μm deep. microwell array contains an interlaced 126 × 126 grid of wells, resulting in a total of 15,876 wells. An additional microfluidic device that contained five

chambers with varying microwells was fabricated and placed on one glass slide. The microwell array was 126×126 (S1), 87×87 (S2), 67×67, 55×55(S3), 46×46(S4) respectively.

**Strains**

A *bd,ccg-2P:mCherry,A*$^{99}$ known as MFNC9 as well as *bd,ccg-2P:mCherry,prd-4* and *bd,ccg-2P:mCherry,frq*$^{7}$ , and *bd,ccg-2P:mCherry,A,frq*$^{1}$ were utilized for most fluorescent measurements. A *bd,ccg-2P:mCherry,A,frq*$^{7}$ and *A bd,ccg-2P:mCherry,A,frq*$^{1}$ were created by the crosses MFNC9a x frq$^{1}$,bd (FGSC 2670) and MFNC9a x frq$^{7}$,bd (FGSC 4878), and the *prd-4* fluorescent mutant was described previously[17].

**Microfluidic experimental setup**

MFNC9 cells and related strains with the *mCherry* recorder were first placed under an LED light source (color temperature 6500K) for 26 h in three different media: 1) media 5 described previously[17]; 2) 0.1% glucose + Vogel's media[100]; 3) 0.001M quinic acid + Vogel's media. Cells were loaded into the big chamber polydimethylsiloxane (PDMS) microfluidic device (**Fig. 1.1**) using a syringe pump at a flow rate of around 5 µL min$^{-1}$. For the microwell device, 50µL of 70% ethanol was pipetted into the inlet, followed by priming with 50µL of 1× PBS supplemented with 0.1%(w/v) bovine serum albumin (BSA). This was followed by pipetting 30µL of cell suspension. Cell concentration of 6 * 10^7 cells/ml were used. Extra cells that were not captured in microwells were washed away with extra media. mCherry beads (Takara Bio) are loaded into one of the microwell chambers as a control for all experiments.

**Imaging and Cell Tracking**

A CCD camera (AxioCam HRm, Carl Zeiss Microscopy, LLC, Thornwood, NY) was used to record the fluorescence intensity of cells through a microscope (Imager. M2, Carl Zeiss, Microscopy, LLC,Thornwood, NY) with a motorized x-y stage (Mechanical stage 75 x 50 R, Carl Zeiss Microscopy, LLC, Thornwood, NY) in a dark room. The microscope consists of a Colibri LED light source with continuous brightness adjustment and automatic calibration. Images were taken every 30 minutes with an exposure time of 900 ms over the 10-day experiment. Loss of cell viability was measured to be 20% or less over ten days[17]. Autofocus was not used because it increased the exposure time and hence possibly photobleaching. The excitation light from a LED light source was guided through a filter set (Filter Set 60HE, Carl Zeiss Microscopy, LLC, Thornwood, NY). All experiments conducted were done in an environmental control enclosure chamber (InVivo Scientific) at a temperature of 30°C.

CellProfiler was used to track individual cells over time[17,93] and validated against our own MATLAB cell tracking code over time[17] reported previously. The number of cells tracked was lower as cells that grew filaments were discarded from the tracking process. Each fluorescence time series were normalized with mCherry beads, log-detrended with a 24 h moving average[17], and the periodogram computed[17]. The fluorescence of the field of view was obtained by integration over the field of view. In parallel for each field of view the total fluorescence was normalized with packed mCherry beads, log-detrended with a 24 h moving average, and used in deterministic model identification by ensemble methods. Prior work had demonstrated that variation in room temperature of the LED light source was 1.11% per 1 $^{o}$C and highly correlated

with control bead intensity[101]. Thus, normalization by the intensity of the mCherry beads removed variation in LED light source intensity."

**Estimating an upper bound on the size of the quorum sensing molecular signal**

Assuming that a quorum sensing molecule exists, we made an estimate that it would take 24 hours for it to diffuse across the whole device with a size of 1800 μm. The molecular diffusion coefficient is then calculated by the following equation $D_A = L_a{}^2 / t_D$. $D_A$ is the diffusion coefficient of the quorum sensing molecule while $L_a$ is the size of the microfluidic device where the cells are confined in, $t_D$ the travel time and $L_a$, the travel distance. We are able to obtain a diffusion coefficient of 2250 $\mu m^2$/min with this following equation. Next, we used the Stokes-Einstein Equation to obtain an estimate of the upper limit of the size with $D_A = k_B T / (3\pi\eta d_A)$ where $D_A$ is the molecular diffusion coefficient, absolute temperature T, by the Stokes-Einstein Equation, $d_a$ the diffusants molecular diameter, η the solvent viscosity. We were then able to obtain an upper limit of size of the quorum sensing signal as 13.05nm.

**Calculating phase**

To calculate the phase for a fluorescent series x(t), first the Hilbert transform $\tilde{x}(t) = PV\ \frac{1}{\pi}\int_{-\infty}^{\infty}\frac{x(\tau)}{t-\tau}d\tau$ was computed from the Fast Fourier Transform[102] of x(t). The Hilbert phase $F^H(t)$ is defined as the phase angle between the Hilbert Transform $\tilde{x}(t)$ and x(t) by $F^H(t) = tan^{-1}\left(\frac{\tilde{x}(t)}{x(t)}\right)$ to avoid discontinuities in the phase angle at $\pi$ and -$\pi$, the Hilbert phase was continuized to $F^C(t)$. The continuization was done recursively through the relation: $F^C(t+1) = F^C(t) + m^C(t)2\pi$, where at each step the argument m was chosen to minimize: $Df_m = |F^H(t+1) - F^C(t) + 2\pi m|$. With the continuized Hilbert Phase $F^C(t)$, the phase is defined

by: $M^C = \frac{|F^C(t_1) - F^C(t_0)|}{2\pi}$ in units of cycles. An accessible description of these phase measures and code to calculate them in MATLAB are available[62] with associated MATLAB in GitHub.

**Ensemble Methods**

The quorum sensing and cell-to-cell contact models specifying the ODEs in (1)-(23) were identified using a Metropolis-Hastings updating scheme[65]. Proposed solutions during the Markov Chain Monte Carlo (MCMC) were with an Adaptive Runge-Kutta solver. The equilibration stage involved 40,000 sweeps. The accumulation phase involved 40,000 sweeps.

The data sets generated during the current study are available from the corresponding authors on reasonable request.

# CHAPTER 3

# THE CLOCK IN GROWING HYPHAE AND THEIR SYNCHRONIZATION IN NEUROSPORA CRASSA

Xiao Qiu, Jia Hwei Cheong et al. To be submitted to (Scientific Report)

**Abstract**. Utilizing a microfluidic chip with serpentine channels, we seeded the chip with Neurospora *crassa* filaments in an agar plug and successfully captured individual hyphae in channels. For the first time, we report the presence of an autonomous clock in hyphae. Fluorescence of a mCherry recorder gene driven by a *clock-controlled gene-2 promoter* (*ccg-2p*) was measured simultaneously along hyphae for every half an hour for a period of at least 6 days. Single hyphae were entrained to light over a wide range of day lengths, including 6, 12, and 36 h days. Furthermore, hyphae also displayed temperature compensation properties, where the period of oscillations were stable over a physiological range of temperatures from 24 °C to 30 °C (Q 10 = 1.00-1.10). Hyphae tracked in individual serpentine channels were highly synchronized (K=0.60-0.78). A clock model developed was able to mimic hyphal growth observed in the serpentine chip.

**Significance**. One of the central problems in systems biology is understanding how clocks in single cells synchronize – that is, can we explain how the irregular behavior of single cell clocks gives rise to the highly orchestrated behavior of populations of $10^7$ cells per ml?[17,31] This synchronized behavior of cell populations is observed in plants[103], flies[104], worms, and mammals[105] as well as fungi[4,106]. The answer to this question may depend in part at which life stage the clock is observed to operate. Our initial efforts to address this question have focused on the simpler stage of single conidial cells[31]. We restricted our consideration initially to simplify the mechanisms at work in cell to cell synchronization. One class of mechanisms involves quorum sensing operating so that cells can set their clocks by a common signal in the medium[17]. Another class of mechanisms involves a positive role of stochastic intracellular noise in generating circadian oscillations[107]. In both cases cells were placed in media to suppress cell

division and the complication of the cell cycle gating circadian rhythms[90,108]. We now remove this restriction to examine other mechanisms of cellular clock synchronization.

As these conidial cells progress to later developmental stages, there is the possibility of other mechanisms for cellular synchronization not present in single conidial cells coming into play, such as cell cycle gating of circadian rhythms[108,109]. In single cells not dividing three mechanisms of clock synchronization may be at work. Conidial cells could by excreting a quorum sensing (QS) signal that serves to synchronize cells[31]; alternatively, cells could communicate by cell to cell contact as in Myxobacteria[44] or possibly the filamentous cyanobacterium, Anabaena[110]. Third, stochastic intracellular noise from a common environment could serve to synchronize cells as well[49,107,111,112]. With cells growing as hyphae there are at least three additional mechanisms of synchronization between nuclei[17]. A QS signal could be made and only be transported between nuclei in the same hyphae, or alternatively a QS signal could be made and excreted into the media as well transported in hyphae. In a final mechanism nuclear division could be gating the synchronization process. To explore the collective behavior of hyphae requires new kinds of experimental approaches in microfluidics[95,96] as well as new theoretical approaches to the study of cellular clock synchronization in hyphaes[39]. Understanding how molecules within a synctitium of nuclei in a fungal network is part of a much broader problem of how mRNAs and proteins are shared between nuclei under a balance of advection (i.e., drift within the shared cytoplasm) and diffusion of these molecules[98].

The goal here is to explore three questions: (1) Can a clock model be developed and specified for single or few hyphae observed by microfluidics; (2) how do real hyphae actually

behave; and (3) does a model developed here behave like real hyphae? The beginning point of this work is merging growth models for filamentous fungi[113,114] with existing deterministic clock models on conidia with experimental support[2].

Here, we developed a microfluidic device with multiple serpentine channels each with a length of at least 32 millimeters (mm) in length to address these three questions. The present study is aimed to identify whether or not there are clocks in single hyphae with the setup shown in **Fig. 2.1**. The best studied clock-controlled gene is *clock-controlled gene-2* (*ccg-2*)[70]. The strain MFNC9 possesses the promoter of *ccg-2* attached to an mCherry recorder without the upstream region providing developmental control of the recorder[31,70]. Cells engineered for fluorescence[3] were inoculated into a microfluidic device and placed on a Zeiss microscope maintained in a temperature controlled incubator. Media was pumped through the microfluidic device to support filament growth and imaged every 30 minutes (m) over at least 6 days. Our results will help us to understand how they behave and apply it to a clock model for growing hyphae.

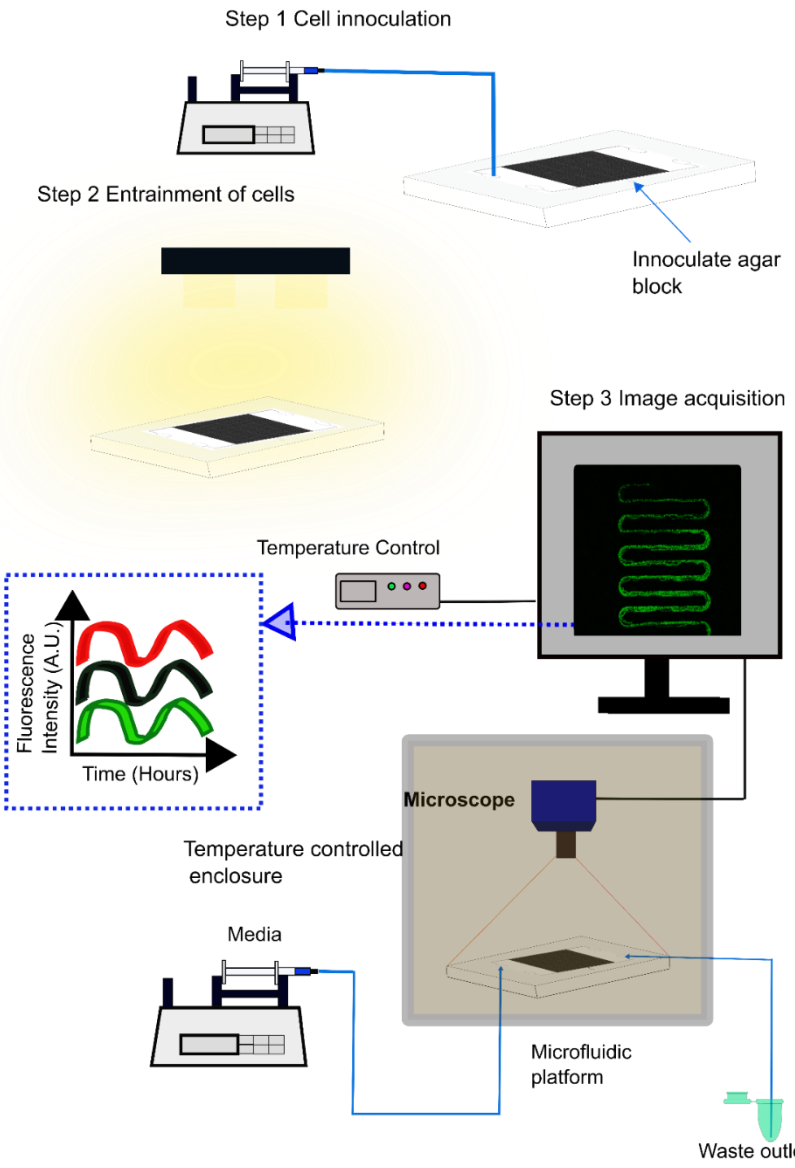


**Fig. 2.1. Schematic representation of experimental setup for the acquisition of fluorescence signal from serpentine chip.** In step 1 of the protocol, a syringe pump is used to fill the chip with media and a small *N. crassa* agar block with fluorescent strain MFNC9[3] is inoculated into cell inlet port. In Step 2, cells were entrained with at least 2 hours of light at 3700 lux. In Step 3, fluorescence of cells in serpentine channels were measured of every 30 minutes. For temperature compensation experiments, temperature is varied with the temperature control. Meanwhile, a LED light source was used for light entrainment, and the temperature was kept constant in the

enclosure. Time series of fluorescence measurement over at least a period of four days was obtained through the images collected.

## Results

### Serpentine microfluidic device design provides a growth environment for filaments

The microfluidic device was developed and designed for the purpose of providing growing cells with sufficient media for growth and recording their fluorescence over time using fluorescent strain MFNC9[3]. The diameter of *N. crassa* conidia is known to be around 3 to 8 µm, while the hyphae have a diameter of around 8-15µm. Hence, the height of the chip of 10µm was designed for the serpentine growth channels to ensure that their height is slightly larger than the *N.crassa* hyphal diameter, which ensures that media would be able to flow constantly through the serpentine channels. This was verified by simulating the flow profile with the COMSOL Multiphysics software (**Fig. S2.1**). The width of the chip was maintained at 15µm to ensure the possibility of media transported along the channels via diffusion to support a growing filament. Reducing the width of the channels may assist in the hyphal tracking process; however, we were still able to optimize the hyphal tracking procedure and branching did not affect our results.

An agar plug consisting of conidia was loaded into the cell inlet and sealed with a modified flexible tubing of the same diameter. To achieve the goal of observing hyphal growth for a period of at least 6 days, serpentine chips of a length of 32µm and 63mm were fabricated. Hyphae grew from the agar plug and elongated towards the serpentine channels due to the presence of nutrients being supplied from the medium channel at the other end of a channel. Clear oscillations were observed for serpentine chips of both lengths as seen in **Fig. 2.6b**. Here

we can observe that hyphae can be tracked in both chips, hence in the future, depending on the studies that need to be done either chip can be utilized.

To ensure hyphae have access to a constant supply of nutrients, media was supplied into the chip at a constant flow. We examined the influence of varying glucose concentration (0.1% ,0.5%, 0.70%, 1.5% glucose) in the serpentine chip. The goal was to ensure cells were provided with an adequate amount of nutrients to grow as well as to oscillate. Interestingly, when the glucose concentration of 0.5%-1.5% was infused into the chip, hyphae only grew a quarter length of the serpentine channel and ceased to grow the full length. An explanation for this phenomenon is that when glucose concentration was increased, cells would efficiently take in more of nutrients provided, and hyphae branching would occur more frequently, causing a huge pressure buildup in the chip. As a result, media would have difficulty diffusing or flowing through compared to when a lower glucose concentration was utilized. Hence, considering that the elongation of hyphae at a higher concentration of glucose was inhibitory to hyphal extension, for further experiments 0.1% of glucose media was supplied into the chip. Hyphae were able to grow the full length, and time-lapse experiments of at least 6-10 days were successfully executed (**Fig. 2.1**).

**Clock Model in a growing hypha**

Consider a single growing hypha in one-dimension x. The velocity of any point, such as the nuclei, within the growing hyphae is given by $v(x,t)$, and the location of the furthest boundary of the exclusion zone to growing tip is $x_P(t)$ (**Fig. 2.2**).

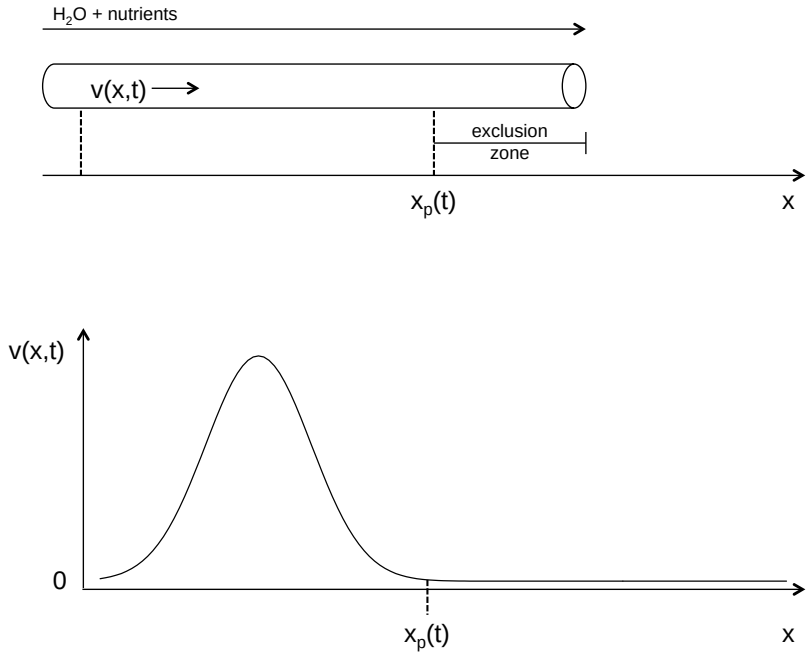


**Fig. 2.2**. A growing hypha idealized as a cylinder is shown above with the velocity distribution of nuclei along the hypha shown below. The influx of nutrients and media drives the flow towards the tip. The zero point of reference $x_P(t)$ along the hypha is the beginning of the exclusion zone near the tip. The velocity distribution asymptotes to a fixed nonzero value at the beginning the exclusion zone and sufficiently far back from the tip.

The segment about 12 $\mu m$ prior to the tip is known as the exclusion zone for nuclei along the tip[115]. To a first approximation the velocity $v(x,t)$ of cytoplasm and nuclei at position x in the hyphae at time t is considered to have a fixed distribution, which goes to a fixed value at the distal boundary to the tip (the Spitzenkorper) and also goes to zero sufficiently far back from the tip. If the coordinate $\xi$ is defined relative to the beginning of the exclusion zone (**Fig. 2.2**), *i.e.*, $\xi = x - x_p(t)$, then for a fixed velocity distribution the velocity can be written as:

$$v(x,t) = V(x - x_p(t)) = V(\xi)$$

This velocity distribution and the coordinate of the growing tip $x_P(t)$ can be measured in a microfluidics device with microscopy tools like cell profiler[93].

A second variable in the model is the density $\rho(x,t)$ of nuclei along the hyphae as captured by the fluorescence[115] or luminescence of the hyphae[95]. This density is also measurable[93]. This density is usually considered to satisfy an equation of continuity[114]. If the flow $\mathcal{F}(x,t) = v(x,t)\,\rho(x,t)$ , then the equation of continuity for the hyphae can be written:

$$\frac{\partial \rho(x,t)}{\partial t} = \frac{\partial\, \mathcal{F}(x,t)}{\partial x} + \mathbb{P}(x,t), \qquad (1)$$

where $\mathbb{P}(x,t)$ is the production of new hyphae nuclei from carbon sources, water, and other components of the growing tip. Production at the tip is thought to be a function of the component density at the tip $\rho(x,t)$ as well as the amount of food $\Phi(x,t)$ at the location x and time t. Tip production $\mathbb{P}(x,t)$ is assumed to be proportional to these two quantities, density and food:

$$\mathbb{P}(x,t) = k_p \rho(x,t) \Phi(x,t) \qquad (2)$$

The rate parameter $k_p$ is the rate of tip production. Initial conditions for the density of nuclei are given by the product of two step functions (one upward and one downward step function; see supplement). One example of this kind of initialization is the inoculation of the tube at the beginning of the tube and a fall of in nuclei away from the beginning of the tube. In the

simulator the initial velocity distribution can be specified from the initial density distribution (see supplement).

For determining the growth of the hyphae, what is left is to specify is what is happening to the food $\Phi(x,t)$. The food is initially distributed uniformly in a microfluidic device or race tube or more generally the product of two step functions (one stepping up and one stepping down; see supplement), and the density of the hyphae determines in part the rate at which the food is consumed:

$$\frac{\partial \Phi(x,t)}{\partial t} = -k_{\Phi}\, \Phi(x,t)\rho(x,t) \qquad (3)$$

The experiment is such that the food is consumed at a rate determined by the density of the hyphae. This completes the growth portion of the model, and there is no reason that this could not be equally well applied to a race tube as opposed to a microfluidics device. Only the interpretation of the density $\rho(x,t)$ of nuclei would change slightly to the density of hyphae in a race tube.

The rate equations for the clock components have substantial experimental basis[2,65,67]. The 3 clock components include the genes *frq*, *wc-1*, and *wc-2* and their cognate mRNAs and proteins[116]. The gene *frq* encodes the oscillator protein FRQ, which is a readout of the time of day[68]. The protein WC-1 is the light receptor of the system[69], and the complex WC-1/WC-2 activates the oscillator gene *frq*. The rate equations have been given[65], as an example:

$$\frac{d[FRQ]}{dt} = L_3[frq^r] - D_6[FRQ], \quad (4)$$

where the translation rate is $L_3$ and the decay rate of the FRQ protein is $D_6$. There are similar rate equations for the remaining 16 molecular species that can be derived from the genetic network (**Fig. 2.3**)[65].

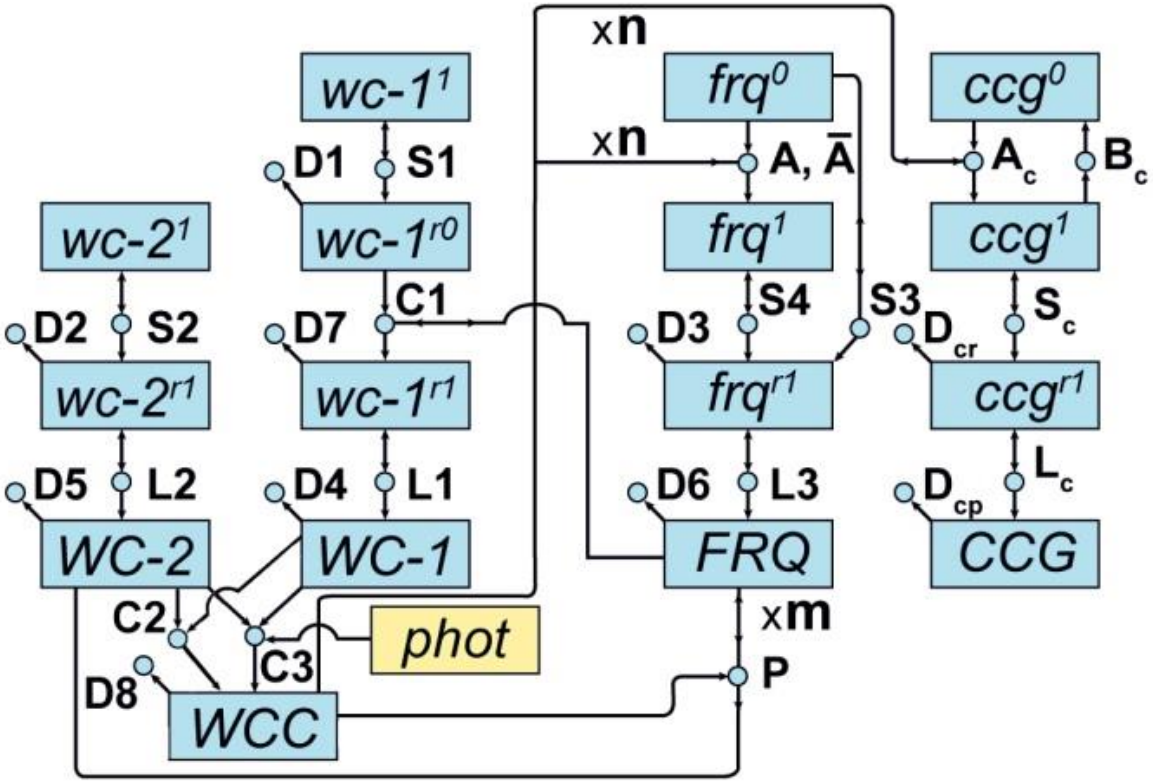


**Fig. 2.3**. Genetic network for the clock in *N. crassa*. Boxes are species, i.e., genes, mRNAs, or proteins. Proteins are in all capitals. The circles denote reactions. A species connected to a double arrow is catalytic. Reactions with no products are decay reactions. The labels of reactions also serve as rate constants for the cognate reaction. The Fig. 2.3 is taken from earlier work[2].

This well supported model[2,65,117] applied to conidia can be tied to the hyphal growth model by simply realizing there are two components to the rate of change of any species in the clock (boxes) network (**Fig. 2.3**):

$$\frac{d[FRQ]_{x,t}}{dt} = \frac{d[FRQ]_{chem}}{dt} + \frac{d[FRQ]_{adv}}{dt} = L_3[frq^r]_{x,t} - D_6[FRQ]_{x,t} + \frac{d[FRQ]_{adv}}{dt} \qquad (5)$$

where the first term is the standard rate equation specification on a macroscopic scale[2,65], and last term is an advection (or drift) term near the tip of the hyphae. This advection term is defined by:

$$\frac{d[FRQ]_{adv}}{dt} = \frac{\partial}{\partial x}\,(v(x,t)[FRQ]_{x,t}). \qquad (6)$$

This advection term captures the turbulence at the tip as new media and nutrients are added to the growing hypha.

There is one further feature of the model, tying the state of each gene after a nuclear division to its state before division. The model as described in the supplemental manual allows all possible states of a gene to be passed through mitosis, i.e., on to off, on to on, off to on, and off to off for *frq*, *wc-1*, and *ccg*. The simulator, the realization of the model here, places these genes in a quiescent state during mitosis.

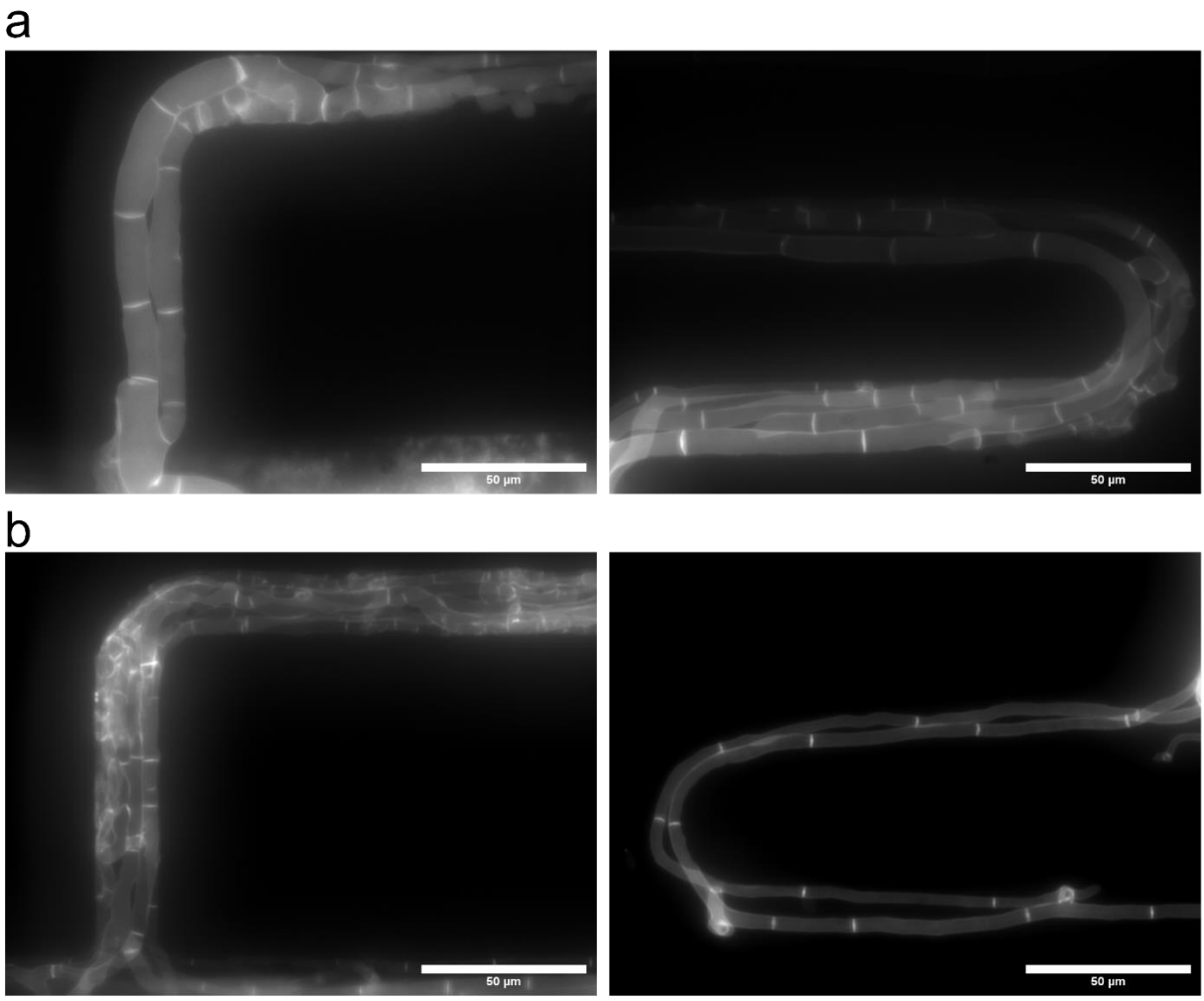


**Fig. 2.4.** Fluorescent images of hyphae stained with calcofluor white demarcate 1-4 hyphae in a channel. (a) Calcofluor white staining on MFNC9 shows two hyphae growing into the opening of the serpentine channels, while the image on the right shows multiple hyphae along the curve of the channel. (b) Calcofluor white staining on a Wild Type (WT strain) shows similar results with multiple hyphae growing into the serpentine channels.

**Variation of hyphal number growing along serpentine channels**

The strain (N2281-3) with a fluorescent recorder on the H1 Histone was used to examine nuclei within hyphae[118]. This method allows us to observe nuclei moving along hyphae, which in turn provided us with a better observation on the number of hyphae present in serpentine channels. From the supplementary video, we observed varying velocity movement of nuclei in each of the hyphae. A total of 1-4 hyphae were observed growing along each of the serpentine channels. To further verify these results, hyphae grown in channels were stained with calcofluor white. It is known that calcofluor white is a non-specific fluorochrome that will bind with chitin and cellulose that are present in the cell walls. Hyphae cells walls were stained by injecting 0.01 % calcofluor white with 0.1% KOH solution into the serpentine chip and incubated for 10 min at room temperature (RT) in the dark. Images were taken under an inverted microscope with a filter set 49 (Zeiss). The stain was effective in differentiating the number of hyphae that are present in the serpentine channels as they grow. In all images observed, intense staining of cell walls and septae were observed in individual hyphae. We were clearly able to differentiate boundaries of the hyphae with the stain (**Fig. 2.4).** A control experiment with Wild Type (WT) strain was carried out to confirm our findings. This allowed us to confirm that the mCherry fluorophore did not interfere with the Calcofluor white staining in the MFNC9 strain. We were able to conclude there were 1-4 hyphae growing into the serpentine channels.

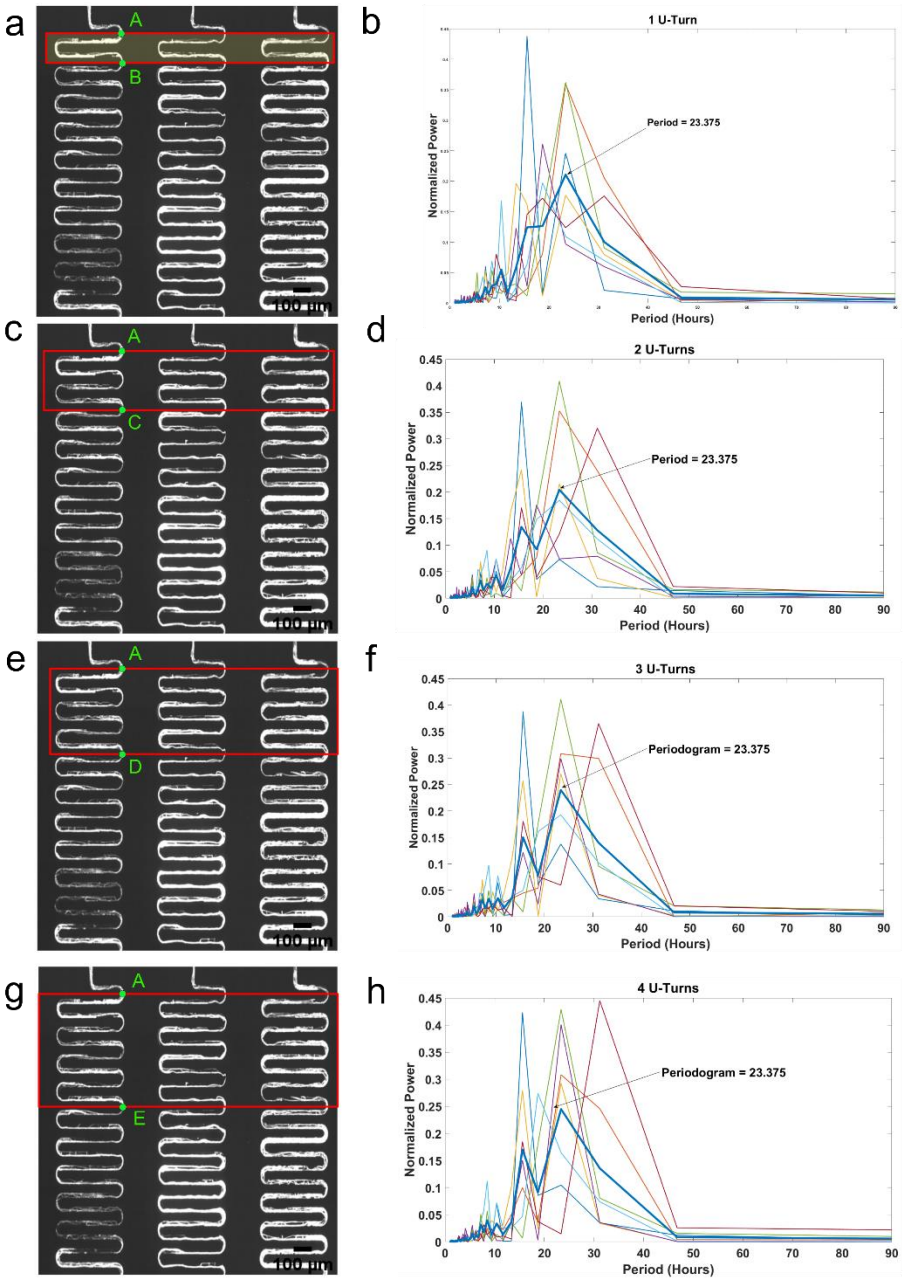


**Fig. 2.5.** Diagram of the results of a U-turn hyphal tracking method we developed with CellProfiler. (a) Fluorescent image of hyphae growing in serpentine channels. One U-turn is defined as a segment from point A to point B for each individual serpentine channel. The image is cropped into a red rectangle as depicted before running through the pipeline on Cell Profiler. (b,d,f,h) Periodograms of individually tracked hyphae, the dark blue line shows the average normalized periodogram of the cropped segment. (c) Fluorescence image of hyphae growing in

the serpentine channels. Two U-turns is defined as point A to point C for each individual serpentine channel. The length of two U-turns of the serpentine channel segment is 1312μm. (e) Fluorescence image of hyphae growing in the serpentine channels. Three U-turns is defined as point A to point D for each individual serpentine channel. (f) Fluorescence image of hyphae growing in the serpentine channels. Four U-turns is defined as point A to point E for each individual serpentine channel. Scale bar:100μm.

**Several strategies to track hyphae were developed**

In order to obtain the best results while tracking their fluorescence and oscillation strength, hyphae were tracked with three methods. One method was to measure only the hyphal tip as the hypha is growing. Three hyphae tips were tracked individually as they grew along the serpentine channel (**Fig. S2.2**) for a period of 30 hours. The fluorescence intensity results were very noisy - if oscillations were present, they were fairly weak and not very noticeable (**Fig. S2.2**). Next, we examined cropped segments across the tiled image horizontally. The segments were identified by the number of U-turns (1,2, 3 or 4 U-turn) across the serpentine channels in a field of view as presented in **Fig. 2.5**. Trajectories of varied segments tracked generally aligned with each other (**Fig. S2.3**) over a period of 98 hours. We observed the periodograms of varying sections of the serpentine channels. We observed that a similar pattern can be observed in periodograms of at least 2 U-turns – 4 U-turns; however, the periodogram on 1 U-turn was not able to capture the features seen in the other three periodograms with multiple U-turns (**Fig. 2.5a**). Hence, we deduced that for further observations, while carrying out fluorescence tracking 2 U-turns will be sufficient when we carry out the data analysis process on fluorescent filaments.

Another reason to use 2 U-turns was that we would not lose any spatial temporal information while tracking the minimal number of U-turns compared to a larger segment.

The last method - Filament tracker (FT) was used to track the individual hyphae as they grew across the full length of the channel individually (**Fig. S2.4**). We tracked the time-averaged fluorescence intensities for each of the individual hypha. We were able to observe clear oscillations down the serpentine channel, and they aligned very well each other. These results imply that the hyphae are synchronized across long distances. We can conlude that both methods of tracking a segment including 2 U-turns as well as tracking the whole filament are recommended.

**Behavior of hyphae in a microfluidic device**

Hyphae from a fluorescent strain (MFNC9[3]) were tracked in a serpentine microfluidics device over 2.8-4 days and their fluorescence, measured as described in Materials and Methods (using FT method), with cell profiler[93]. Each channel is designed to accommodate one or more hyphae[118]. These fluorescent hyphae were compared with a luminescent strain[4] grown in race tubes over 5 days (**Fig. 2.6**). Previous work by Dunlap has shown that circadian oscillations can be observed by tracking its luminescence bands in the race tubes (**Fig. S2.5**).

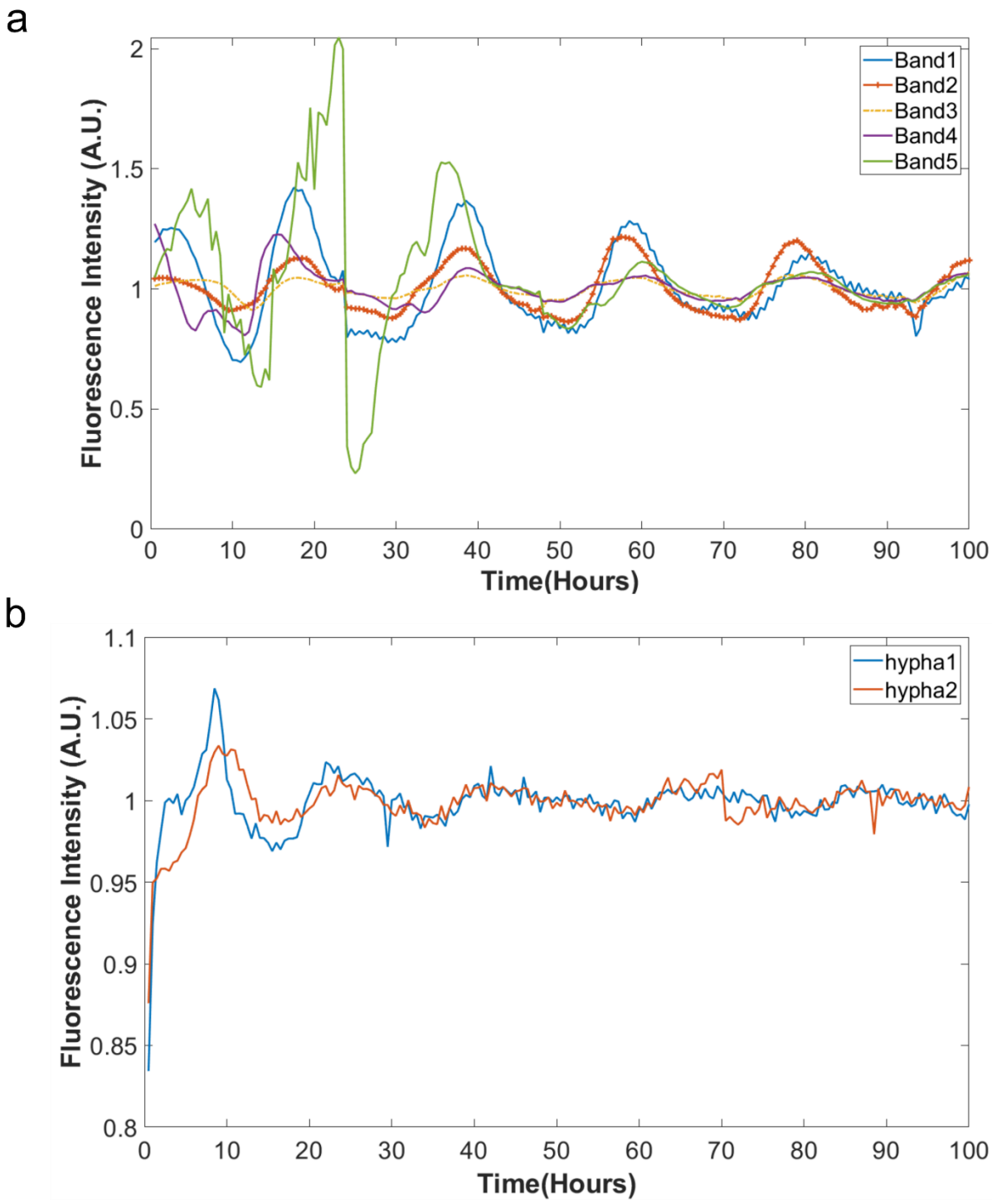


**Fig. 2.6**. A single hypha of MFNC9 (**b**) yielded a circadian rhythm comparable to that of the luciferase strain FRQ-luc-I in race tubes[4] (**a**), but the signal to noise ratio for the hyphae was

8.831 vs. 33.391. Both images were log-detrended with a moving average described earlier[17]. The average periods of bands and hyphae are: (**a**) 20.78 h; (**b**) 19.20 h.

For both hyphae in serpentine channels as well as multiple hyphae in race tubes, they behaved similarly with regard to period of the circadian rhythm. The signal to noise ratio of race tubes is about 4X that of a few hyphae in serpentine channels. Although the number of hyphae tracked in our serpentine chip is far less compared to the race tube, from Fig. 2.6 we can observe that the amplitude of their oscillations is similar. The hyphae are as synchronized as the bands in race tubes.

The signal to noise ratio (as described in Materials and Methods) was computed for 8 bundles of hyphae of the fluorescent strain MFNC9[3] to obtain some idea of the variation in signal to noise as well in period (Takahashi). The results are in **Table 2.1**.

**Table 2.1**. The signal to noise ratio of a bundle of hyphae overlapped with that of race tubes with a luminescent strain (**Fig. 2.6**). Each bundle of hyphae usually has a period of 23 h for strain MFNC9[3], which is similar to that measured in race tubes (21 h)[3].

| Replicate | Signal to Noise[1] | Period (h) |
|---|---|---|
| 1 | 9.381 | 23 |
| 2 | 6.523 | 23 |
| 3 | 2.921 | 23 |
| 4 | 34.697 | 23 |
| 5 | 13.552 | 23 |

| | | |
|---|---|---|
| 6 | 3.936 | 23 |
| 7 | 11.477 | 17.5 |
| 8 | 21.205 | 23 |
| Average (+/- standard error) | 12.9615 (+/-3.7309) | 22.3125(+/-0.6875) |

[1]See Materials and Methods.

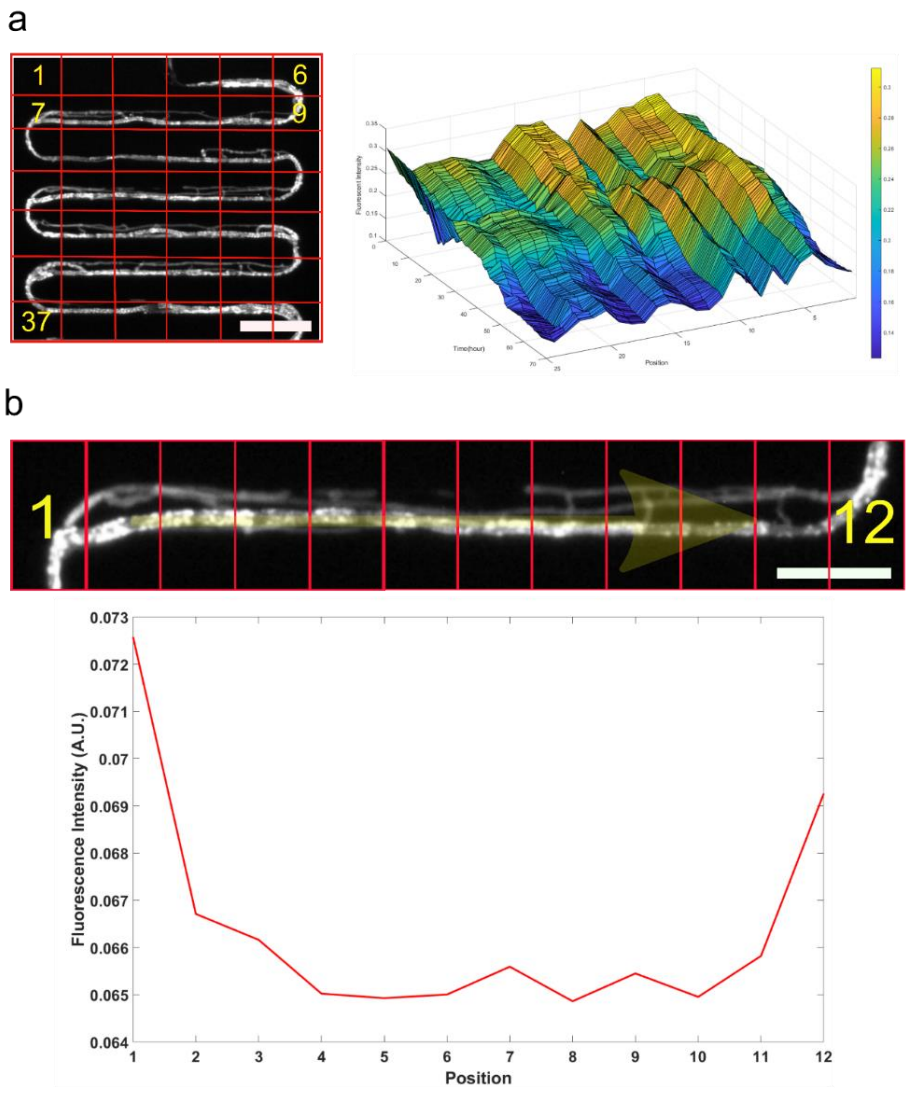


**Fig. 2.7.** Fluorescence intensity pattern varies along positions in the serpentine channel. (**a**) Left: Florescence image of hypha located in a segment of 2 U-turns of the serpentine channel. 42

positions were labelled beginning from the top left corner of the image to the right as shown in the scheme on the left. Right: Spatio-temporal images of the fluorescence intensities observed at different time points for a particular position in the channel. Color bar indicates the fluorescence signal intensity. Scale bar:10µm. (**b**) Fluorescence intensities acquired at a specific cropped out area of a serpentine channel. Twelve positions shown the plot correspond to scheme shown on top. Scale bar: 100µm.

Here we showed that a circadian oscillator exists in each bundle of hyphae with little variation in period. The period of MFNC9 is similar to that (21 h) in race tubes[3] and in conidial cells in a **microfluidics device**[17,31].

**Growth dynamics on serpentine chip**

Time-lapse images obtained during confined growth in the serpentine channels were used to build spatio-temporal diagrams using 42 sectors. such as the one displayed in **Fig. 2.7a**. This graphical representation allowed us to visualize the variation of fluorescence intensities spatially at different sections of the channel. Interestingly, on such a diagram, as we look across the time series for each individual position, there is no significant shift in the pattern of the fluorescence intensities. We do not observe oscillations or huge changes at positions that present a peak. These peaks seem to occur at most of the U-turn positions in the channel. To further explore the growth dynamics observed, we examined the mean fluorescence of a hypha in a cropped image consisting of one small section of a U-turn and one of the straight sections of the channel divided into 12 sectors. As seen in **Fig. 2.7b** there is a higher fluorescence intensity recorded at both ends of the U-turn when compared to the straight channels.

**Synchronization of hyphae in serpentine channels**

Previous work showed that synchronization exists in a "big chamber device" and microwell devices[119] while cells were in their conidial form. We sought to further explore whether synchronization is observed through hyphae that are growing in their own serpentine channels along the whole device. We examined the synchronization between channels as shownin **Fig. S2.6**. This was measure by a synchronization measure known as the Kuramoto order parameter (K) [87] between different segments and is defined as:

$$K = \left\langle \left| n^{-1} \sum_{j=1}^{n} \exp(i\mathrm{M}_j) - \left\langle n^{-1} \sum_{j=1}^{n} \exp(i\mathrm{M}_j) \right\rangle \right| \right\rangle$$

where K represents the phase coherence, and $M_j$ is the phase of the jth serpentine segment with hyphae. The quantity n is the number of hyphal segments being compared (n = 2 for two hyphae segments in neighboring serpentine channels). The order parameter K would be 1 if both channels were equally phase synchronized while it would be 0 in incoherent states. The synchronization measure (K) calculated between any two segments across the channels was at least 0.7526. The high degree of phase synchronization across channels indicates that the hyphae were all synchronized although they were located in separate serpentine channels. This results were supported by the low K value of K = 0.0322 +/- 0.0007 that were calculated on isolated 1-cell droplets[62], which were almost close to zero as expected. At the other extreme is a "big chamber device", in which cells were tightly packed into an artificial tissue. In this situation the measured order parameter was K > 0.91 between different fields of view in a transect across the artificial tissue[120]. Furthermore, we also looked at the K values for randomly generated white noise oscillations and obtained a result of 0.531 (described in Materials and Methods).

**Table 2.2.** Measures of synchronization (K) between 6 segments of different serpentine channels along the serpentine chip.

| Kuramoto K | Serpentine 1 | Serpentine 2 | Serpentine 3 | Serpentine 4 | Serpentine 5 | Serpentine 6 |
|---|---|---|---|---|---|---|
| Serpentine 1 | - | - | - | - | - | - |
| Serpentine 2 | 0.8272 | - | - | - | - | - |
| Serpentine 3 | 0.7937 | 0.7903 | - | - | - | - |
| Serpentine 4 | 0.7526 | 0.7866 | 0.7901 | - | - | - |
| Serpentine 5 | 0.8239 | 0.8763 | 0.8193 | 0.8196 | - | - |
| Serpentine 6 | 0.8148 | 0.8027 | 0.9045 | 0.8107 | 0.8511 | - |

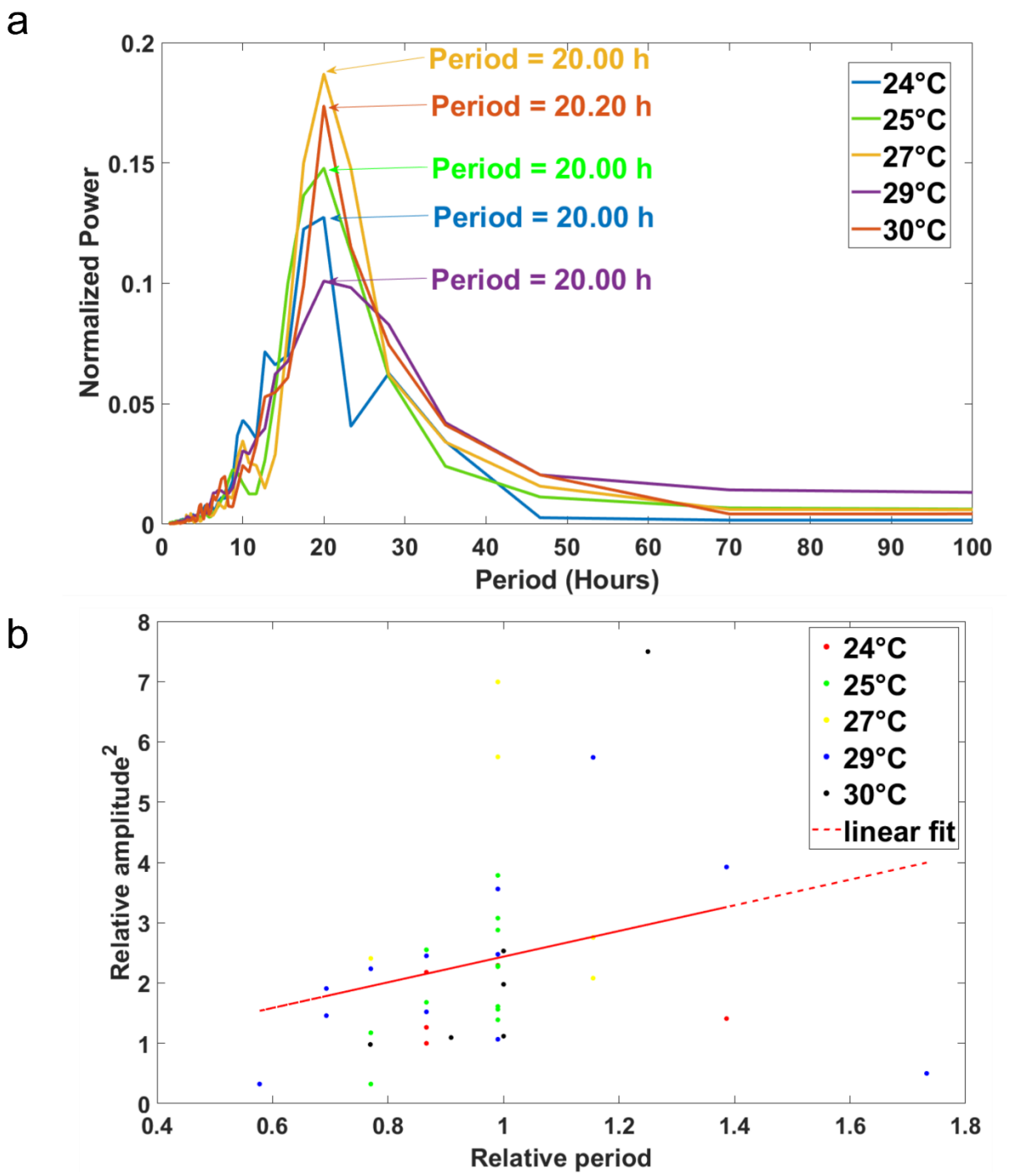


**Fig. 2.8**. Single hyphae display temperature compensation properties. (**a**) Average normalized periodogram at five varying temperatures over the physiological range of *Neurospora crassa* is shown. Each average normalized periodogram at each temperature is based on over 5 (24°C),12 (24°C),5 (27°C),12 (29°C),6 (30°C) hyphae respectively. (**b**) The coupling of the relative amplitude squared plotted vs. relative period.

The x-axis is the relative period, it is calculated by the period of each tracked hypha at the observed temperature and dividing it by the average period at 30°C. The y-axis would be the relative amplitude squared. This is calculated by obtaining the maximum amplitude squared of each tracked hypha and dividing it by the average amplitude squared of the reference temperature (30°C). Single hyphae are color coded depending on their temperatures. The correlation (r) of amplitude squared and period was r = 0.2696 (Fishers z = 0.2765, P < 0.0001) The Spearman rank correlation ($r_s$ ) was $r_s$=0.3886 (P =0.0132 )

**Hyphae display clock-like properties**

With the serpentine microfluidic platform developed and exhibiting circadian rhythms (**Fig. 2.6**), two further defining properties of a biological clock were examined, light entrainment and temperature compensation. Having demonstrated the existence of biological clocks in single cells[121] while they were restrained in growth and in their conidial form,[31] our goal here is to verify a biological clock exists at the next life stage, growing hyphae. Experiments were carried out over a range of 24-30°C as seen in **Fig. 2.8**. If temperature compensation is present at the single cell level, the period length of tracked hyphae would not change over the temperature range. This was quantified by the $Q_{10}$ value measure as seen in Equation:

$$Q_{10} = \left(\frac{P_1}{P_2}\right)^{\frac{10}{T_1 - T_2}}$$

where the reference temperature is denoted as ($T_2$) at 30°C and the periods, $P_1$ and $P_2$, the periods are at temperatures $T_1$ and $T_2$, respectively. The $Q_{10}$ values were close to 1 (**Table 2.3**), demonstrating there were small fluctuations of period with temperature. Hence, we were able to show that single hyphae demonstrated temperature compensation characteristics.

We would like to explore the mechanisms of temperature compensation from data in **Fig. 2.8b**. Previous work [31] has shown that there is evidence of amplitude-period coupling that is consistent with presented clock models exhibiting temperature compensation properties[122]. We examined the coupling of relative amplitude to relative period in **Fig. 2.b** in over 40 single hyphae. The highly significant positive slope ($P < 0.0001$) of relative amplitude squared on relative period further strengthens the prediction that coupling exists as seen in three families of clock models.

**Table 2.3**. Temperature Coefficient $Q_{10}$ over a physiological range of temperatures (T1) provided evidence of temperature compensation. Standard Errors (SE) for temperature coefficient were computed using the propagation of error method.

| Temperature ($T_1$) | 24° C | 25° C | 27° C | 29° C |
|---|---|---|---|---|
| Period (Hours) (+/-2SE) | 20.00 (+/- 2.0335) | 20.00 (+/- 0.4336) | 20.00 (+/- 1.4320) | 20.000 (+/- 1.8819) |
| $Q_{10}$ (+/-2SE) | 1.0167(+/- 0.0369) | 1.113(+/- 0.0124) | 1.0337(+/- 0.0906) | 1.1046(+/- 0.0416) |

The next attribute of a biological clock is that cells can be light entrained. We carried out time-lapse experiments of *Neurospora crassa* hyphal growth using a developed upright microscope setup with a LED light source for light entrainment (see Materials and Methods). In order to investigate the intrinsic behavior of the clock, we entrained the hyphae to a Light:Dark

(L/D) of 6:6hr L/D cycle and a 36:36hr L/D cycle under constant conditions (LED with 3700 lux) and temperature (30°C), shown in Fig 2.9. This method allowed us to track growing hyphae in individual serpentine channels while carrying out the entrainment process.

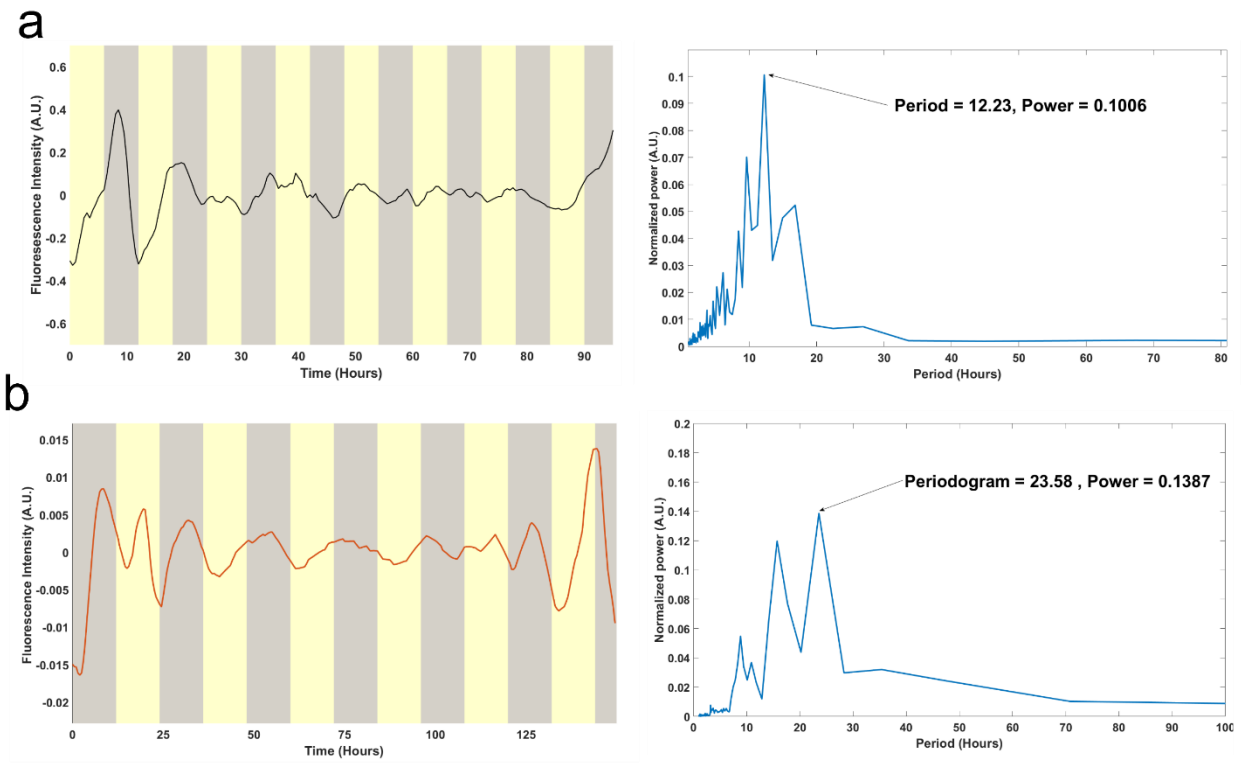


**Figure 9**. Entrainment by light in *N. crassa* hyphae in serpentine channels to a 12 hour (**a**), 24 hour (**b**) day. (**a**) Left: Average of 9 single hyphae trajectories detrended under 6 hour L/D regimen. Right: Average periodogram of hyphae of 12 day length. (**b**) Left: Average of 16 single hyphae trajectories detrended under 12 hour L/D regimen. Right: Average periodogram of hyphae of 24 day length.

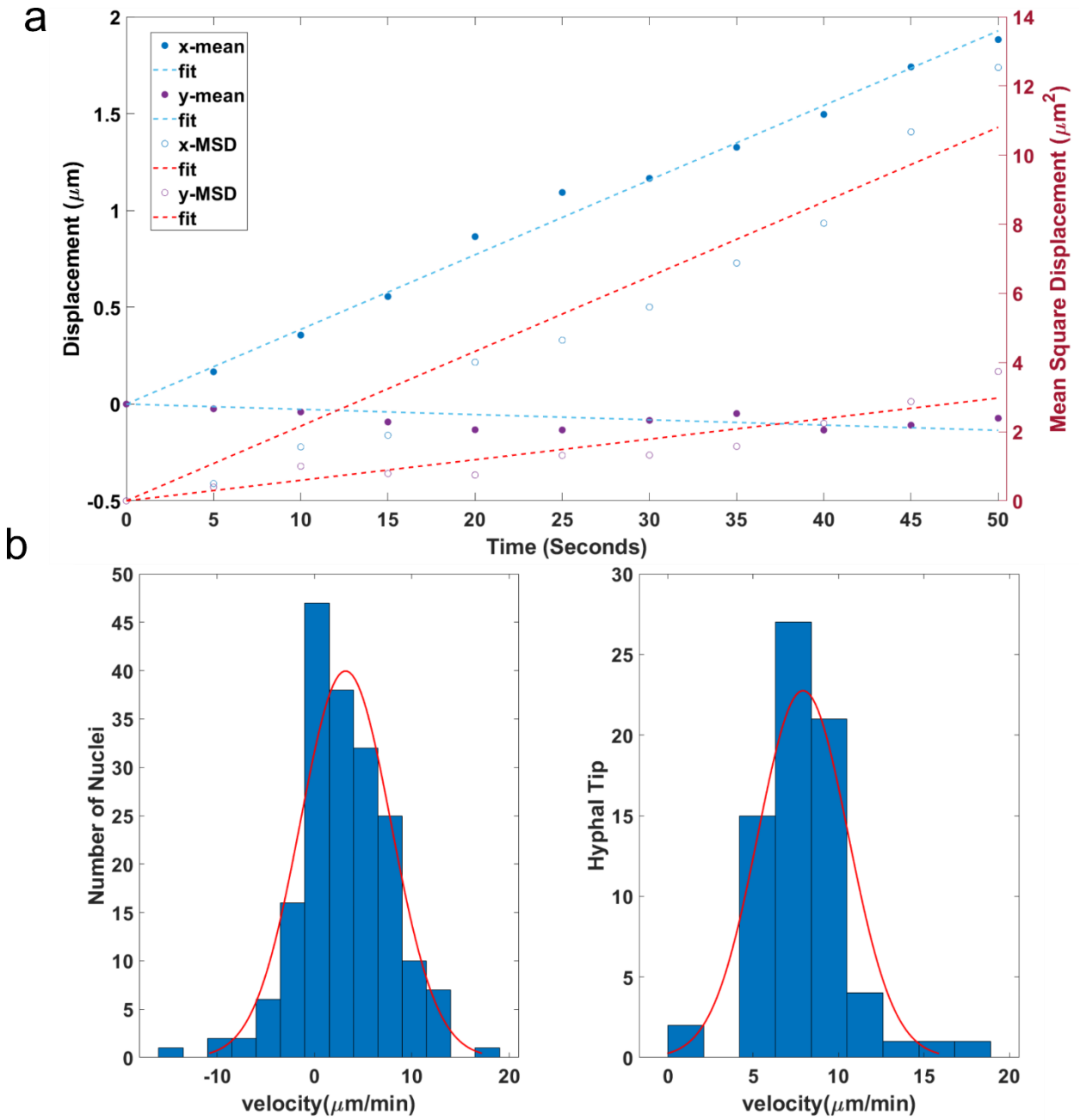


**Fig. 2.10**. Overview of velocity profiles obtained with nuclei tracking in serpentine channel. (**a**) Graph of drift velocity as well as diffusion velocity on the relative time. The x-y coordinates of each nucleus (139 nuclei) were tracked over 11 sequential images (taken at 5s intervals) and plotted against time. Each point in the graph is plotted with the mean displacement travelled from the origin over 11 sequential images.The drift velocity calculated in the x-direction was

2.316μm/min. The Pearson correlation was r = 0.9961 (Fishers z =3.1146, P = 9.75e-11) and the Spearman rank correlation ($r_s$ ) was $r_s$=1 (P = 0). The drift velocity in the y-direction was -0.162μm/min. The Pearson correlation (r) for the latter was r = -0.5509 (Fishers z =-0.6197, P =0.0790) while the spearman rank correlation ($r_s$ ) was $r_s$= -0.5364 (P =0.0936) .The diffusion coefficient in the x-direction was 12.97 $\mu m^2$/min . The Pearson correlation was r = 0.9833 (Fishers z =2.3872, P = 5.8153e-08) and the Spearman rank correlation ($r_s$ ) was $r_s$=1 (P = 0).In the y-direction it was 3.57$\mu m^2$/min. The Pearson correlation was r = 0.9376 (Fishers z =1.7181 P =2.02e-05) while the spearman rank correlation ($r_s$ ) was $r_s$= 0.9636 (P =0) (**b**) Left: Histogram of the velocity profile for 187 nuclei was plotted. Right: Histogram of the velocity profile for 72 hyphal tip time series.

**Specifying the velocity profile, drift and diffusion velocities of the hyphal clock model**

To study the nature of flow in hyphae of *N.crassa*, we obtained the velocity profile by fluorescence microscopy. The GFP-tagged histone (for imaging nuclei) provided us with the movement of nuclei while the hyphae elongated in the channels. CellProfiler allowed tracking of nuclei and obtaining their x-y coordinates. The drift velocity in the x-direction calculated was 2.316μm/min while the drift velocity in the y-direction was -0.0014μm/sec which was almost close to 0. The diffusion coefficient calculated was 12.97 $\mu m^2$/min while in the y-direction it was 3.57$\mu m^2$/min. The velocity profile, drift velocity (due to advection), and diffusion velocity are features of the hyphal clock model introduced in the modeling section. We investigated the relationship between the rates of the nuclei movement and hyphal elongation.

**Behavior of the hyphal clock model**

First the growth of the hyphae is shown in **Fig. 2. 11**. As the nuclei divides there is an initial growth in the density of nuclei until a steady state in nuclear density is achieved along the serpentine channel or race tube (**Fig. 2. 11A**). The velocity profile is also constant and established at the beginning of the growth experiment (**Fig. 2. 11B**). The velocity profile is near zero at the beginning of the race tube or channel and rises to a constant value as new material is added to growing hyphae(s). The food density is also uniform after a step up (**Fig. 2.11C).** To give more flexibility in initial conditions for the food and velocity profile these can be specified as a product of step functions in the simulator (see Supplement).

Previous studies were done on the measurement of nuclei movement during the growth of hyphae; however, the microfluidic device would introduce additional restrictions for the growth or branching hence additional data needs to be collected for the hyphal clock model.

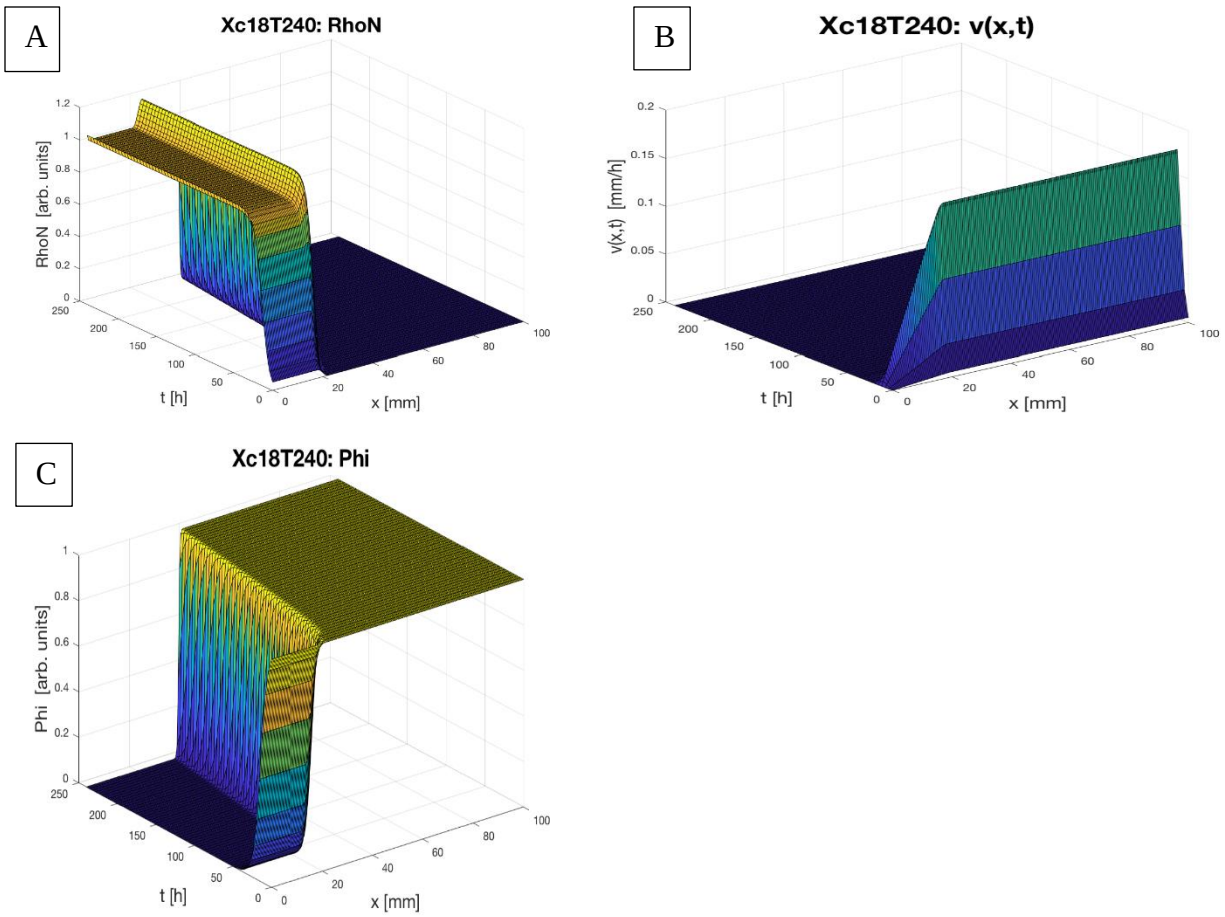


**Fig. 2.11**. The nuclear density, velocity profile, and food distribution are specified by the growth model as a function of spatial location (x) and time (t): (A) nuclear density $\rho(x,t)$; (B) initial velocity profile $v(x,t)$ for the growing hyphae(s); (C) food distribution $\Phi(x,t)$.

The other aspect of the model is the clock in the hyphae (**Fig. 2.12**). The genes are being swept along in each hypha in the nuclei. They are producing mRNAs and proteins along the race tube or serpentine device. Each of these molecular species have a velocity, position, and concentration in the growing hyphae as shown. The model shows the characteristic 21 h period in the FRQ, WCC, and CCG proteins expected in the device. The bands in all three proteins that are visible in race tubes have the characteristic period of 21 h similar to that in the serpentine

device (Table 2.1). What is also interesting is that the hypothesized communication signal in the media of the device around a growing hypha also displays the characteristic periodicity. This hypothesized signal acts to provide the synchronization signal between nuclei.

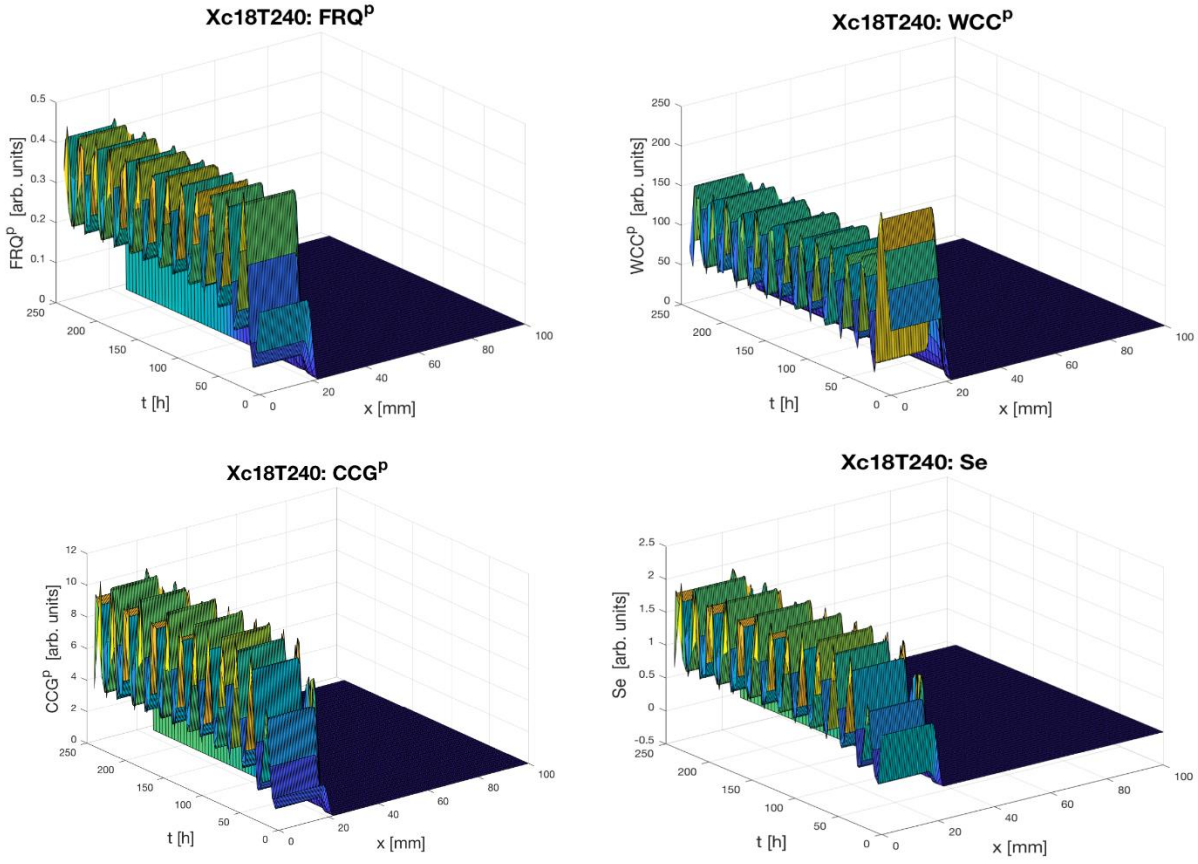


**Fig. 2.12**. The hyphal clock model displays the "bands" observed in race tubes and the periodicity of the serpentine device. (A). The FRQ protein concentration is graphed as a function of spatial location (x) along the device and time (t); (B) the WCC protein concentration is graphed as a function of spatial location (x) along the device and time (t); (C) the CCG protein usually observed in the device is graphed as a function of spatial location (x) and time (t); (D) the communication signal in the media (Se) is also graphed as a function of spatial location (x) and time (t).

**Discussion**

The current study provides us with a substantial insight into a rather neglected area of cell synchronization biology. Previously, we were able to show synchronization at a macroscopic limit for single cells in a big chamber microfluidic device. [119] A microwell device was also fabricated to observe the synchronization of cells at a much lower density.[119] Despite the increasing evidence for phase synchronization of cells, these were limited to *N. crassa* cells that were prohibited from growing.

Hence, we continued the exploration of cell synchronization by permitting hyphal growth with sufficient media. The chip (Fig. 2.1) was designed to allow precise control of the cellular environment with a fixed media flow rate. We demonstrated the existence of clocks for individual hyphae in a microfluidic chip (Table 2.3 and Fig. 2.10). The width of the serpentine channel opening was determined to restrict the number of hyphae growing into channels. This allowed us to track single hyphae without much difficulty. We were able to observe clear oscillations that were comparable to luminescent bands tracked in race tubes[4]. An interesting result seen while tracking luminescence in race tubes is that the synchronization is seen over long distances 30-60 mm (**Fig. 2.6**). While velocities of cytoplasmic flow have been measured from 0.2-60 $\mu m$/s in *N. crassa*, this is still two orders of magnitude two slow to explain the synchronization on the scale of 30-60 mm. For example, for a small metabolite with radius 13.05nm could travel no further than 313.2nm in a day to synchronize cells at the distance of 30-60 mm[120]. To test whether advection could be an explanation to how they synchronize, we calculated the drift velocity (advection). As the advection rate was fairly low (2.316μm/min), presumably it is not fast enough to promote synchronization. The diffusion coefficient for

*N.crassa* gave us an estimation of the mean size of nuclei to be 2.269μm (**Fig. 2.10**), which is comparable with prior measurements (1.40-3.40$\mu m^3$ ).The average hyphal tip velocity was calculated to be around 7.9188μm/min, a factor of four faster than the drift nuclei velocity.

Several hypotheses have been proposed for how cell synchronization would occur in this microfluidic chip. Previously, we presented experimental evidence that a chemical signal diffusing in the media would cause synchronization between cells[119,123]. In this scenario where cells are allowed to grow, the chemical signal could be travelling across the hyphae in one-dimension. As we have shown that there is a drift velocity within the cells (**Fig .10**), and the signal could be carried by advection within the hyphae as they elongate. There could be a switch between advection/diffusion as hyphal tip velocity varies at various points in the channel. An alternative hypothesis suggested is cell-to-cell contact results in synchronization to occur[44,110]. There is a possibility that stochastic intracellular noise independently plays a positive role in phase synchronization of cellular oscillators[17,63]. Another possible explanation for this phenomenon is the presence of cell cycle components that result in synchronized nuclear divisions in Neurospora[124]. There is a possibility that there is no sole hypothesis to explain cell synchronization. Further research should be conducted in the future to better identify which hypothesis is supported. This can be done by introducing cell perturbation systems [91,125-127], for example time-dependent cyclic perturbations or varying media flow diffused into the serpentine chip[96]. These can be carried out by making modifications to our current device.

Our fluorescence trajectories demonstrated an interesting increasing trend in fluorescence intensity at the U-turn sections of the serpentine channel (**Fig. 2.7**). We hypothesize that these

could be a result of higher possibility of branching around the U-turns due to the device geometry. There have been studies using time-lapse live cell imaging of *N. crassa* in maze like microfluidic structures to observe how constraining geometries determine fungal growth[128]. They observed a hit & split phenomenon that would occur instantly after the contact between a hypha and a constraining structure. Recently, a report was made that *N. crassa* is considered to be a fast-growing fungus that possesses the ability to cover new available nutrient-rich space[129]. However, when placed in spatially confined areas with obstacles, this may cause multiple new polarity axes to form, resulting in branching to occur[129]. An alternative hypothesis is the possibility of a change in the diffusion rate for hyphae growing in the U-turns. A decrease in the diffusion rate may allow branching to occur more frequently around the curved area of the channel compared to straight channels. To test these hypotheses, a microfluidic chip with varying geometries can be fabricated parallel to each other on the same device for simultaneous tracking.

**Conclusion**

This study illustrates how a high-throughput serpentine chip was fabricated to demonstrate the existence of cellular clocks in individual hyphae, the dominant life stage of filamentous fungi. Hyphae within the device are also phase synchronized with respect to their individual hyphal clocks. The device used provides multiple serpentine channels to facilitate controlled hyphal growth of *N. crassa*. Trapped hyphae successfully grew and elongated across the serpentine channels. Th resultant hyphae grew down narrow growth channels that enabled measurements on their fluorescence intensities. Since there is a possibility that clock communication may occur thorough phase, a new microfluidic device needs to be fabricated to

allow hyphae that are entrained at different phases to synchronize with each other. This is the first report of the existence of cell clocks in growing individual hyphae with a supporting hyphal clock model. The platform has the potential to aid us in our understand of the growth process of *N.crassa* and other fungal species, and provides a broadly applicable research tool to introduce perturbations for cells to study fundamental processes, such as the clock..

## Materials and Methods

### Fluorescent strains.

For observation of the clock strain *bd,ccg-2P:mCherry* was used[3] (MFNC9), where ccg-2P: mCherry denotes a *clock-controlled gene-2 Promoter* region (*ccg-2P*) fused in frame with a mCherry recorder. For observing nuclei the fluorescent strain mat A his-3+::Pccg-1-hH1+-sgfp+ [118] (N2218-3 ) was used.

### Microfluidics Device design and fabrication.

The microfluidic device (**Fig. 2.12**) contains a cell loading channel with an inlet to load an agar plug, one medium loading channel, and 106 serpentine regions. The serpentine channels resemble those in other devices to allow hyphae to grow several days[95,130] within the device. The device features channels of two varying heights, where the medium loading channel (30 μm), and serpentine regions (15 μm) were fabricated with two photomasks. The device consists of four inlets, one inlet to deliver media, a medium outlet while the other two have plugs attached to ensure a constant flow of media across the serpentine channels, as well as xx serpentine growth channels. The 15 μm serpentine regions were added with SU-8 3010 (MicroChem, Westborough, MA). The second step was to have 30 μm medium loading channel fabricated with SU-8 2025 (MicroChem,

Westborough, MA). The channel heights were measured by a profilometer (Veeco Instruments, Chadds Ford, PA). Prior to PDMS casting, the fabricated master mold was vapor covered with (tridecafluoro-1,1,2,2-teterahydroctyl) trichlorosilane for 15 minutes and subsequently heated to 120°C for 10 minutes. The microfluidic device were built with PDMS (10:1 w/w) by a standard PDMS replica molding technique[131]. Polydimethylsiloxane (Dow Corning, Midland, MI) were poured onto the silicon wafer, baked at 80°C for 2 hours, and bonded on a glass slide to produce the final device.

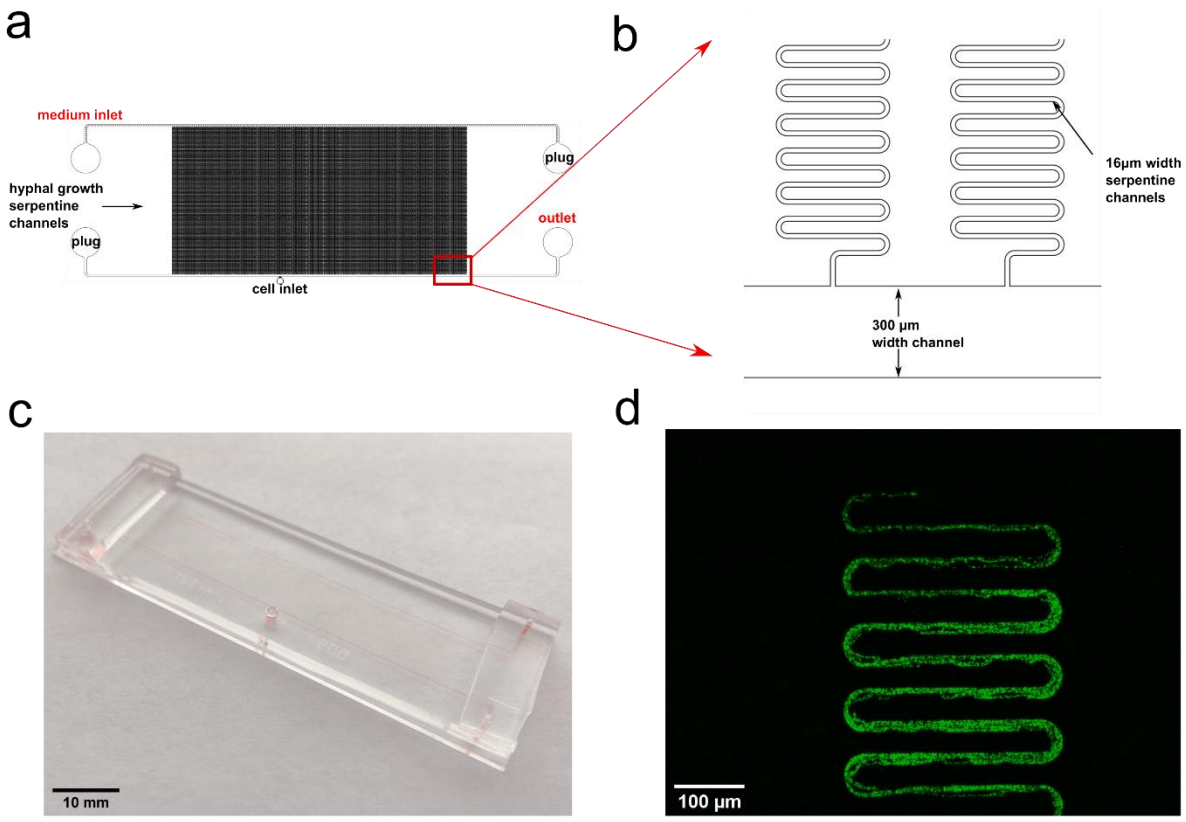


**Fig. 2.13. Microfluidic platform that was used to track hyphae growth.** Serpentine microfluidics device allows observation on 1-95 hyphae over 6 days**. (b)**The channel for hyphae growth is 16 microns wide and 198,241 $\mu$m long. The dimensions of the serpentine channel were chosen to accommodate only a few hyphae. A hypha can range from 8-15 $\mu$m[118]. (c) A

photo of the serpentine chip. The dimensions of the device are 65500 $\mu$m x 20150 $\mu$m and features 95 parallelized serpentine channels. A cell inlet port with a 2 mm diameter is located in the middle of the larger medium inlet channel. (d) Visualization of a *N.crassa* strain N2218-3 expressing a histone H1-GFP growing along the serpentine channels.

**Inoculation of agar plug and hyphae growth into serpentine microfluidics device**.

In a typical procedure, all microfluidic channels were initially primed with 0.1% glucose media to ensure the reduction of bubbles. The agar plug that was prepared is placed in the middle inlet and sealed with a 3D printed plug. A 3 mL syringe with 0.1% glucose media was constantly perfused into the medium infusion channel throughout the time lapse experiment. The waste outlet was connected to a conical tube to collect excess medium. The device was then placed under constant light exposure (5370 lux) for at least 2 hours before placing in the dark for imaging. Hyphal growth generally started occurring after a period of 6 hours until they begin to grow into the nearest serpentine channels. After required light exposure, system was placed on the stage microscope.

**Image acquisition**.

Live cell imaging was done with a CCD camera (AxioCam HRm, Carl Zeiss Microscopy, LLC, Thornwood, NY) to record the fluorescence intensity of the cells through a microscope (Axio Imager M2, Carl Zeiss Microscopy, LLC, Thornwood, NY) with a motorized x-y stage (Mechanical stage 75 × 50 R, Carl Zeiss Microscopy, LLC, Thornwood, NY) in a dark room. The excitation light used was guided through a filter set (Filter Set #61HE, Carl Zeiss Microscopy, LLC, Thornwood, NY) at 585/35 with emission at 645/60. Images were taken every

30 minutes with an exposure time of 1200ms. Images were stitched and exported as a 8-bit gray scale to accommodate for the large file size due to the length of the time-lapse experiment. Zeiss A2 inverted microscope was used to observe calcofluor labelling with the corresponding filters.

**Processing of hyphal images.**

Fluorescence images were tracked using a pipeline built with CellProfiler. Images were first converted to 8-bit files and cropped based on the segments to analyze to accommodate for the processing time as well as the size the software can handle. For each experiment, custom Python codes were written to extract required data. Data were then exported to MATLAB. Custom MATLAB scripts were utilized to produce periodograms or fluorescence trajectory plots. Each fluorescence trajectories were detrended[17] with a 24-hour moving average. Their periodograms were computed.

**Processing of race tube time lapse movie.**

The race tube data on FRQ-luc-I were downloaded for Supplemental Movie File 4 at https://ec.asm.org/content/7/1/28/Fig.s-only[4]. A python program(vti) was written to convert the video to an image sequence, which was then processed as with the hyphae images.

**Measuring signal to noise ratio.**

The estimated mean amplitudes of signal and noise from the experimental data were applied to calculate the signal-to-noise ratio for the fluorescent intensity signals of hypha and race tube data. The built-in smooth function in MATLAB was applied to the original experimental data to estimate the signal, and the window size of the smooth function was 2.5

hours. The mean amplitude was calculated using the first three days of signal data. Then the noise was estimated by taking the absolute values of the differe1nce between the original data and the estimated signal. Then the mean amplitude of the noise was calculated using the first three days' noise data. The signal-to-noise ratios of the hyphae's' fluorescent intensity signals were then calculated by using the mean amplitudes of signal divided by the mean amplitude of noise.

**Generation of white noise for Kuramoto K calculation**.

The noise model generates 127 trajectories, and each trajectory would have 480 data points. All initial values of the trajectories are set to 0, and for each corresponding step, white noise is added to the trajectory respectively. The trajectories were detrended with a 24-hour moving average over time (Supplementary Fig S7). The synchronization was calculated among the trajectories and Kuramoto K is 0.53.

# CHAPTER 4

# *IN VIVO* METABOLOMIC AND RNA PROFILING DATA SUPPORT AN AROMATIC ALCOHOL AS A QUORUM SENSNING SIGNAL FOR PHASE SYNCHRONIZATION OF THE CLOCK IN SINGLE CELLS OF NEUROSPORA CRASSA

---

Xiao Qiu, Wu Yue et al. To be submitted to (Scientific Report)

**Abstract**. Recent experimental evidence supports the presence of a density-dependent metabolic switch in Ethanol production in a *qa-x* background in *Neurospora crassa*, providing a potential biochemical mechanism by which aromatic alcohols serve as quorum sensing signals for the phase synchronization of the biological clock. Here we test whether or not available RNA profiling and Continuous *in vivo* Metabolism-NMR data are consistent with the hypotheses that: (1) quorum sensing (QS) in Ethanol production is the mechanism in phase synchronization of the clock; (2) the QS signal is (are) an aromatic alcohol(s); (3) the gene (NCU03643) encodes the quorum sensing regulator. Ensemble methods were used to fit this hypothesis successfully to RNA profiling and CIVM-NMR data in four experiments at high and low density in *qa-x* and Wildtype genetic backgrounds. In this way a detailed biochemical mechanism is put forward to explain the phase synchronization of clocks in single cells in *N. crassa*.

**Significance**. A fundamental problem in collective behavior is understanding the phase synchronization of cellular oscillators[132]. This problem arises at the molecular level in a variety of contexts including in the origin of glycolytic oscillations in *Saccharomyces cerevisiae*[77], in the spiking of $CA^{++}$ signaling pathways[38,39], in synchronizing hyphal clocks in cyanobacterial Anabena filaments[110], and in the synchronization of cellular clocks in *Neurospora crassa*[133]. Using microfluidic measurements on single cells, the clocks in single cells[31] of *N. crassa* were shown to phase synchronize in a population of between 829-5198 cells through a hypothetical quorum sensing signal with a maximum radius of 13.05 nanometers[133]. This phase synchronization was also shown to be density-dependent[133]. The challenge is understanding the biochemical basis of this quorum sensing behavior for phase synchronization of a population of cellular oscillators.

One clue to the biochemical basis of quorum sensing in *N. crassa* came from using new Continuous *In Vivo* Metabolism-NMR or CIVM-NMR on classic mutants of the *qa* gene cluster[94], which has been studied for over 60 years as a model of eukaryotic gene regulation[72,134,135]. This gene cluster allows *N. crassa* to use quinic acid (QA) as a sole carbon source[134]. There are 7 genes in this cluster tandemly arrayed in a 17.5 kilobase stretch near the centromere on linkage group VII[136,137], but there is still one member of this cluster, the *qa-x* gene, for which there is no known function[138]. Its only known phenotype is the accumulation of a pink-brown color in the media[139,140]. Using CIVM-NMR, the function of *qa-x* was uncovered – the *qa-x* mutant yielded a block in metabolism with an accumulation of homogentisic acid (HGA), as in alkaptanuria patients[141]. This block occurs downstream of Tyrosine degradation (**Fig. 3.1**). The *qa-x* mutant also readily displayed an interesting density dependent biochemical switch from Ethanol consumption at low cell density to Ethanol production at high cell density[141].

Aromatic alcohols have been implicated in quorum sensing in *S. cerevisae*[92] and occur upstream of HGA (**Fig. 3.1**). With the block below HGA in a *qa-x* mutant, the flux around the aromatic alcohols would suggest Tyrosol should accumulate as the organism grows. The implication is that Tyrosol could be utilized as a quorum sensing signal for the metabolic switch, allowing the switch from Ethanol consumption to production at higher density. This is the hypothesis put forward[141]. Based on this hypothesis a biochemical mechanism for clock phase synchronization is that: (1) the quorum sensing signal (QS) for the switch in Ethanol production is Tyrosol accumulation[141] and is the same quorum sensing signal for phase synchronization of cellular oscillators[133]; (2) Tyrosol is the hypothetical QS signal in the clock for phase

synchronization[133] (**Fig. 3.1**); (3) the gene NCU03643 encodes the quorum sensing regulator[135]. We now test this biochemical mechanism with both transcriptional profiling data on the *qa* cluster[72] and CIVM-NMR data on central metabolism in *N. crassa*[94].

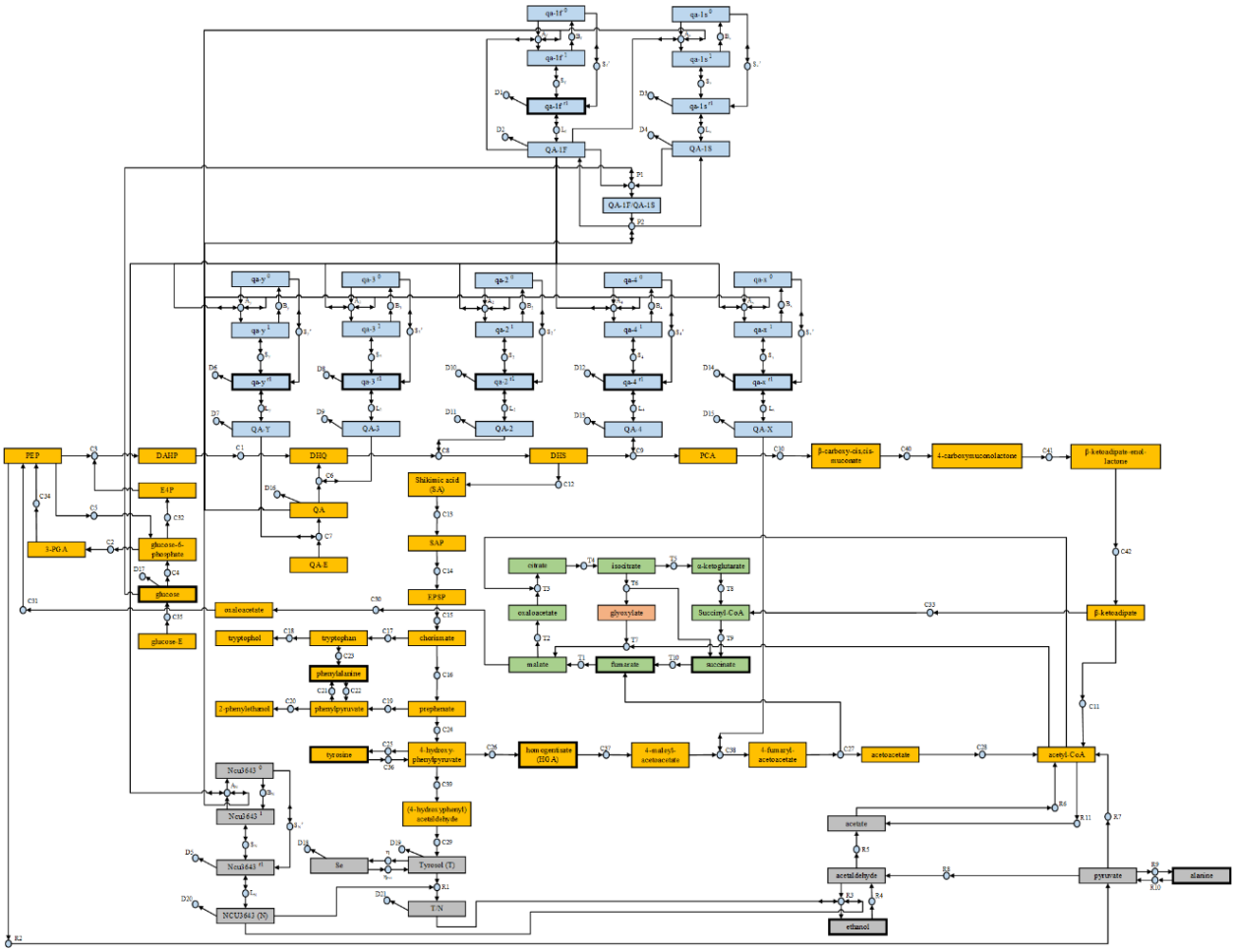


**Fig. 3.1**. Metabolic model with allosteric clock regulation. Across the top are the qa cluster genes under the control of the QA-1F transcription factor and QA-1S repressor (in blue). Additionally the NCU0343 encoded activator (in grey) is under QA-1F transcriptional control[135]. QA metabolism is in orange. Aromatic amino acid metabolism is in orange. QA pathway entry into the TCA cycle is in green. Quorum sensing regulation is in grey. Fermentation is in grey. Boxes denote reactants and products. Circles denote reactions. A double arrow indicates a catalytic step,

not reversibility of the reaction. Inactive genes, active genes, mRNAs, and proteins are denoted by gene$^{0}$, gene$^{1}$, gene$^{r}$, and GENE respectively. There are 16 measured metabolites, and all mRNAs are measured by Northerns[72]. Measured species have a thicker border.

**Model**

The genetic network consists of the *qa* gene cluster and cognate mRNAs and proteins (in blue) and parts of metabolism under *qa* cluster control, including aromatic amino acid biosynthesis and degradation (in orange), glycolysis (in orange), TCA cycle (in green), and fermentation (in grey)[135]. Embedded in this network is a quorum sensing mechanism controlling the switch between Ethanol production to and from Ethanol Consumption. Key components include a regulator (NCU03643) and a quorum sensing signal (in grey)[41].

Quorum sensing has been hypothesized to be a mechanism for the synchronization of cellular clocks in a mammalian system without and with noise[45,48]. The model for the biochemical mechanism by which *N. crassa* synchronizes the clocks in different cells is also a quorum sensing model[133] (**Fig. 3.1**). The mean field assumption about the action of the quorum sensing signal[48] is supported experimentally with data from a "big chamber" microfluidic device – the signal diffuses uniformly and instantaneously within the device[133]. In the quorum sensing component of the model (in grey in **Fig. 3.1**) the signal is taken as Tyrosol[92] and the quorum sensing regulator as the protein encoded by NCU03643[135] in the grey region controlling fermentation (**Fig. 3.1**). The immediate phenotype of quorum is Ethanol consumption or production at low and high density, respectively. The transcription factor NCU03643 is under the control of the *qa* gene cluster[135]. The transcription factor encoded by NCU03643 or QA-1F

regulates a putative alcohol dehydrogenase (NCU03415) in *N. crassa*[135], which potentially connects NCU03643 to the ethanol switch.

The model also explicitly incorporates the genetic network of the *qa* gene cluster because the *qa-x* mutant is more sensitive to density than Wildtype (WT)[141] and because the hypothesized quorum sensing regulation is directly or indirectly (through NCU03643) under the control of the *qa* gene cluster[135] through its linkage to aromatic amino acid metabolism. One of the components in this metabolic network includes the *qa* cluster genes and their corresponding mRNA and protein products in blue (**Fig. 3.1**). A genetic network for the *qa* cluster has been developed previously[72,135]

The *qa* gene cluster is strongly linked to aromatic amino acid metabolism in orange (**Fig. 3.1**). For example, the QA-2 enzyme converting Dehydroquinate (DHQ) to Dehydroshikimate (DHS) can functionally substitute for that of AROM-9 in aromatic amino acid biosynthesis[142]. So, aromatic amino acid biosynthesis and degradation are included in this metabolic component of the model (**Fig. 3.1**). All of the other products have a known function except the protein QA-X. There is only one unknown step in the pathway after HGA, and the associated enzymatic role is assigned to QA-X in the model (**Fig. 3.1**).

In that fermentation provides the phenotype in quorum sensing[141] and in that QA metabolism is linked to glycolysis, fermentation, and the TCA cycle[135], the TCA cycle (in green) and Glycolysis (in orange) are included as well (**Fig. 3.1).** The *in vivo* CIVM NMR method provides the metabolic profiles in this network[94]. Northerns provide mRNA profiles on the

products of the *qa* gene cluster[72]. The metabolic components of the model are specified by CIVM-NMR measurements[94] and the pathways, derived from BIOCYC[143].

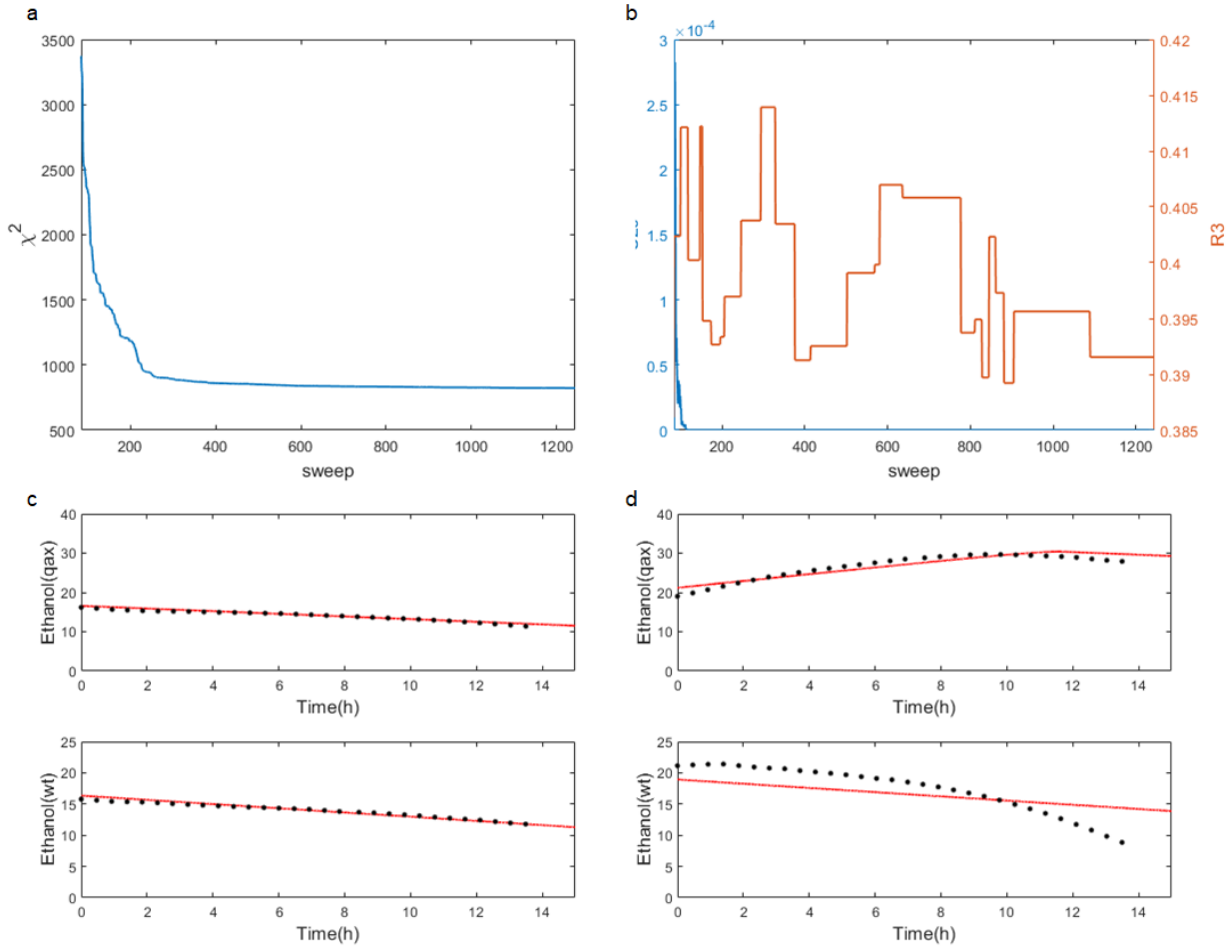


**Fig. 3.2** The Monte Carlo Experiment to fit the quorum sensing model to 1128 mRNA and metabolite measurements appears well equilibrated. (a) $\chi^2$ vs. sweep (*i.e.*, a visit once on average to each parameter in the model) with the first 80 sweeps removed to show equilibration; (b) plot of Tyrosol signal production rate (C29) and Ethanol production rate ((R3) vs. sweep as a control on equilibration of Monte Carlo Experiment) . (c) Observed and predicted trajectories of Ethanol at low density in *qa-x* and WT. (d) Observed and predicted trajectories of Ethanol at high density in *qa-x* and WT. Dots indicate CIVM NMR data; solid lines indicated expected

trajectories of Ethanol. **The plots were created in MATLAB_R2020B (**https://www.mathworks.com/products/matlab.html).

Alternative models are diagrammed is supplementary Fig. S3.1-S3.3.

## Results

**A quorum sensing model with Tyrosol as the quorum sensing signal was successfully fitted to both RNA profiling and *in vivo* metabolomic data on the clock.**

In order to determine whether or not the quorum sensing model is supported, the model was fitted to both RNA profiling[72] data and CIVM NMR data[141] on the clock on the macroscopic scale[133] using ensemble methods[72] **(Fig. 3.2**).

The RNA profiling data were acquired by Northerns– the result was 8 time points on each of the mRNAs of 6 *qa* cluster genes for WT. The real time metabolic data was acquired by CIVM-NMR on 6 metabolites, yielding 30 time points on annotated metabolites in 2 distinct genotypic backgrounds (WT, *qa-x*) each at both high and low density for a total of 1128 data points in four independent experiments.

The entire genetic network was fitted by ensemble methods[72,144] using the same rate constants for all four experiments simultaneously at low and high density in a *qa-x* mutant and wildtype (WT) background. The challenge of fitting genetic networks to omics data is having limited data, but many parameters in the network[117]. To overcome this problem the solution proposed by Boltzmann was NOT to fit one model[78], but to identify an ensemble of models consistent with available data[80]. Averaging over the fitted models in the ensemble is used to

make predictions about system dynamics (**Fig. 3.2c-d**)). This approach was first introduced into systems biology in the context of the *qa* cluster and later on the clock in *N. crassa*[72,144].

A Monte Carlo Experiment was carried out to fit the genetic network in **Fig. 3.1** by ensemble methods[144] to the data on four experiments involving WT and *qa-x* at high and low density (**Fig. 3.2c-d**) (see Materials and Methods). The ensemble is well equilibrated after 300 sweeps (*i.e.*, the number of Monte Carlo steps taken to visit on average each parameter once), in which the chi-squared statistic drops to 844.38 or 844.38/1128 = 0.7486 chi-squared per data point, much better than in previous clock models[117,144] (**Fig. 3.2a**). One common set of rate coefficients (**Table S31.1**) were successfully fitted to all four experiments in a *qa-x* and WT background at high and low density. Only initial conditions varied between experiments. Key parameters, such as the rate of production of the Tyrosol signal (C29) and the rates of production of Ethanol (R3) of the cell (**Fig. 3.2b**) appear well equilibrated. The model well predicted the Ethanol switch at low and high densities with Ethanol consumption predicted at low density and ethanol consumption predicted at high density. The Ethanol concentration showed the metabolic switch at low and high densities in both model and experiment (**Fig. 3.2c-d**). There is a striking difference in the production response at high density in *qa-x* and WT - in *qa-x* production of Ethanol is sustained over 10 hours and in WT production of Ethanol is sustained only over 1 hour (**Fig. 3.4D**).

**The quorum sensing model fitted to available data displays an Ethanol metabolic switch, a switch on in the quorum sensing regulator from low to high density and the accumulation of HGA in the *qa-x* mutant.**

There are several results that must be accommodated by the model to fit the available data: (1) the CIVM data displaying a metabolic switch from Ethanol consumption to Ethanol production from low to high density; (2) the quorum sensing regulator (*e.g.*, Tyrosol) turning on at high density to power the metabolic switch (**Fig. S3.4**); (3) a *qa-x* mutant displaying an accumulation of HGA to generate the rise in aromatic amino acids and aromatic alcohols.

The model displays all of these behaviors as well as an excellent fit to the measured RNA profiles (**Fig.3**) and metabolic trajectories (**Fig. 3.4**) – measured dynamics are well predicted by the model (**Fig. 3.1**). Most of the data points fall within two standard errors of the fitted trajectories.

The RNA profiling has the *qa* cluster mRNAs tracking the observed profiles of the 6 *qa* cluster genes as found in previous work[72,135]. Their tends to be a maximum in expression between 2-4 h after shift from sucrose to QA media in both model and experiment. This portion of the genetic network provides control not only of carbon metabolism but also the production of the hypothesized quorum sensing regulator under QA control (NCU03643).

The model also has a metabolic component derived from BIOCYC[143]. The carbon source (QA) is being consumed (**Fig. 3.4b**) at low density. Ethanol is also being consumed at low density as well. Tyrosine and phenylalanine are at low levels (**Fig. 3.4d-e**) initially.

At high density the system switched its behavior by producing Ethanol (**Fig. 3.5c**) in contrast to **Fig 3.4c**. There was also an increase in the two aromatic amino acids (**Fig. 3.5 e-f**) that was indicative of what may be happening to the hypothesized quorum sensing signals, the aromatic alcohols, that were below signal detection by CIVM-NMR. Downstream of tyrosine degradation is also seen the accumulation of Homogentisic acid (HGA) due to the probable block by *qa-x* (**Fig. 3.1**), although the metabolic trajectory of HGA predicted is a little off in its trend from that observed. The model is both qualitatively and quantitatively consistent with **Fig. 3.1** being the quorum sensing mechanism for clock phase synchronization.

a

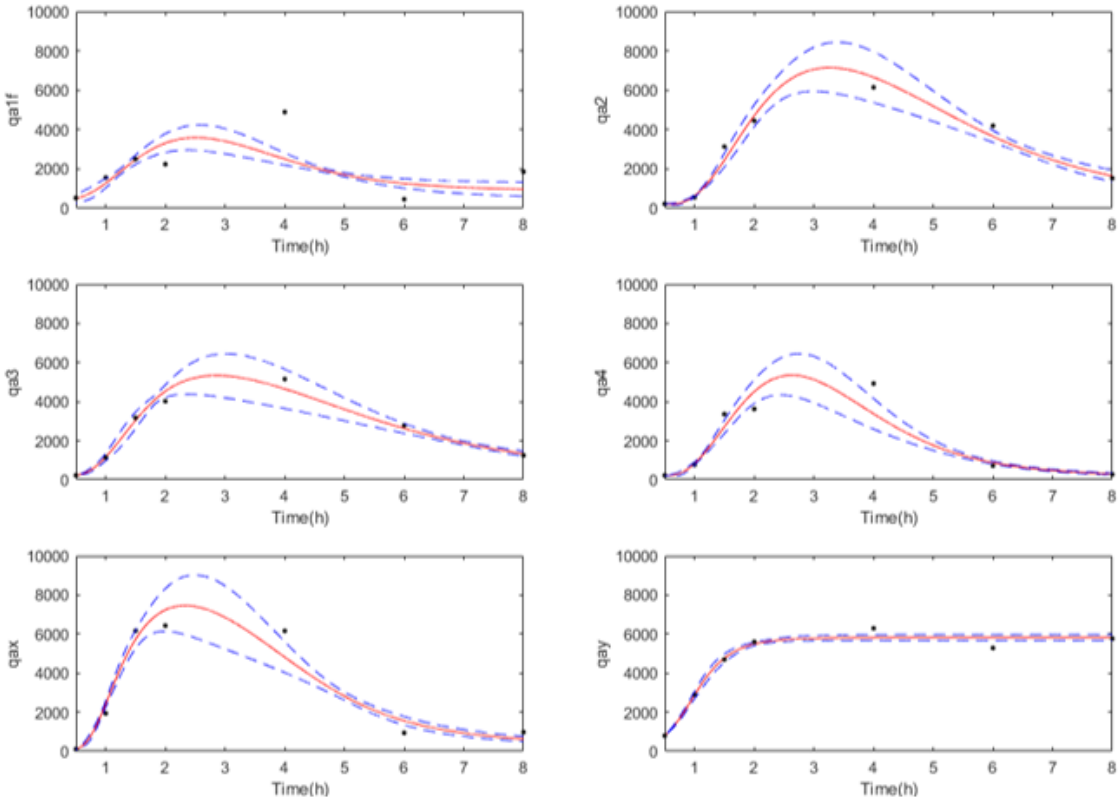

b

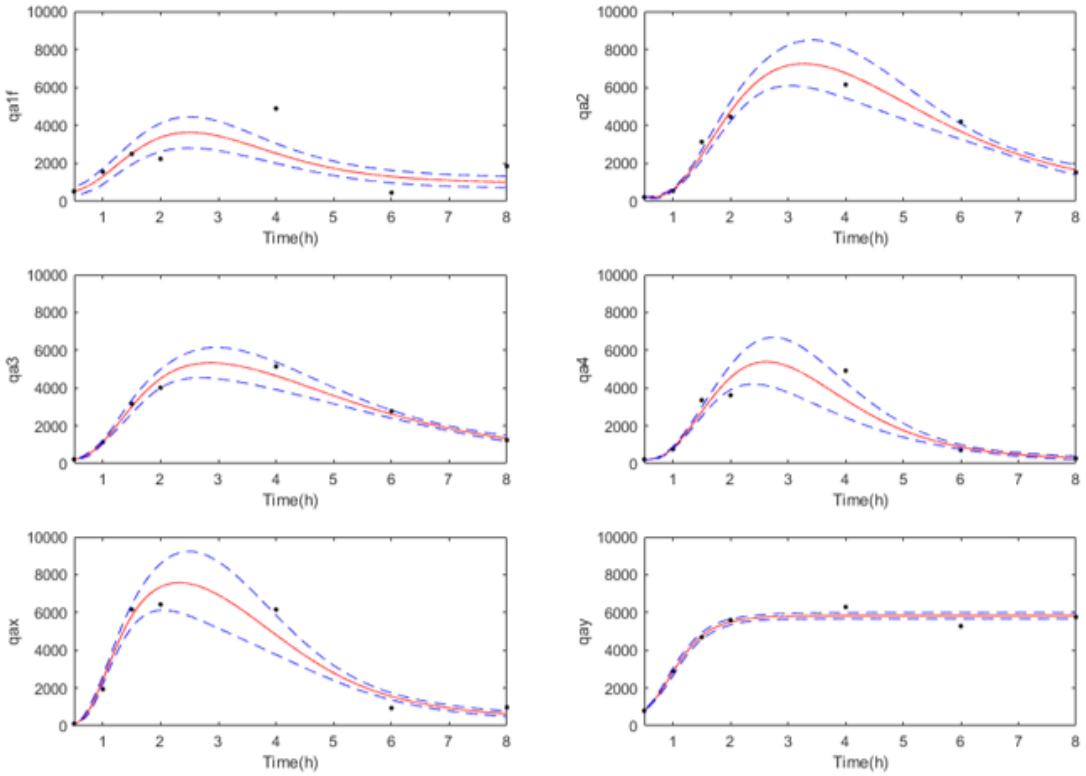


**Fig. 3.3** The RNA profiles of the *qa* gene cluster are well fitted by the quorum sensing model for all for experiments on the *qa-x* mutant at low (a) and high density (b). Northern RNA profile of: (i) *qa-1F* encoding a transcription factor ; ii) *qa-2* encoding a quinate dehydrogenase ; (iii) *qa-3* quinate dehydroquinase ; (iv) *qa-4* encoding a 3-dehydroshikimate dehydratase; (v) *qa-y* encoding a QA permease; (vi) *qa-x*. The dash-dotted (-.-.-) lines indicated 95% confidence intervals about the fitted trajectories. **The plots were created in MATLAB_R2020B (**https://www.mathworks.com/products/matlab.html).

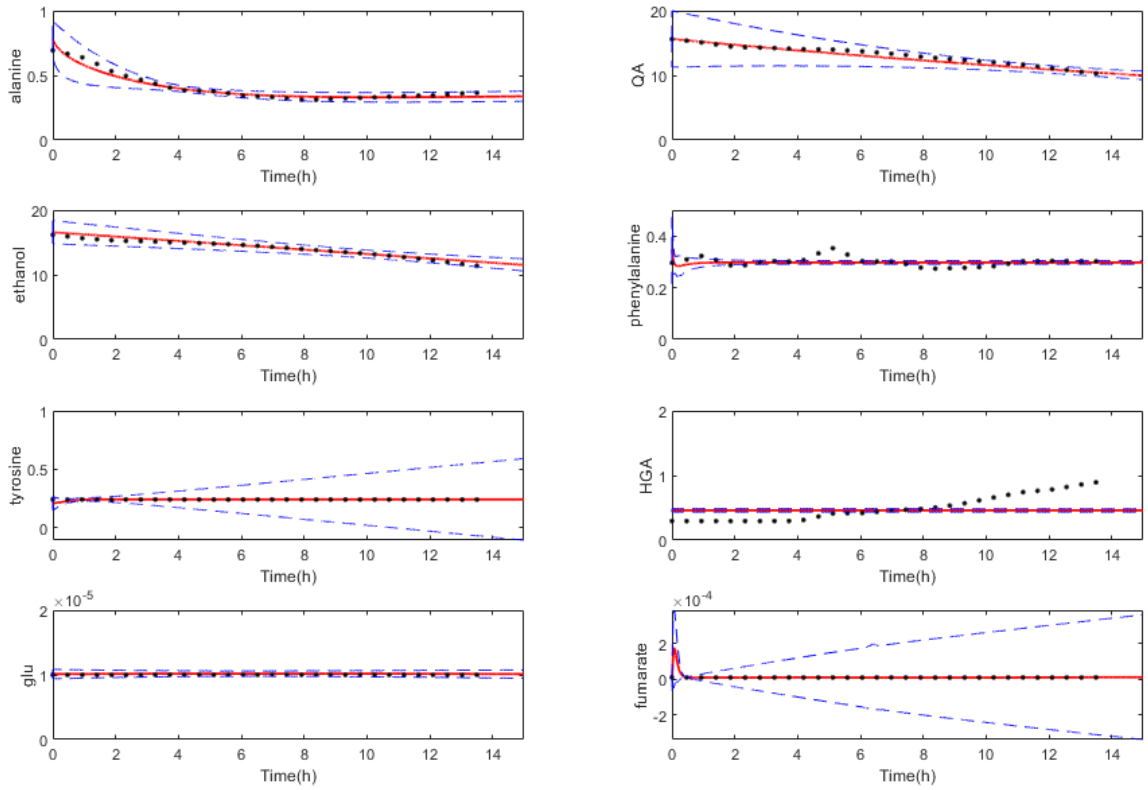


**Fig. 3.4**. The observed metabolic profiles by CIVM-NMR (dotted lines) for 8 metabolites in a *qa-x* mutant at low density are well fitted by the quorum sensing model (solid lines) (null hypothesis) in **Fig. 3.1** for: (a) alanine; ( b) QA; (c) Ethanol; (d) phenylalanine; e) tyrosine; (f) Homogentisic Acid (HGA); (g) glutamate; (h) fumarate. Model trajectories are an ensemble average. **The plots were created in MATLAB_R2020B (**https://www.mathworks.com/products/matlab.html).

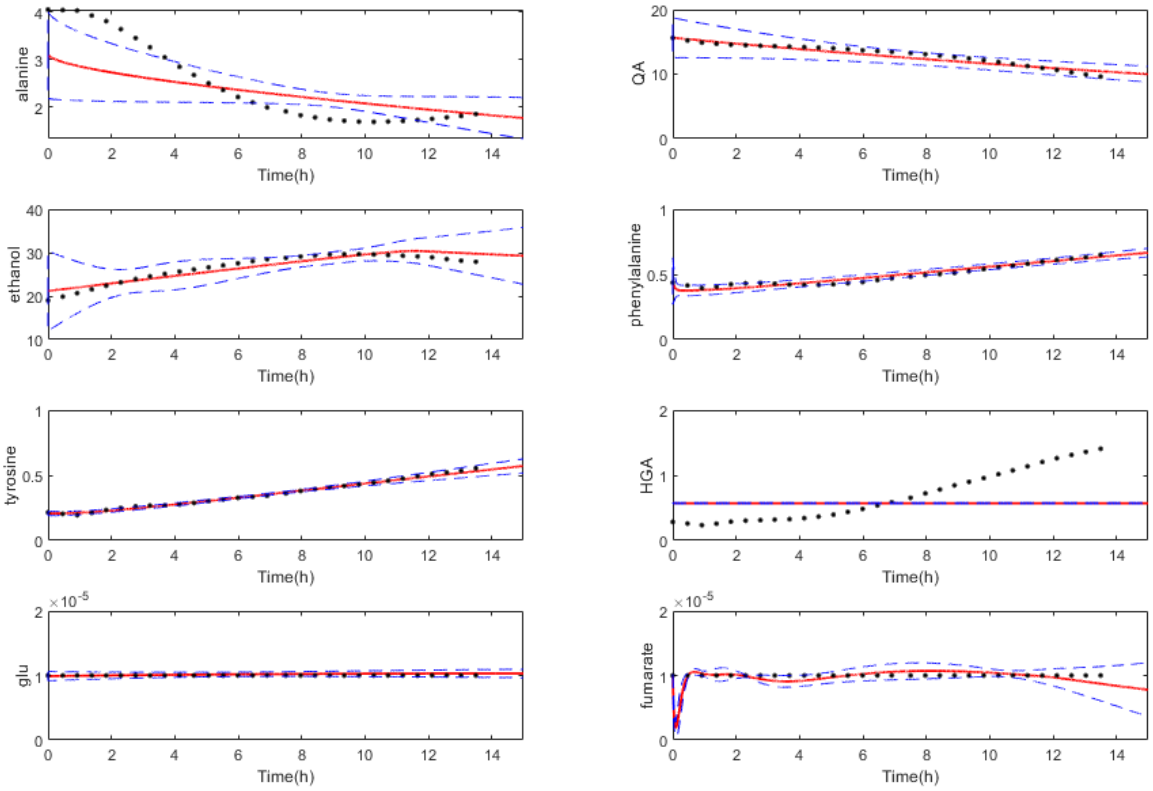


**Fig. 3.5.** The observed metabolic profiles from CIVM-NMR (dotted lines) for 8 metabolites in a *qa-x* mutant at high density are well fitted by the quorum sensing model (solid lines) (null hypothesis) in **Fig. 3.1** for: (a) alanine; ( b) QA; (c) Ethanol; (d) phenyalanine; e) tyrosine; (f) Homogentisic Acid (HGA); (g) glutamate; and (h) fumarate. The model trajectories represent ensemble means. **The plots were created in MATLAB_R2020B (**https://www.mathworks.com/products/matlab.html).

a

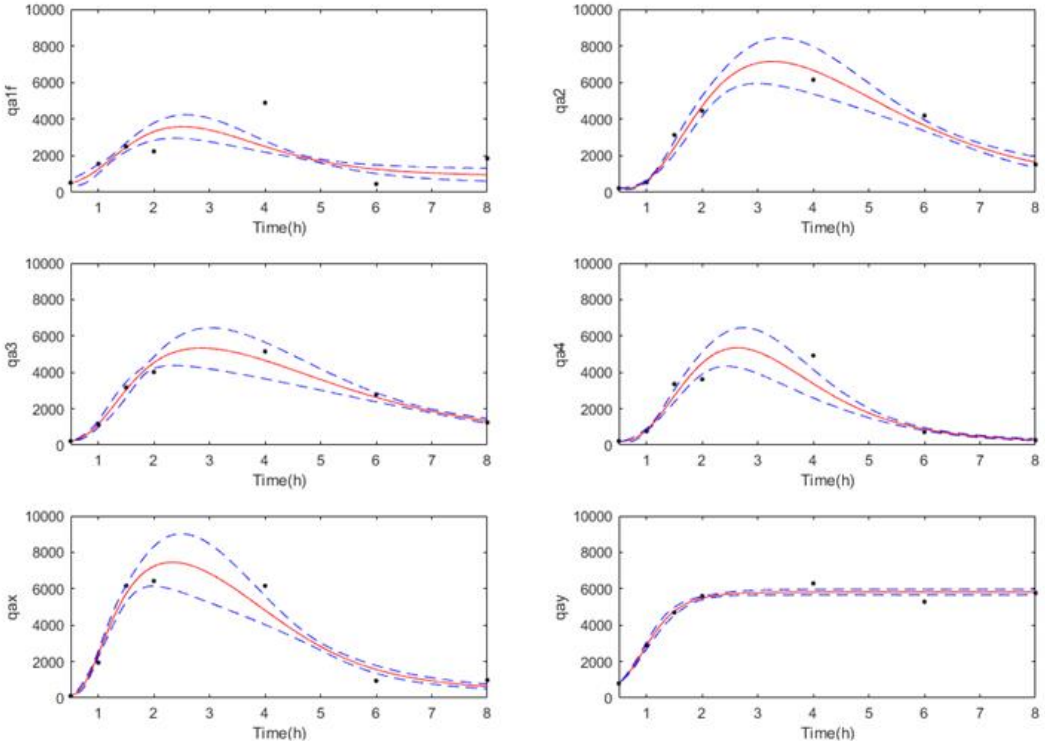


b

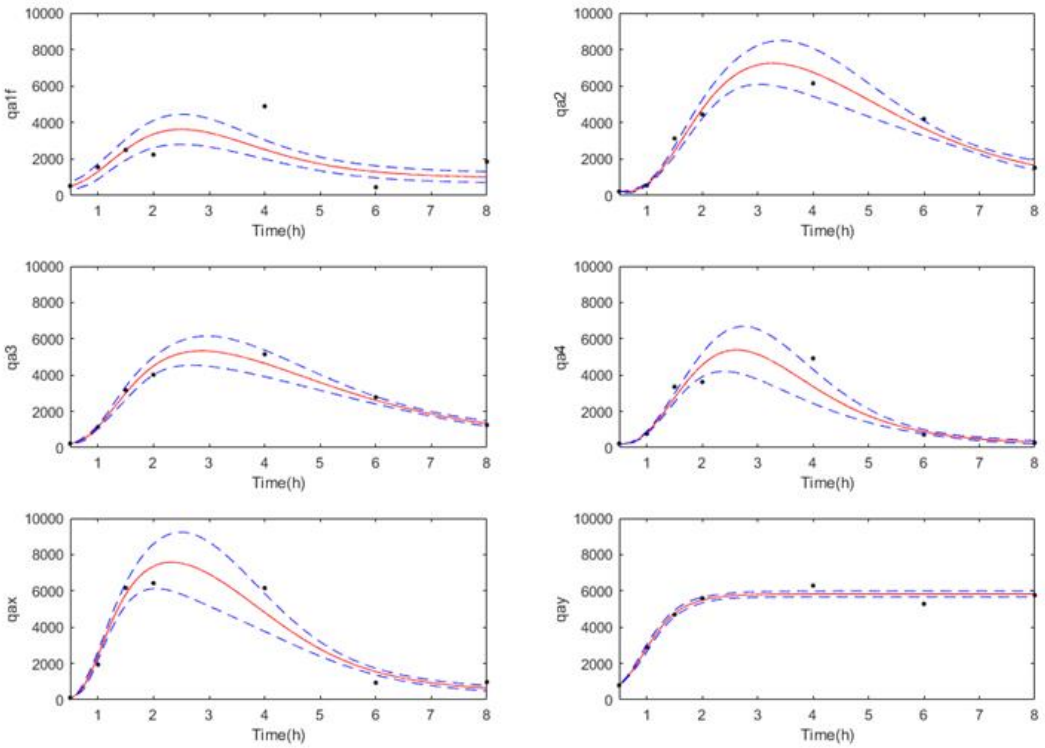

**Fig. 3.6.** The RNA profiles (dotted lines) for the *qa* cluster genes in WT are well fitted by the null hypothesis of the quorum sensing model (solid lines) by the same rate coefficients at (a) low and (b) high density as in Fig. 3.3. The fitted trajectories represent ensemble means. **The plots were created in MATLAB_R2020B (**https://www.mathworks.com/products/matlab.html).

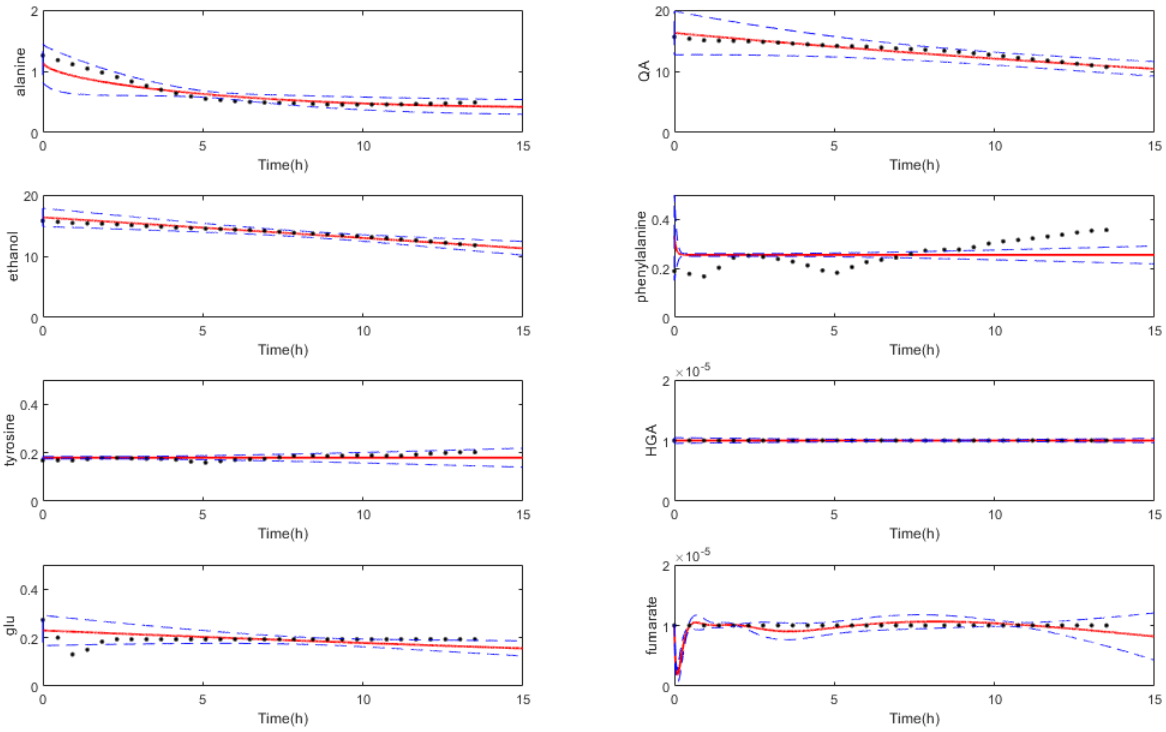


**Fig. 3.7**. The metabolic profiles from CIVM-NMR for 8 metabolites in WT at low density are well fitted by the quorum sensing model (**Fig. 3.1**). Dotted lines are the CIVM-NMR trajectories, and solid curves are fitted ensemble means of the CIVM-NMR trajectories. **The plots were created in MATLAB_R2020B (**https://www.mathworks.com/products/matlab.html).

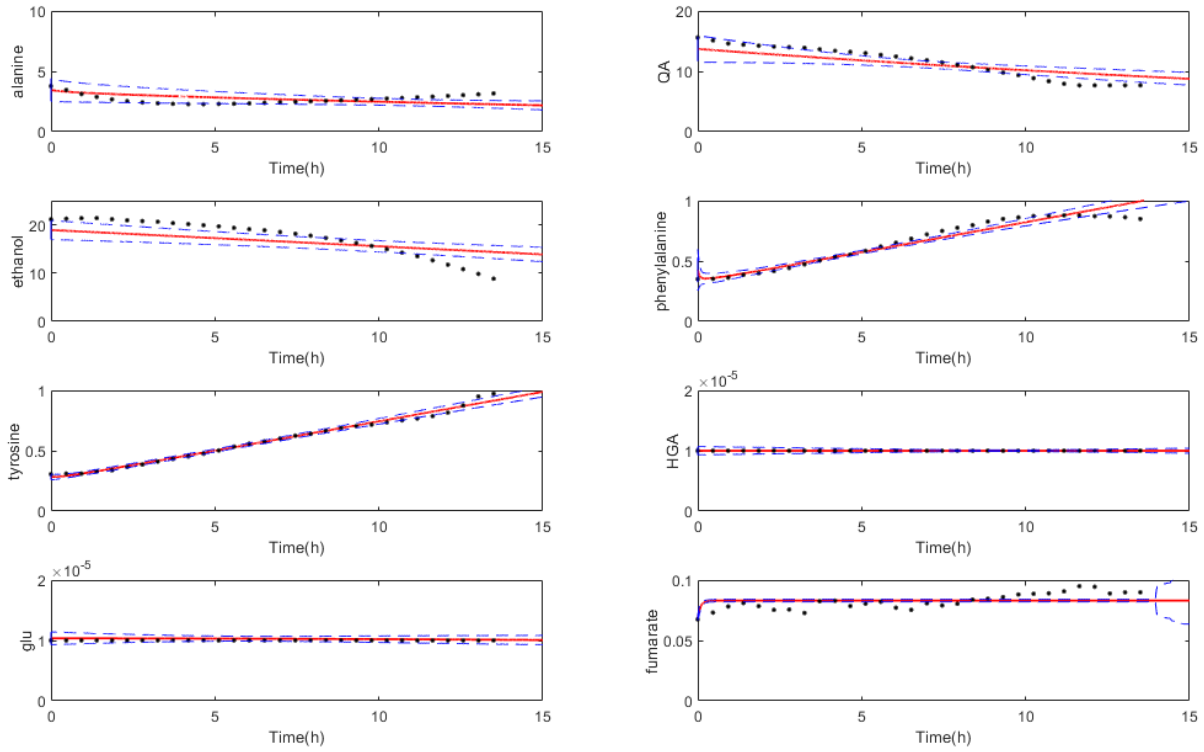


**Fig. 3.8.** The metabolic profiles from CIVM-NMR for 8 metabolites in WT at high density are well fitted by the quorum sensing model (**Fig. 3.1**). Dotted lines are the CIVM-NMR trajectories, and solid curves are fitted ensemble means of the CIVM-NMR trajectories. **The plots were created in MATLAB_R2020B (**https://www.mathworks.com/products/matlab.html).

**The quorum sensing model is less sensitive to density in WT than in *qa-x***

The behavior of the metabolism of Ethanol is quite different in WT than in a *qa-x* background (**Fig. 3.7-8***)*. At low density there is little change in Ethanol. At high density the increase is slight and is sustained for about an hour. The Ethanol switch is greatly diminished in WT. Tyrosol only appears to increase in the *qa-x* background at high density and not in WT (**Fig. S3.4**).

HGA also does not accumulate without the QA-X metabolic block present. Without the HGA block it likely there is not sufficient accumulation of the quorum sensing signal. The system is then not sensitive enough to detect the density differential.

**Testing that QA-X is a structural enzyme vs. a regulator of structural enzymes below HGA.**

The function of *qa-x* is unknown, but the block at HGA suggests that it is a particular gene encoding a metabolic step below HGA (**Fig. 3.1**)[141]. An alternative hypothesis is its only annotation as a inositol monophosphatase[145]. The RNA profiling and CIVM-NMR can be used to test one hypothesis against the other (**Fig. 3.9).**

Under the null hypothesis the *qa-x* is a structural gene HGA (**Fig. 3.1).** Under the alternative hypothesis it is a regulator. Both models were identified by ensemble methods (see Materials and Methods).

The resulting histograms of the chi-squared statistics across each ensemble associated with each hypothesis suggest that both hypotheses are consistent with the available RNA profiling data and CIVM-NMR data. Neither hypothesis can be eliminated as indicated by the overlapping chi-squared statistic histograms.

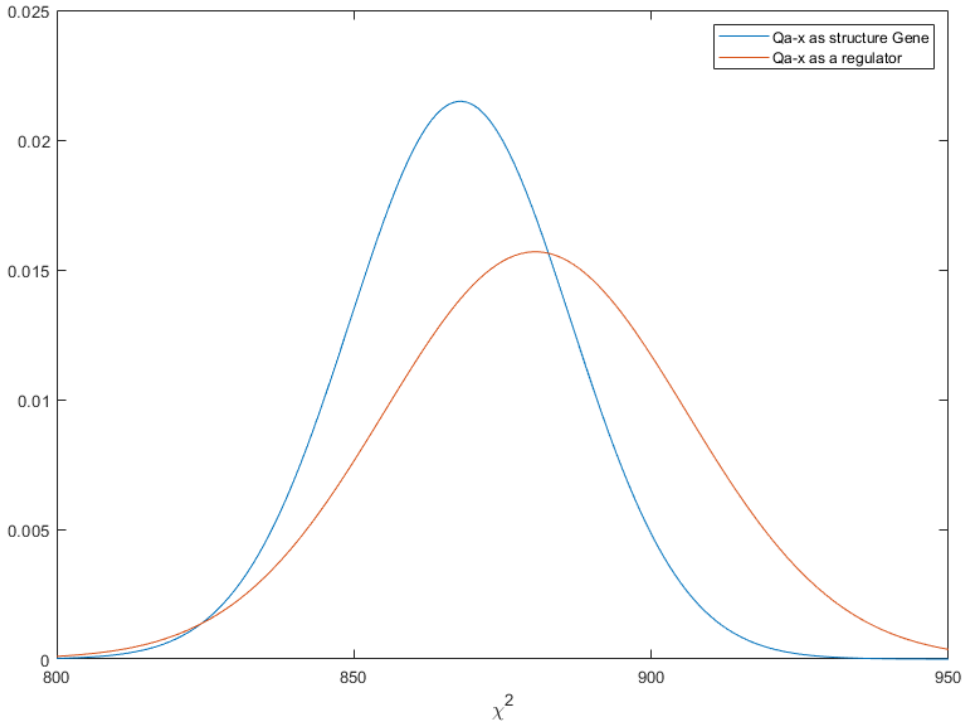


**Fig. 3.9.** The RNA profiling data and CIVM-NMR data are consistent with *qa-x* being a structural gene in QA metabolism as in **Fig. 3.1** or as an alternative regulator of QA metabolism. The two hypotheses are compared by the overlapping chi-squared distributions across two ensembles under each of these hypotheses. **The plots were created in MATLAB_R2020B (**https://www.mathworks.com/products/matlab.html).

**Testing that the quorum sensing signal is tyrosol vs. tryptophol or phenylethanol.**

In *Candida albicans* the aromatic alcohols, Tyrosol and Farnesol, are both quorum sensing signals[146]. In *S. cerevisiae* both Phenylethanol and Tryptophol are quorum sensing signals[92]. It is reasonable to test whether or not Tyrosol or the other two aromatic alcohols in **Fig. 3.1** are quorum sensing signals as the block in HGA, for example, leads to their accumulation. Each hypothesis (networks available for the alternative hypotheses in **Fig. S3.1-**

**3.3**) was fitted by the ensemble method, and chi-squared statistics on ensembles from each of the three hypotheses were constructed (**Fig. 3.1).** All three hypotheses were consistent with available RNA profiling and CIVM-NMR data from 4 experiments and overlapping (**Fig. 3.3**). Anyone of the aromatic alcohols or a combination could be the quorum sensing signal(s).

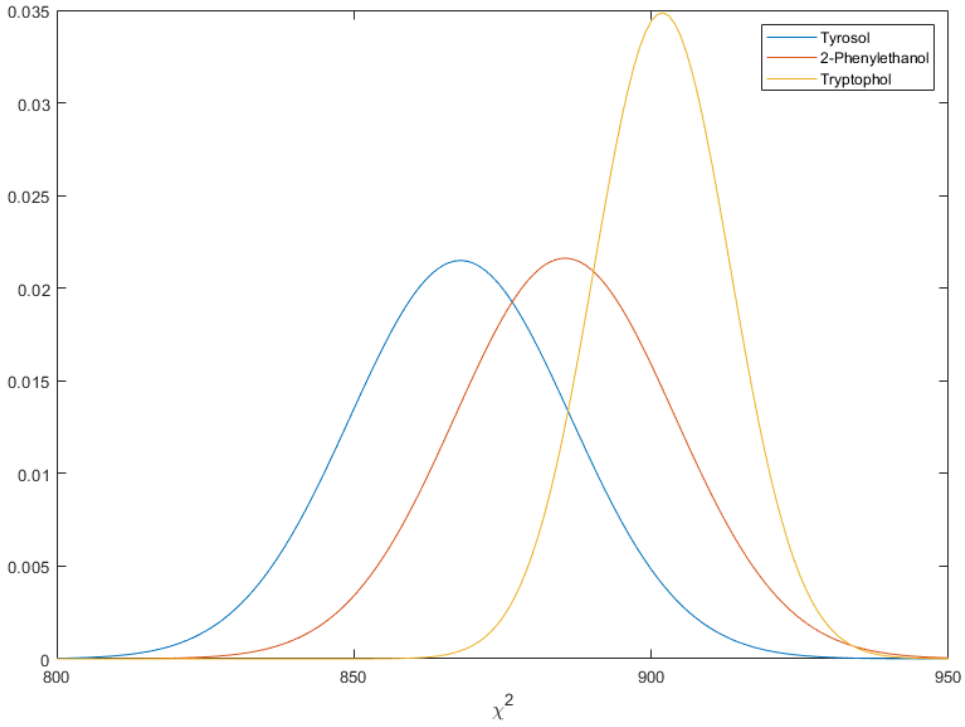


**Fig. 3.10.** There is little to distinguish among aromatic alcohols as a quorum sensing signal based on the overlapping chi-squared distributions across the ensembles for each hypothesis with the signal being: (T) Tyrosol (null hypothesis); (Tr) Tryptophol; or (P) Phenylethanol. **The plots were created in MATLAB_R2020B (**https://www.mathworks.com/products/matlab.html).

**Discussion**

In previous work we have provided evidence for a quorum sensing signal with a radius of no more than 13.05 nm for phase synchronization of the biological clock in *Neurospora crassa* using microfluidics[133]; moreover, we have shown that there is a classic density dependent response of phase synchronization of single cell oscillators that is associated with a hypothetical quorum sensing signal associated with the clock[133]. More recently by using CIVM-NMR a classic metabolic mutant *qa-x*[140] was associated with density-dependent switch in Ethanol production[141]. The hypothesis here is that these two quorum sensing mechanisms are one and the same.

Having shown quorum sensing in the phase synchronization of the clock, it is natural to ask what the biochemical mechanism is by which quorum sensing is achieved in the phase synchronization of cellular clocks to produce a clock on a macroscopic scale of tissues and the whole organism. One clue to such a biochemical mechanism comes from the application of CIVM-NMR in real time to living *N. crassa* cells.

Metabolic trajectories provide further clues to the identity of the metabolic signal. The fact that a density dependent switch in Ethanol production and consumption exists in *qa-x* background suggests what metabolites could act a quorum sensing signal.

The block in HGA generated by *qa-x* would imply an accumulation of aromatic alcohols as an indicator of growth (**Fig. 3.1**). Such a mechanism has been demonstrated in other fungi, such as *C. albicans*[146] and *S. cerevisiae*[92]. To test this hypothesis a biochemical model was

developed and fitted by ensemble methods to RNA profiling and CIVM-NMR and was self consistent with the hypothesis that Tyrosol was the quorum sensing signal. In fitting this model, only one set of rate coefficients were needed to explain all 4 experiments on *qa-x* and WT at high and low density.

There were limitations in this conclusion. The ability to distinguish a regulatory role for *qa-x* or a role as a structural gene could not be distinguished. The Monte Carlo experiments suggest the next round of experiments to isolate the QS signal. In previous work activity-guided fractionation[147] was used to isolating the mating pheromone in *Canerohabditis elegans*[148] . An assay for activity-guided fraction has been developed[141]. The assay involves using media conditioned by cells at high density to treat cells grown at low density and observing the production of Ethanol. This simple assay is to be applied repeatedly to fraction libraries to isolate the signal to confirm whether or not the quorum sensing signal is a particular aromatic alcohol or set of aromatic alcohols[92].

**Conclusion**

A detailed biochemical mechanism was developed to explain the phase synchronization of a population of cellular clocks by quorum sensing in *N. crassa*. The mechanism involves an aromatic alcohol as the quorum sensing signal and gene NCU03643 as the quorum sensing regulator[141]. The model is consistent with both RNA profiling data on the *qa* gene cluster linked to aromatic amino acid synthesis as well as real time CIVM-NMR data[94] on living cells of *N. crassa*. The fitted model predicts that one or more aromatic alcohols may be the quorum sensing

signal, a prediction that can be tested by activity-guided fractionation[147] using media conditioned by cells grown at high density[141]

## Materials and Methods

### Model

The full genetic network is specified in **Fig. 3.1**, and a script specifies the detailed system of ODEs (supplement S1) in MATLAB_R2020B **(**https://www.mathworks.com/products/matlab.html).

### Quantification of RNA profiles and Metabolic Features

The RNA profiling data were acquired by Northerns using RNA isolated by shifting liquid cultures from 1.5% sucrose to 0.3% quinic acid in Fries media[72] – the result was 8 time points on each of the mRNAs of 6 *qa* cluster genes. The same RNA profile is used for both the *qa-x* and WT background with the exception of *qa-x* itself.

Time-series metabolism was recorded by CIVM-NMR[94] and extracted by RTExtract[149]. Compound annotation followed the original CIVM-NMR publication, and ridges were selected for quantification[94]. The absolute quantification was computed though quinic acid concentration at the start time point and based on extracted ridge intensities. More details on data processing and feature extraction can be found here[150]. The real time metabolic data was acquired by CIVM-NMR on 6 metabolites, yielding 30 time points on annotated metabolites in 2 distinct genotypic backgrounds (WT, *qa-x*) each at both high and low density for a total of 1128 data points in four independent experiments.

**Calculating phase**

To calculate the phase for a fluorescent series x(t), first the Hilbert transform $\tilde{x}(t) = PV\ \frac{1}{\pi}\int_{-\infty}^{\infty}\frac{x(\tau)}{t-\tau}d\tau$ was computed from the Fast Fourier Transform[102] of x(t). The Hilbert phase $F^H(t)$ is defined as the phase angle between the Hilbert Transform $\tilde{x}(t)$ and x(t) by $F^H(t) = tan^{-1}\left(\frac{\tilde{x}(t)}{x(t)}\right)$ to avoid discontinuities in the phase angle at $\pi$ and -$\pi$, the Hilbert phase was continuized to $F^C(t)$. The continuization was done recursively through the relation: $F^C(t+1) = F^C(t) + m^C(t)2\pi$, where at each step the argument m was chosen to minimize: $Df_m = |F^H(t+1) - F^C(t) + 2\pi m|$. With the continuized Hilbert Phase $F^C(t)$, the phase is defined by: $M^C = \frac{|F^C(t_1) - F^C(t_0)|}{2\pi}$ in units of cycles. An accessible description of these phase measures and code to calculate them in MATLAB are available[62] with associated MATLAB in GitHub.

**Ensemble Methods**

The quorum sensing and cell-to-cell contact models specifying the ODEs in (1)-(23) were identified using a Metropolis-Hastings updating scheme[65]. Proposed solutions during the Markov Chain Monte Carlo (MCMC) were with an Adaptive Runge-Kutta solver. The equilibration stage involved 300 sweeps. The accumulation phase involved 300 sweeps.

The data sets generated during the current study are available from the corresponding authors on reasonable request.

# CHAPTER 5

# CONCLUSION

As a summary, by applying a method that combines numerical simulations with controlled laboratory experiments, we have addressed the previous three questions that are raised in the introduction.

First, to have a better understanding of how single cells communicate to overcome their stochasticity and synchronize their circadian rhythm with each other, a “big chamber” microfluidic experiment as well as a microfluidic experiment were designed to demonstrate that communication existed among cells. At the macroscopic limit (~150,000 cell), there was a high degree of phase synchronization between cells in the artificial tissue. In the microwell experiment, the ability to isolate single cells in individual wells showing phase synchronization provided strong evidence for the quorum sensing hypothesis and some information about the communication parameters that quantitate quorum sensing. Using the microwell devices, the collective behavior of synchronization was shown to be density-dependent and hence a quorum sensing behavior. While conidial cells are relatively easy to manipulate, a remaining challenge is the study and manipulation of the filamentous stage in the fungal syncytium with microfluidic devices[95-98]. It is very likely that by considering other life stages in the fungal syncytium, other mechanisms of cellular communication will be uncovered and found to be involved in the phase transition to synchronization of cellular oscillators.

In addition, to fill the knowledge gap of how growing cells communicate and synchronize their circadian rhythm with each other, a microfluidic chip with serpentine channels was fabricated to demonstrate the existence of cellular clocks in individual hyphae, the dominant life stage of filamentous fungi. Hyphae within the device are also phase synchronized with respect to their individual hyphal clocks. Since there is a possibility that clock communication may occur thorough phase, a new microfluidic device needs to be fabricated to allow hyphae that are entrained at different phases to synchronize with each other.

Finally, to answer the questions that what the signaling molecule is that single cells use to communicate with each other and how the signaling molecule affect the clock, a detailed biochemical mechanism was developed to explain the phase synchronization of a population of cellular clocks by quorum sensing. The mechanism involves an aromatic alcohol as the quorum sensing signal and gene NCU03643 as the quorum sensing regulator[141]. The model is consistent with both RNA profiling data on the qa gene cluster linked to aromatic amino acid synthesis as well as real time CIVM-NMR data[94] on living cells of N. crassa. The fitted model predicts that one or more aromatic alcohols may be the quorum sensing signal, a prediction that can be tested by activity-guided[147] fractionation using media condition by cells grown at high density[141].

## REFERENCE


1 Caranica, C., Al-Omari, A., Schuttler, H.-B. & Arnold, J. Identifying a clock stochastic network with light entrainment for single cells of *Neurospora crassa* by ensemble methods. *Nature Scientific Reports* **19**, 15168 (2020).

2 Dong, W. *et al.* Systems biology of the clock in Neurospora crassa. *PloS one* **3**, e3105 (2008).

3 Castro-Longoria, E., Ferry, M., Bartnicki-Garcia, S., Hasty, J. & Brody, S. Circadian rhythms in *Neurospora crassa*: Dynamics of the clock component *frequency* visualized using a fluorescent reporter. *Fungal Genetics and Biology* **47**, 332-341 (2010).

4 Gooch, V. D. *et al.* Fully codon-optimized luciferase uncovers novel temperature characteristics of the Neurospora clock. *Eukaryotic cell* **7**, 28-37 (2008).

5 Conrad, J. C. J. P. o. t. N. A. o. S. Quantifying collective behavior in mammalian cells. **109**, 7591-7592 (2012).

6 Dunlap, J. C. Molecular bases for circadian clocks. *Cell* **96**, 271-290 (1999).

7 Al-Omari, A. *et al.* Discovering Regulators in Post-Transcriptional Control of the Biological Clock of $ Neurospora~ crassa $ Using Variable Topology Ensemble Methods on GPUs. *IEEE access* **6**, 54582-54594 (2018).

8 Dong, W. *et al.* Systems biology of the clock in Neurospora crassa. *PloS one* **3**, e3105 (2008).

9 Maung, S. C., El Sara, A., Chapman, C., Cohen, D. & Cukor, D. Sleep disorders and chronic kidney disease. *World journal of nephrology* **5**, 224 (2016).

10 Nakano, S. *et al.* Circadian rhythm of blood pressure in normotensive NIDDM subjects: its relationship to microvascular complications. *Diabetes Care* **14**, 707-711 (1991).

11 Gorbacheva, V. Y. *et al.* Circadian sensitivity to the chemotherapeutic agent cyclophosphamide depends on the functional status of the CLOCK/BMAL1 transactivation complex. *Proceedings of the National Academy of Sciences* **102**, 3407-3412 (2005).

12 Larrondo, L. F., Olivares-Yañez, C., Baker, C. L., Loros, J. J. & Dunlap, J. C. Decoupling circadian clock protein turnover from circadian period determination. *Science* **347**, 1257277 (2015).

13 Duvall, L. B. & Taghert, P. H. The Circadian Neuropeptide PDF Signals Preferentially through a Specific Adenylate Cyclase Isoform AC3 in M Pacemakers of Drosophila. *Plos Biology* **10**, doi:ARTN e100133710.1371/journal.pbio.1001337 (2012).

14 Abraham, U. *et al.* Coupling governs entrainment range of circadian clocks. *Molecular systems biology* **6**, 438 (2010).

15 Carr, A.-J. F. & Whitmore, D. Imaging of single light-responsive clock cells reveals fluctuating free-running periods. *Nature cell biology* **7**, 319 (2005).

16 Muranaka, T. & Oyama, T. Heterogeneity of cellular circadian clocks in intact plants and its correction under light-dark cycles. *Science advances* **2**, e1600500 (2016).

17 Deng, Z. *et al.* Synchronizing stochastic circadian oscillators in single cells of *Neurospora crassa*. *Scientific Reports* **6**, 35828 (2016).

18 Deng, Z. *et al.* Single Cells of Neurospora Crassa Show Circadian Oscillations, Light Entrainment, Temperature Compensation, and Phase Synchronization. *IEEE Access* **7**, 49403-49417 (2019).
19 Benzi, R., Sutera, A. & Vulpiani, A. The mechanism of stochastic resonance. *Journal of Physics A: Mathematical and General* **14**, L453 (1981).
20 Caranica, C. *et al.* Ensemble methods for stochastic networks with special reference to the biological clock of Neurospora crassa. *PloS one* **13**, e0196435 (2018).
21 Smith, S. & Grima, R. Single-cell variability in multicellular organisms. *Nature Communications* **9**, 345, doi:10.1038/s41467-017-02710-x (2018).
22 Nakashima, H. A Liquid Culture Method for the Biochemical Analysis of the Circadian Clock of Neurospora crassa. *Plant and Cell Physiology* **22**, 231-238, doi:10.1093/oxfordjournals.pcp.a076160 (1981).
23 Connor, M. R. & Atsumi, S. Synthetic biology guides biofuel production. *BioMed Research International* **2010** (2010).
24 Sforza, E., Simionato, D., Giacometti, G. M., Bertucco, A. & Morosinotto, T. Adjusted light and dark cycles can optimize photosynthetic efficiency in algae growing in photobioreactors. *PloS one* **7**, e38975 (2012).
25 Buhl, J. *et al.* From disorder to order in marching locusts. *Science* **312**, 1402-1406 (2006).
26 Weber, W. *et al.* A synthetic time-delay circuit in mammalian cells and mice. *Proceedings of the National Academy of Sciences* **104**, 2643-2648 (2007).
27 Cheong, J. H. *et al.* The macroscopic limit to synchronization of cellular clocks in single cells of Neurospora crassa. *Nature Scientific Reports* **in press** (2022).
28 Winfree, A. T. On emerging coherence. *Science* **298**, 2336-2337 (2002).
29 Platt, J. R. Strong Inference. *Science* **146**, 347-353 (1964).
30 Erez, Z. *et al.* Communication between viruses guides lysis–lysogeny decisions. *Nature* **541**, 488, doi:10.1038/nature21049 https://www.nature.com/articles/nature21049#supplementary-information (2017).
31 Deng, Z. *et al.* Single cells of *Neurospora crassa* show circadian oscillations as well light entrainment and temperature compensation. *IEEE Access* **7**, 49403-49417 (2019).
32 Ballerini, M. *et al.* Interaction ruling animal collective behavior depends on topological rather than metric distance: Evidence from a field study. *Proceedings of the National Academy of Sciences* **105**, 1232, doi:10.1073/pnas.0711437105 (2008).
33 Rosenthal, S. B., Twomey, C. R., Hartnett, A. T., Wu, H. S. & Couzin, I. D. Revealing the hidden networks of interaction in mobile animal groups allows prediction of complex behavioral contagion. *Proceedings of the National Academy of Sciences* **112**, 4690, doi:10.1073/pnas.1420068112 (2015).
34 Torney, C. J., Hopcraft, J. G. C., Morrison, T. A., Couzin, I. D. & Levin, S. A. From single steps to mass migration: the problem of scale in the movement ecology of the Serengeti wildebeest. *Philosophical Transactions of the Royal Society B: Biological Sciences* **373**, 20170012, doi:doi:10.1098/rstb.2017.0012 (2018).
35 Strandburg-Peshkin, A., Farine, D. R., Couzin, I. D. & Crofoot, M. C. Shared decision-making drives collective movement in wild baboons. *Science* **348**, 1358-1361 (2015).
36 Chen, Y., Kim, J. K., Hirning, A. J., Josić, K. & Bennett, M. R. Emergent genetic oscillations in a synthetic microbial consortium. *Science* **349**, 986, doi:10.1126/science.aaa3794 (2015).

37 Sumpter, D. J. T. The principles of collective animal behaviour. *Philosophical Transactions of the Royal Society B: Biological Sciences* **361**, 5 (2006).
38 Wacquier, B., Voorsluijs, V., Combettes, L. & Dupont, G. Coding and decoding of oscillatory Ca2+ signals. *Seminars in Cell & Developmental Biology* **94**, 11-19, doi:https://doi.org/10.1016/j.semcdb.2019.01.008 (2019).
39 Voorsluijs, V., Dawson, S. P., De Decker, Y. & Dupont, G. Deterministic Limit of Intracellular Calcium Spikes. *Physical Review Letters* **122**, 088101, doi:10.1103/PhysRevLett.122.088101 (2019).
40 Sgro, A. E. *et al.* From intracellular signaling to population oscillations: bridging size- and time-scales in collective behavior. *Molecular Systems Biology* **11**, 779, doi:https://doi.org/10.15252/msb.20145352 (2015).
41 Miller, M. B. & Bassler, B. L. Quorum Sensing in Bacteria. *Annual Review of Microbiology* **55**, 165-199, doi:10.1146/annurev.micro.55.1.165 (2001).
42 Whiteley, M., Diggle, S. P. & Greenberg, E. P. Progress in and promise of bacterial quorum sensing research. *Nature* **551**, 313, doi:10.1038/nature24624 (2017).
43 Mehmood, A. *et al.* Fungal Quorum-Sensing Molecules and Inhibitors with Potential Antifungal Activity: A Review. *Molecules* **24**, 1950, doi:10.3390/molecules24101950 (2019).
44 Nudleman, E., Wall, D. & Kaiser, D. Cell-to-cell transfer of bacterial outer membrane lipoproteins. *Science* **309**, 125-127 (2005).
45 Ullner, E., Buceta, J., Díez-Noguera, A. & García-Ojalvo, J. Noise-induced coherence in multicellular circadian clocks. *Biophysical Journal* **96**, 3573-3581 (2009).
46 Strogatz, S. H. From Kuramoto to Crawford: exploring the onset of synchronization in populations of coupled oscillators. *Physica D: Nonlinear Phenomena* **143**, 1-20, doi:https://doi.org/10.1016/S0167-2789(00)00094-4 (2000).
47 Winfree, A. T. Biological rhythms and the behavior of populations of coupled oscillators. *Journal of Theoretical Biology* **16**, 15-42, doi:https://doi.org/10.1016/0022-5193(67)90051-3 (1967).
48 Gonze, D., Bernard, S., Waltermann, C., Kramer, A. & Herzel, H. Spontaneous Synchronization of Coupled Circadian Oscillators. *Biophysical Journal* **89**, 120-129, doi:https://doi.org/10.1529/biophysj.104.058388 (2005).
49 Ko, C. H. *et al.* Emergence of noise-induced oscillations in the central circadian pacemaker. *PLoS Biol* **8**, e1000513 (2010).
50 Gang, H., Ditzinger, T., Ning, C. Z. & Haken, H. Stochastic resonance without external periodic force. *Physical Review Letters* **71**, 807-810, doi:10.1103/PhysRevLett.71.807 (1993).
51 Rappel, W.-J. & Strogatz, S. H. Stochastic resonance in an autonomous system with a nonuniform limit cycle. *Physical Review E* **50**, 3249 (1994).
52 Zhou, T., Chen, L. & Aihara, K. Molecular Communication through Stochastic Synchronization Induced by Extracellular Fluctuations. *Physical Review Letters* **95**, 178103, doi:10.1103/PhysRevLett.95.178103 (2005).
53 Sriram, K. & Gopinathan, M. S. Stochastic resonance in circadian rhythms. *Theoretical Chemistry Accounts* **114**, 46-51, doi:10.1007/s00214-005-0642-3 (2005).
54 Caranica, C. *et al.* Ensemble methods for stochastic networks with special reference to the biological clock of *Neurospora crassa*. *PloS one* **13**, e0196435 (2018).

55 Whitesides, G. M. The origins and the future of microfluidics. *Nature* **442**, 368-373 (2006).
56 Mondragon-Palomino, O., Danino, T., Selimkhanov, J., Tsimring, L. & Hasty, J. Entrainment of a population of synthetic genetic oscillators. *Science* **333**, 1315-1319 (2011).
57 Aronson Benjamin, D., Johnson Keith, A., Loros Jennifer, J. & Dunlap Jay, C. Negative Feedback Defining a Circadian Clock: Autoregulation of the Clock Gene frequency. *Science* **263**, 1578-1584, doi:10.1126/science.8128244 (1994).
58 Crosthwaite Susan, K., Dunlap Jay, C. & Loros Jennifer, J. Neurospora wc-1 and wc-2: Transcription, Photoresponses, and the Origins of Circadian Rhythmicity. *Science* **276**, 763-769, doi:10.1126/science.276.5313.763 (1997).
59 Liu, Y., Garceau, N. Y., Loros, J. J. & Dunlap, J. C. Thermally regulated translational control of FRQ mediates aspects of temperature responses in the neurospora circadian clock. *Cell* **89**, 477-486 (1997).
60 Schafmeier, T. *et al.* Transcriptional feedback of Neurospora circadian clock gene by phosphorylation-dependent inactivation of its transcription factor. *Cell* **122**, 235-246 (2005).
61 Lindgren, K. M. Characterization of *ccg-1*, a clock-controlled gene of *Neurospora crassa*. *PhD dissertation. Dartmouth College* (1994).
62 Caranica, C. *et al.* What is phase in cellular clocks? *Yale Journal of Biology and Medicine* **92**, 169-178 (2019).
63 Deng, Z., Arsenault, S., Mao, L. & Arnold, J. Measuring synchronization of stochastic oscillators in biology. *J. of Physics Conference Series, 29th Annual Workshop, 2016, Recent Developments in Computer Simulational Studies in Condensed Matter Physics, Athens, GA, 22-26 February, 2016* **750**, 012001, doi:10.1088/1742-6596/750/1/012001(2016).
64 Homer, Christina M. *et al.* Intracellular Action of a Secreted Peptide Required for Fungal Virulence. *Cell Host & Microbe* **19**, 849-864, doi:https://doi.org/10.1016/j.chom.2016.05.001 (2016).
65 Yu, Y. *et al.* A genetic network for the clock of *Neurospora crassa*. *Proceedings of the National Academy of Sciences of the United States of America* **104**, 2809-2814 (2007).
66 Al-Omari, A., Arnold, J., Taha, T. & Schuttler, H. Solving Large Nonlinear Systems of First-Order Ordinary Differential Equations with Hierarchical Structure Using Multi-GPGPUs and an Adaptive Runge Kutta ODE Solver. *IEEE Access* **1**, 770-777 (2013).
67 Al-Omari, A. *et al.* Discovering Regulators in Post-Transcriptional Control of the Biological Clock of *Neurospora crassa* Using Variable Topology Ensemble Methods on GPUs. *IEEE Access* **6**, 54582-54594, doi:10.1109/ACCESS.2018.2871876 (2018).
68 Aronson, B. D., Johnson, K. A., Loros, J. J. & Dunlap, J. C. Negative feedback defining a circadian clock: autoregulation of the clock gene frequency. *Science* **263**, 1578-1584 (1994).
69 Crosthwaite, S. K., Dunlap, J. C. & Loros, J. J. Neurospora wc-1 and wc-2: transcription, photoresponses, and the origins of circadian rhythmicity. *Science* **276**, 763-769 (1997).
70 Bell-Pedersen, D., Dunlap, J. C. & Loros, J. J. The Neurospora circadian clock-controlled gene, *ccg-2*, is allelic to eas and encodes a fungal hydrophobin required for formation of the conidial rodlet layer. *Genes & Development* **6**, 2382-2394 (1992).

71 Al-Omari, A. *et al.* Discovering regulatory network topologies using ensemble methods on GPGPUs with special reference to the biological clock of *Neurospora crassa*. *IEEE Access* **3**, 27-42 (2015).
72 Battogtokh, D., Asch, D. K., Case, M. E., Arnold, J. & Schuttler, H. B. An ensemble method for identifying regulatory circuits with special reference to the *qa* gene cluster of *Neurospora crassa*. *Proc Natl Acad Sci U S A* **99**, 16904-16909 (2002).
73 Garcia-Ojalvo, J., Elowitz, M. B. & Strogatz, S. H. Modeling a synthetic multicellular clock: repressilators coupled by quorum sensing. *Proc Natl Acad Sci USA* **101**, 10955-10960 (2004).
74 Jaeger, J. *et al.* Dynamic control of positional information in the early Drosophila embryo. *Nature* **430**, 368-371 (2004).
75 Arnold, J., Taha, T. R. & Deligiannidis, L. GKIN: a tool for drawing genetic networks. *Network Biology* **2**, 26 (2012).
76 Kim, Jae K. Protein sequestration versus Hill-type repression in circadian clock models. *IET Systems Biology* **10**, 125-135 (2016).
77 Bier, M., Bakker, B. M. & Westerhoff, H. V. How Yeast Cells Synchronize their Glycolytic Oscillations: A Perturbation Analytic Treatment. *Biophysical Journal* **78**, 1087-1093, doi:https://doi.org/10.1016/S0006-3495(00)76667-7 (2000).
78 Guggenheim, E. A. *Boltzmann's distribution law*. (North-Holland Pub. Co.; Interscience Publishers, 1955).
79 Landau, D. P. & Binder, K. A Guide to Monte Carlo Simulations in Statistical Physics. *Cambridge University Press* (2009).
80 Landau, D. P., Binder, K., Landau, D. P. & Binder, K. Monte Carlo simulations at the periphery of physics and beyond. *A Guide to Monte Carlo Simulations in Statistical Physics; Cambridge University Press: New York, NY, USA*, 13-22 (2014).
81 Perkins, D. D., Radford, A. & Sachs, M. S. *The Neurospora Compendium : Chromosomal Loci*. (Academic, 2000).
82 Cotter, C. R., Schüttler, H.-B., Igoshin, O. A. & Shimkets, L. J. Data-driven modeling reveals cell behaviors controlling self-organization during *Myxococcus xanthus* development. *Proceedings of the National Academy of Sciences* **114**, E4592, doi:10.1073/pnas.1620981114 (2017).
83 Williams, C. J., Anderson, W. W. & Arnold, J. Generalized linear modeling methods for selection component experiments. *Theoretical Population Biology* **37**, 389-423, doi:https://doi.org/10.1016/0040-5809(90)90045-W (1990).
84 Roca, M. G., Arlt, J., Jeffree, C. E. & Read, N. D. Cell biology of conidial anastomosis tubes in Neurospora crassa. *Eukaryotic cell* **4**, 911-919, doi:10.1128/EC.4.5.911-919.2005 (2005).
85 De Monte, S., Ovidio, F., Danø, S. & Sørensen, P. G. Dynamical quorum sensing: Population density encoded in cellular dynamics. *Proceedings of the National Academy of Sciences* **104**, 18377, doi:10.1073/pnas.0706089104 (2007).
86 Lehmann, E. L. *Nonparametrics: Statistical Methods Based on Ranks*. *Holden-Day: San Francisco*, p. 300 (1975).
87 Shinomoto, S. & Kuramoto, Y. Phase Transitions in Active Rotator Systems. *Progress of Theoretical Physics* **75**, 1105-1110, doi:10.1143/PTP.75.1105 (1986).
88 Roberts, A. Modify the Improved Euler scheme to integrate stochastic differential equations. *arXiv: Numerical Analysis* (2012).

89 Yang, Q., Pando, B. F., Dong, G., Golden, S. S. & van Oudenaarden, A. Circadian gating of the cell cycle revealed in single cyanobacterial cells. *Science* **327**, 1522-1526 (2010).
90 Paijmans, J., Bosman, M., Wolde, P. R. t. & Lubensky, D. K. Discrete gene replication events drive coupling between the cell cycle and circadian clocks. *PNAS USA* **113**, 4063-4068 (2015).
91 Danino, T., Mondragón-Palomino, O., Tsimring, L. & Hasty, J. A synchronized quorum of genetic clocks. *Nature* **463**, 326-330, doi:10.1038/nature08753 (2010).
92 Chen, H. & Fink, G. R. Feedback control of morphogenesis in fungi by aromatic alcohols. *Genes & Development* **20**, 1150-1161 (2006).
93 McQuin, C. *et al.* CellProfiler 3.0: Next-generation image processing for biology. *PLOS Biology* **16**, e2005970, doi:10.1371/journal.pbio.2005970 (2018).
94 Judge, M. *et al.* Continuous in vivo metabolism by NMR. *Frontiers in Molecular Biosciences* **6**, doi:10.3389/fmolb.2019.00026 (2019).
95 Lee, K. K., Labiscsak, L., Ahn, C. H. & Hong, C. I. Spiral-based microfluidic device for long-term time course imaging of *Neurospora crassa* with single nucleus resolution. *Fungal Genetics and Biology* **94**, 11-14 (2016).
96 Geng, T. *et al.* Compartmentalized microchannel array for high-throughput analysis of single cell polarized growth and dynamics. *Scientific Reports* **5** (2015).
97 Held, M., Edwards, C. & Nicolau, D. V. Probing the growth dynamics of Neurospora crassa with microfluidic structures. *Fungal Biology* **115**, 493-505, doi:https://doi.org/10.1016/j.funbio.2011.02.003 (2011).
98 Roper, M., Lee, C., Hickey, P. C. & Gladfelter, A. S. Life as a moving fluid: fate of cytoplasmic macromolecules in dynamic fungal syncytia. *Current Opinion in Microbiology* **26**, 116-122, doi:https://doi.org/10.1016/j.mib.2015.07.001 (2015).
99 Brunson, J. K., Griffith, J., Bowles, D., Case, M. E. & Arnold, J. *lac-1* and *lag-1* with *ras-1* affect aging and the biological clock in *Neurospora crassa*. *Ecology and Evolution* **6**, 8341-8351, doi:10.1002/ece3.2554 (2016).
100 Davis, R. H. & de Serres, F. J. [4] Genetic and microbiological research techniques for *Neurospora crassa*. *Methods Enzymol* **17**, 79-143 (1970).
101 Deng, Z. Single-Cell Analysis of the Biological clock Using Microfluidic Droplets. *Ph.D. Dissertation. University of Georgia, Athens, GA*, 31-37 (2017).
102 Marple, S. L. Computing the discrete-time "Analytic" Signal via FFT. *IEEE Transactions* **47**, 2600-2603 (1999).
103 Gould, P. D. *et al.* Coordination of robust single cell rhythms in the Arabidopsis circadian clock via spatial waves of gene expression. *eLife* **7**, e31700, doi:10.7554/eLife.31700 (2018).
104 Grima, B., Chélot, E., Xia, R. & Rouyer, F. Morning and evening peaks of activity rely on different clock neurons of the Drosophila brain. *Nature* **431**, 869-873 (2004).
105 Yamaguchi, S. *et al.* Synchronization of cellular clocks in the suprachiasmatic nucleus. *Science* **302**, 1408-1412 (2003).
106 Dharmananda, S. *Studies of the circadian clock of Neurospora crassa: light-induced phase shifting*. (University of California, 1980).
107 Caranica, C. A.-O., A.; Schuttler, H.-B.; Arnold, J. Identifying a stochastic clock network with light entrainment for single cells of Neurospora crassa. *Nature Scientific Reports* **submitted** (2020).

108 Yang, Q., Pando, B. F., Dong, G., Golden, S. S. & van Oudenaarden, A. Circadian Gating of the Cell Cycle Revealed in Single Cyanobacterial Cells. *Science* **327**, 1522 (2010).
109 Hong, C. I. *et al.* Circadian rhythms synchronize mitosis in Neurospora crassa. *Proceedings of the National Academy of Sciences of the United States of America* **111**, 1397-1402, doi:10.1073/pnas.1319399111 (2014).
110 Arbel-Goren, R. *et al.* Robust, coherent, and synchronized circadian clock-controlled oscillations along Anabaena filaments. *Elife* **10**, e64348 (2021).
111 Caranica, C., Al-Omari, A., Schuttler, H.-B. & Arnold, J. A clock stochastic network with light entrainment is identified for single cells of *Neurospora crassa* by ensemble methods. *PloS one* **submitted** (2019).
112 Mihalcescu, I., Hsing, W. & Leibler, S. Resilient circadian oscillator revealed in individual cyanobacteria. *Nature* **430**, 81, doi:10.1038/nature02533 https://www.nature.com/articles/nature02533#supplementary-information (2004).
113 Bartnicki-Garcia, S., Hergert, F. & Gierz, G. Computer simulation of fungal morphogenesis and the mathematical basis for hyphal (tip) growth. *Protoplasma* **153**, 46-57, doi:10.1007/BF01322464 (1989).
114 Schnepf, A., Roose, T. & Schweiger, P. Growth model for arbuscular mycorrhizal fungi. *Journal of The Royal Society Interface* **5**, 773-784, doi:10.1098/rsif.2007.1250 (2008).
115 Ramos-García, S. L., Roberson, R. W., Freitag, M., Bartnicki-García, S. & Mouriño-Pérez, R. R. Cytoplasmic Bulk Flow Propels Nuclei in Mature Hyphae of <em>Neurospora crassa</em&gt. *Eukaryotic cell* **8**, 1880, doi:10.1128/EC.00062-09 (2009).
116 Judge, M., Griffith, J. & Arnold, J. Aging and the biological clock. *Healthy Aging and Longevity* **Circadian Rhythms and Their Impact on Aging**, 211-234 (2017).
117 Al-Omari, A. M. *et al.* Ensemble Methods for Identifying RNA Operons and Regulons in the Clock Network of Neurospora Crassa. *IEEE Access* **10**, 32510-32524, doi:10.1109/ACCESS.2022.3160481 (2022).
118 Freitag, M., Hickey, P. C., Raju, N. B., Selker, E. U. & Read, N. D. GFP as a tool to analyze the organization, dynamics and function of nuclei and microtubules in Neurospora crassa. *Fungal Genetics and Biology* **41**, 897-910, doi:https://doi.org/10.1016/j.fgb.2004.06.008 (2004).
119 Cheong, J. H. *et al.* The macroscopic limit to synchronization of cellular clocks in single cells of Neurospora crassa. *Sci Rep* **12**, 6750, doi:10.1038/s41598-022-10612-2 (2022).
120 Cheong, J. H. *et al.* The macroscopic limit to synchronization of cellular clocks in single cells of Neurospora crassa. *Scientific Reports* **12**, 6750, doi:10.1038/s41598-022-10612-2 (2022).
121 Deng, Z. *et al.* Single Cells of <italic>Neurospora Crassa</italic> Show Circadian Oscillations, Light Entrainment, Temperature Compensation, and Phase Synchronization. *IEEE Access* **7**, 49403-49417, doi:10.1109/ACCESS.2019.2910731 (2019).
122 Kurosawa, G., Fujioka, A., Koinuma, S., Mochizuki, A. & Shigeyoshi, Y. Temperature-amplitude coupling for stable biological rhythms at different temperatures. *Plos Comput Biol* **13**, doi:ARTN e100550110.1371/journal.pcbi.1005501 (2017).
123 Deng, Z. J. *et al.* Single Cells of Neurospora Crassa Show Circadian Oscillations, Light Entrainment, Temperature Compensation, and Phase Synchronization. *Ieee Access* **7**, 49403-49417, doi:10.1109/Access.2019.2910731 (2019).

124 Hong, C. I. *et al.* Circadian rhythms synchronize mitosis in Neurospora crassa. *Proceedings of the National Academy of Sciences of the United States of America* **111**, 1397-1402, doi:10.1073/pnas.1319399111 (2014).
125 Teng, S. W., Mukherji, S., Moffitt, J. R., de Buyl, S. & O'Shea, E. K. Robust circadian oscillations in growing cyanobacteria require transcriptional feedback. *Science* **340**, 737-740, doi:10.1126/science.1230996 (2013).
126 Lee, K. K., Ahn, C. H. & Hong, C. I. Circadian rhythms in Neurospora crassa on a polydimethylsiloxane microfluidic device for real-time gas perturbations. *Biomicrofluidics* **7**, 44129, doi:10.1063/1.4819478 (2013).
127 Gagliano, O. *et al.* Synchronization between peripheral circadian clock and feeding-fasting cycles in microfluidic device sustains oscillatory pattern of transcriptome. *Nature Communications* **12**, doi:ARTN 618510.1038/s41467-021-26294-9 (2021).
128 Held, M., Kaspar, O., Edwards, C. & Nicolau, D. V. Intracellular mechanisms of fungal space searching in microenvironments. *Proc Natl Acad Sci U S A* **116**, 13543-13552, doi:10.1073/pnas.1816423116 (2019).
129 Fukuda, S. *et al.* Trade-off between Plasticity and Velocity in Mycelial Growth. *Mbio* **12**, doi:ARTN e03196-2010.1128/mBio.03196-20 (2021).
130 Chung, K., Rivet, C. A., Kemp, M. L. & Lu, H. Imaging Single-Cell Signaling Dynamics with a Deterministic High-Density Single-Cell Trap Array. *Analytical Chemistry* **83**, 7044-7052, doi:10.1021/ac2011153 (2011).
131 Duffy, D. C., McDonald, J. C., Schueller, O. J. & Whitesides, G. M. Rapid Prototyping of Microfluidic Systems in Poly(dimethylsiloxane). *Anal Chem* **70**, 4974-4984, doi:10.1021/ac980656z (1998).
132 Sumpter, D. J. T. Collective Animal Behavior. *Princeton University Press, Princeton, NJ* (2010).
133 Cheong, J. H. *et al.* The macroscopic limit to synchronization of cellular clocks in single cells of Neurospora crassa. *Nature Scientific Reports* **12**, 6750 (2022).
134 Giles, N. H. *et al.* Gene organization and regulation in the qa (quinic acid) gene cluster of *Neurospora crassa*. *Microbiological reviews* **49**, 338-358 (1985).
135 Tang, X. *et al.* Systems Biology of the qa Gene Cluster in Neurospora crassa. *PloS one* **6**, e20671, doi:10.1371/journal.pone.0020671 (2011).
136 Giles, N. H. *et al.* Gene organization and regulation in the qa (quinic acid) gene cluster of Neurospora crassa. *Microbiological reviews* **49**, 338-358, doi:10.1128/mr.49.3.338-358.1985 (1985).
137 Kelkar, H. S. *et al.* The Neurospora crassa genome: Cosmid libraries sorted by chromosome. *Genetics* **157**, 979-990 (2001).
138 Patel, V. B., Schweizer, M., Dykstra, C. C., Kushner, S. R. & Giles, N. H. Genetic organization and transcriptional regulation in the qa gene cluster of Neurospora crassa. *Proceedings of the National Academy of Sciences* **78**, 5783-5787, doi:10.1073/pnas.78.9.5783 (1981).
139 Arnett, D. R., Lorimer, H. E. & Asch, D. K. Catabolite repression directly affects transcription of the qa-y gene of Neurospora crassa. *Fungal Genetics and Biology* **46**, 377-380, doi:https://doi.org/10.1016/j.fgb.2009.02.003 (2009).
140 Case, M. E., Geever, R. F. & Asch, D. K. Use of gene replacement transformation to elucidate gene function in the qa gene cluster of Neurospora crassa. *Genetics* **130**, 729-736, doi:10.1093/genetics/130.4.729 (1992).

141 judge, M., Wu, Y., Arnold, J. & Edison, A. S. Uncovering latent metabolic phenotypes in a classic Neurospora mutant using dynamic metabolomics measurements. *Nature* **in preparation** (2022).
142 Case, M. E., Giles, N. H. & Doy, C. H. GENETICAL AND BIOCHEMICAL EVIDENCE FOR FURTHER INTER-RELATIONSHIPS BETWEEN THE POLYAROMATIC SYNTHETIC AND THE QUINATE-SHIKIMATE CATABOLIC PATHWAYS IN NEUROSPORA CRASSA 1. *Genetics* **71**, 337-348, doi:10.1093/genetics/71.3.337 (1972).
143 Dreyfuss, J. M. *et al.* Reconstruction and validation of a genome-scale metabolic model for the filamentous fungus Neurospora crassa using FARM. *Plos Comput Biol* **9**, e1003126-e1003126, doi:10.1371/journal.pcbi.1003126 (2013).
144 Yu, Y. *et al.* A genetic network for the clock of Neurospora crassa. *Proceedings of the National Academy of Sciences of the United States of America* **104**, 2809-2814 (2007).
145 Stajich, J. E. *et al.* FungiDB: an integrated functional genomics database for fungi. *Nucleic Acids Research* **40**, D675-D681, doi:10.1093/nar/gkr918 (2012).
146 Alem, M. A. S., Oteef, M. D. Y., Flowers, T. H. & Douglas, L. J. Production of tyrosol by Candida albicans biofilms and its role in quorum sensing and biofilm development. *Eukaryotic cell* **5**, 1770-1779 (2006).
147 Edison, A. S. *et al.* Metabolomics and Natural-Products Strategies to Study Chemical Ecology in Nematodes. *Integrative and Comparative Biology* **55**, 478-485, doi:10.1093/icb/icv077 (2015).
148 Srinivasan, J. *et al.* A blend of small molecules regulates both mating and development in *Caenorhabditis elegans*. *Nature* **454**, 1115-1118 (2008).
149 Wu, Y., Judge, M. T., Arnold, J., Bhandarkar, S. M. & Edison, A. S. RTExtract: time-series NMR spectra quantification based on 3D surface ridge tracking. *Bioinformatics* **36**, 5068-5075, doi:10.1093/bioinformatics/btaa631 (2020).
150 Wu, Y., Judge, M. T., Edison, A. S. & Arnold, J. Uncovering in vivo biochemical patterns from time-series metabolic dynamics. *PloS one* **17**, e0268394, doi:10.1371/journal.pone.0268394 (2022).
151 Caranica, C. *et al.* What is Phase in Cellular Clocks? *Yale J Biol Med* **92**, 169-178 (2019).

APPENDICES A

Supplementary Materials for

The macroscopic limit to synchronization of cellular clocks in single cells of *Neurospora crassa*

**Table S1.1** The rate constants for the quorum sensing (column 3) are similar to isolated single cells[1] (column 2) and those at the macroscopic limit of $10^7$cells per ml[2] (column 4)

| **Parameter** | **Initial Parameter values from published ensemble (column 4) computed by Parallel tempering for D/D experiment[1]** | **Best parameter values from model ensemble computed by microwell D/D experiment under quorum sensing model** | **Initial Parameter values from published ensemble (column 3) computed by Parallel tempering for D/D experiment[2]** |
|---|---|---|---|
| Number of communicating cells | 1 | 240 | ~$10^7$ cells/ml |
| A | 2.56E−10 | 6.852861E-03 | 0.0313 |
| Ā | 1.589532708 | 1.013056E-01 | 0.1108 |
| S1 | 80.12566921 | 3.352361E+01 | 0.000420 |
| S3 | 0.400641074 | 1.708023E-03 | 5.47E-5 |
| S4 | 8,316.020583 | 1.932607E+01 | 1.252 |
| D1 | 1.294999006 | 1.195490E+00 | 6.607 |
| D3 | 4.382612039 | 1.855057E+00 | 0.798 |
| C1 | 0.000932789 | 1.685434E-03 | 1.047 |

| | | | |
|---|---|---|---|
| L1 | 4.777735371 | 4.268960E+01 | 94.39 |
| L3 | 0.665600817 | 5.283324E+00 | 63.93 |
| D4 | 0.08474029 | 5.428893E-01 | 0.00451 |
| D6 | 0.193685712 | 5.775316E-01 | 0.205 |
| D7 | 2.130911791 | 4.301660E-02 | 0.135 |
| D8 | 0.007744621 | 6.586861E-05 | 0.0122 |
| C2 | 1.515554675 | 3.583455E+00 | 3.322 |
| P | 2.72E−09 | 9.845228E+01 | 0.2233 |
| $A_c$ | 1.86E−08 | 1.109814E+01 | 0.1293 |
| $B_c$ | 2.581096866 | 9.345902E-01 | 0.6091 |
| $S_c$ | 61.51499414 | 1.458434E-03 | 2.572 |
| $L_c$ | 1.61524392 | 1.256038E-08 | 3.664 |
| $D_{cr}$ | 0.150810052 | 6.049845E+01 | 0.579 |
| $D_{cp}$ | 0.54063952 | 3.940957E-01 | 0.5536 |
| $K_{S1}$ | -- | 4.612788E+09 | -- |
| C4 | -- | 2.646258E+00 | -- |
| $\eta$ | -- | 1.445784E-05 | -- |
| $\eta_{ext}$ | -- | 4.094524E-01 | -- |
| D9 | -- | 2.150455E+01 | -- |
| D10 | -- | 3.057320E-08 | -- |

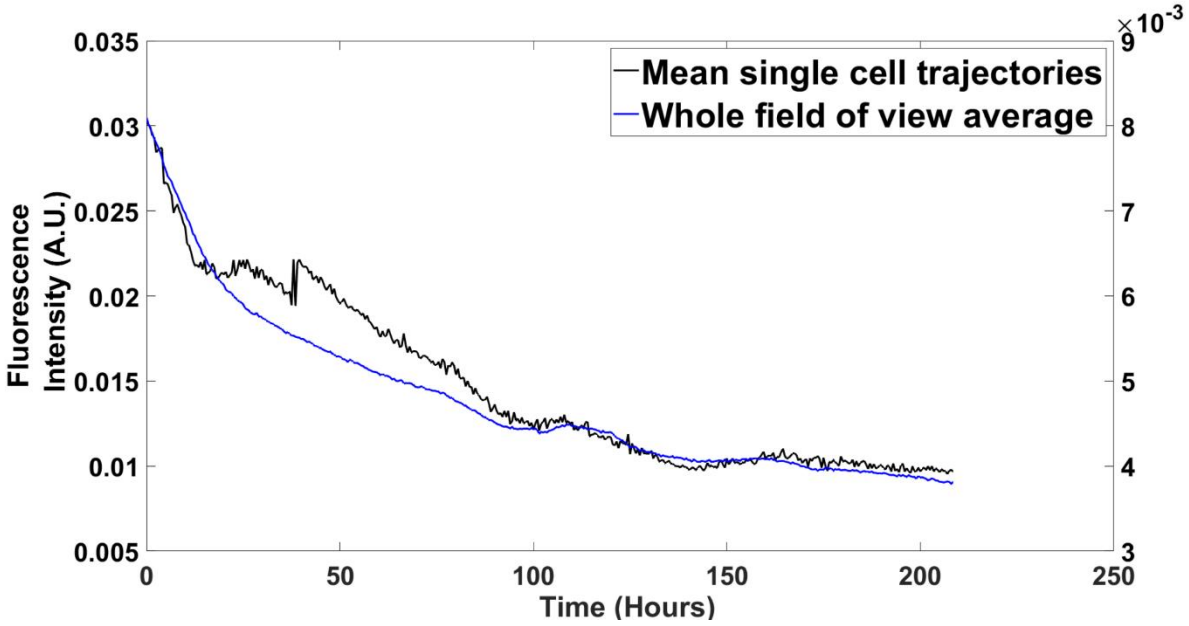


**Fig. S1.1** Mean single cell trajectories from the chamber microfluidic device tracked the whole field of view average intensity very well. **The plots were created in MATLAB_R2020B (**https://www.mathworks.com/products/matlab.html).

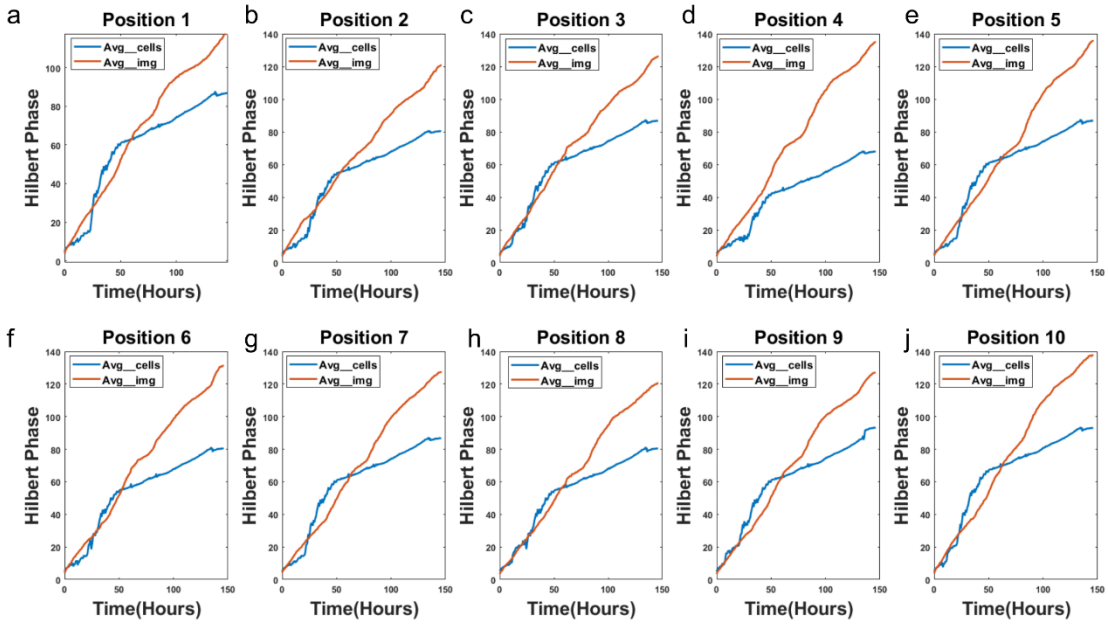


**Fig. S1.2** Average Phase of single cells tracks phase of a field of view across 10 fields of view in the big chamber device. The strain is MFNC9 (see Materials and Methods). Cells were grown in media 5 (see Materials and Methods) to block cell division. Fluorescence was measured every half hour over 10 days. **The plots were created in MATLAB_R2020B (**https://www.mathworks.com/products/matlab.html).

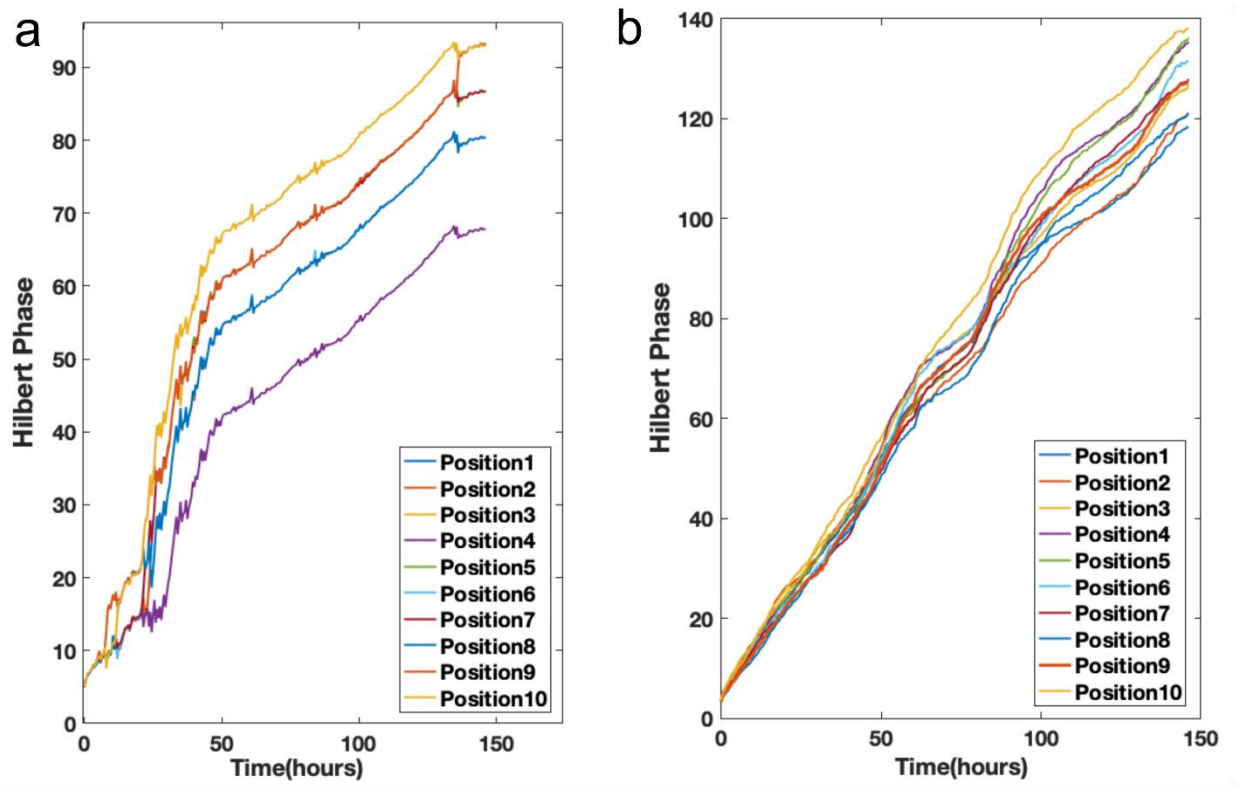


**Fig. S1.3** While the phase curves do track each other, they also fan out over time. The Hilbert phase curves from single cell trajectories were computed as described earlier[62]. (A) average of image (B) average of cells tracked. Single cell tracking was done with CellProfiler[93]. **The plots were created in MATLAB_R2020B (**https://www.mathworks.com/products/matlab.html).

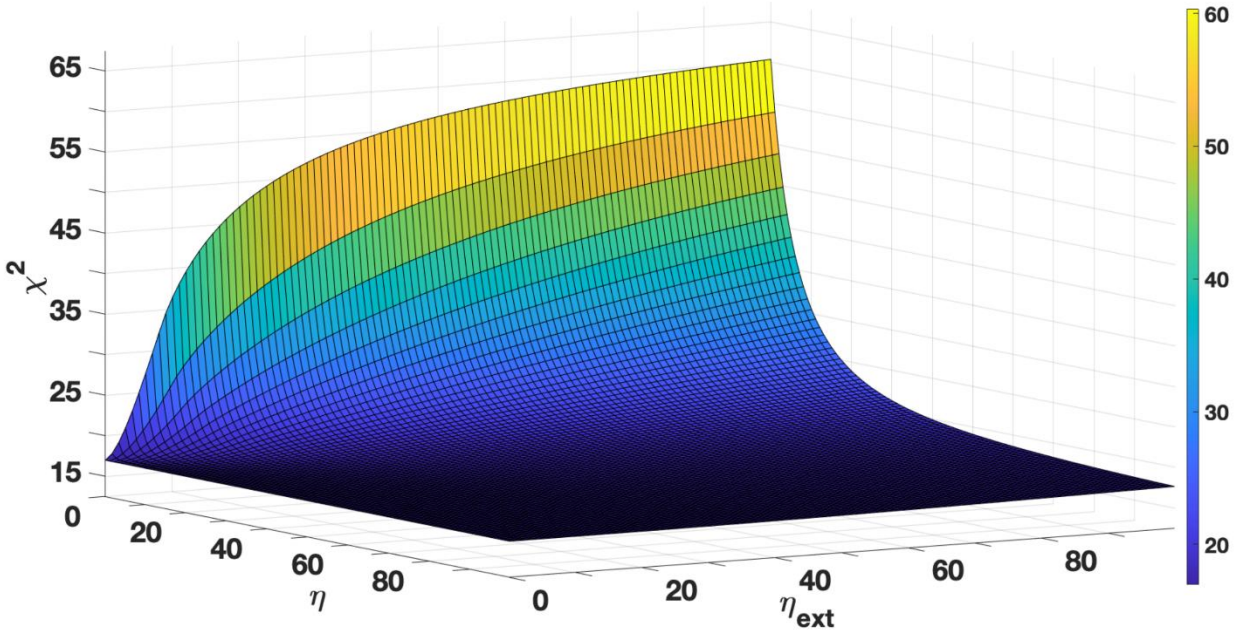


**Fig. S1.4** There is limited information about the diffusion parameters ($\eta$ and $\eta_{ext}$) for communication under the quorum sensing model as indicated by the chi-squared statistic surface as a function of $\eta$ and $\eta_{ext}$. For example, the surface is nearly flat with respect to $\eta_{ext}$. There is more information about $\eta$ – the surface increases sharply for $\eta_{ext}$around ~20 or below. Other parameters are set at their best values with respect to the chi-squared statistic in supplement Table S1. **The plots were created in MATLAB_R2020B (**https://www.mathworks.com/products/matlab.html).

APPENDICES B

Supplementary Materials for

The clock in growing hyphae and their synchronization in *Neurospora crassa*

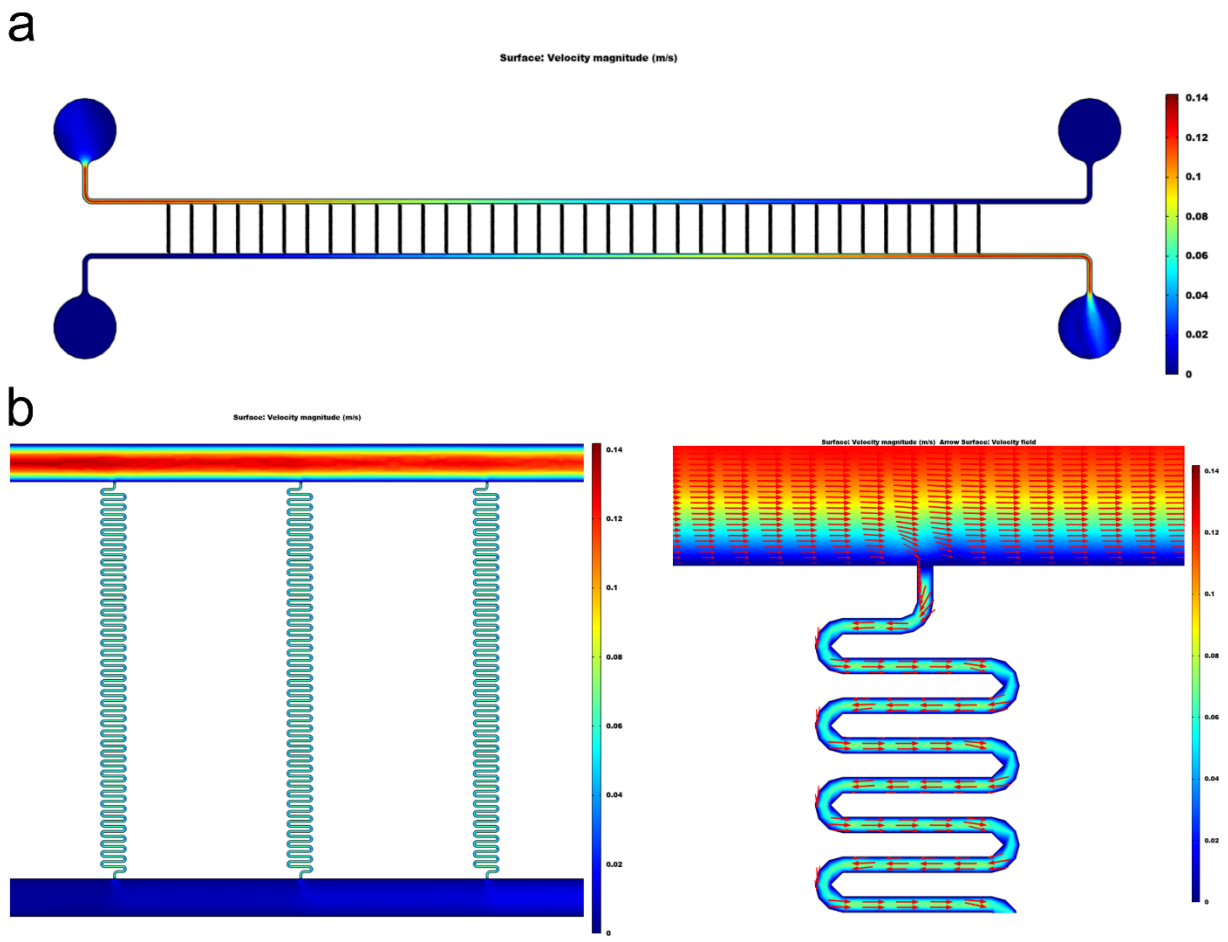


**Figure S2.1**. Numerical simulation of flow profiles within the channels using COMSOL Multiphysics software. (**a**) Simulated velocity flow profile in the whole serpentine chip shows constant flow of media. The right panel- color bar indicates the velocity. (**b**) (Left) Magnified image of the simulated velocity flow profile in random selected serpentine channels. Flow is

present in the serpentine channel. (Right) Magnified image of the velocity profile at the sepentine inlet closest to the media flow.

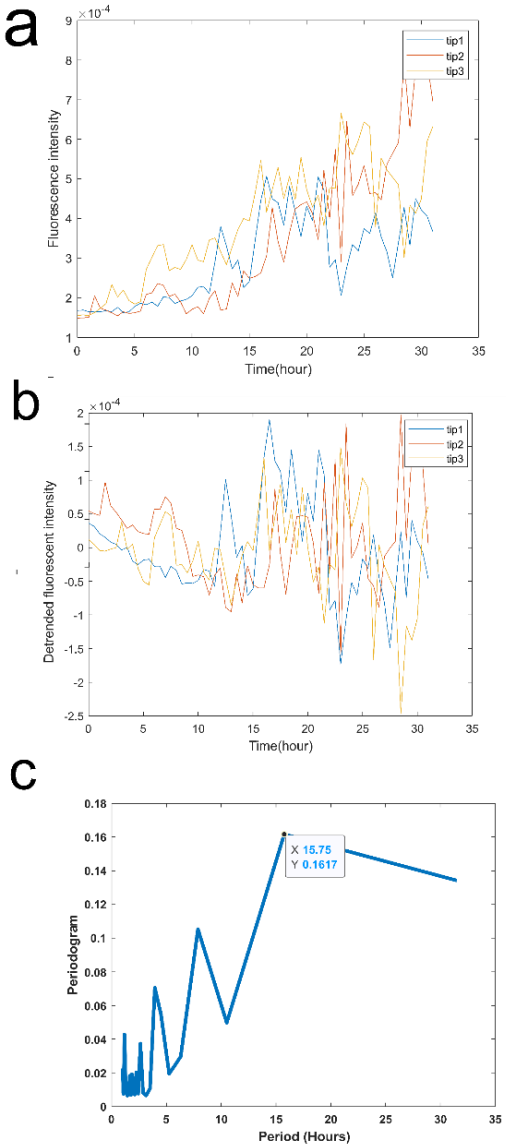


**Figure S2.2**. Fluorescence trajectories of three individual hyphal tips tracked. (**a**) Raw fluorescence trajectories of hyphal tip tracked over a period of 30 hours. (**b**) Detrended fluorescence trajectories of hyphal trip tracked.(**c**) The average periodogram of hyphal tips present a period of 15.75 hours.

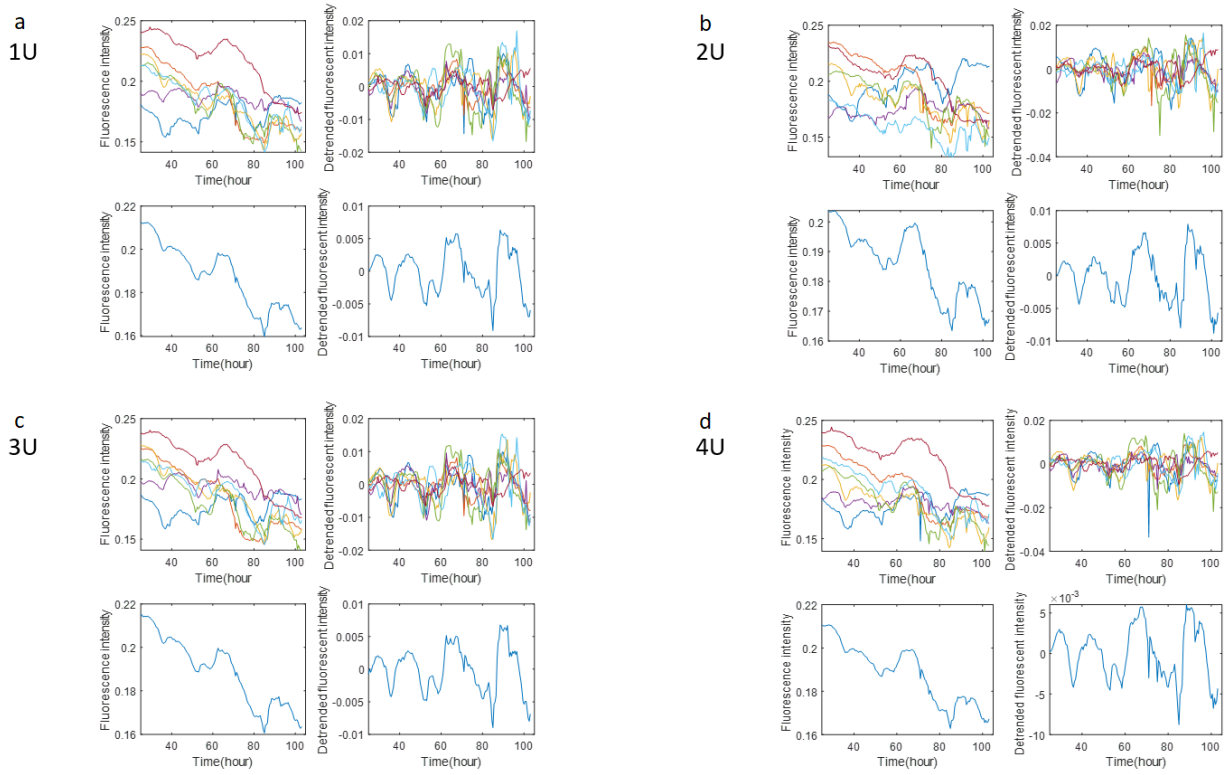


**Figure S2.3**. Fluorescence trajectories of seven individual segments of hyphae in serpentine channels. (**a-d**) Top left graph show raw fluorescence trajectories of seven individual segments while the top right graph is the detrended trajectories that were carried out with a 24-hour detrending window. The bottom left graph is the average raw fluorescence trajectories while the bottom right graph is the average detrended trajectories. The corresponsing number of U-turns tracked for each graph is labelled in the image.

a

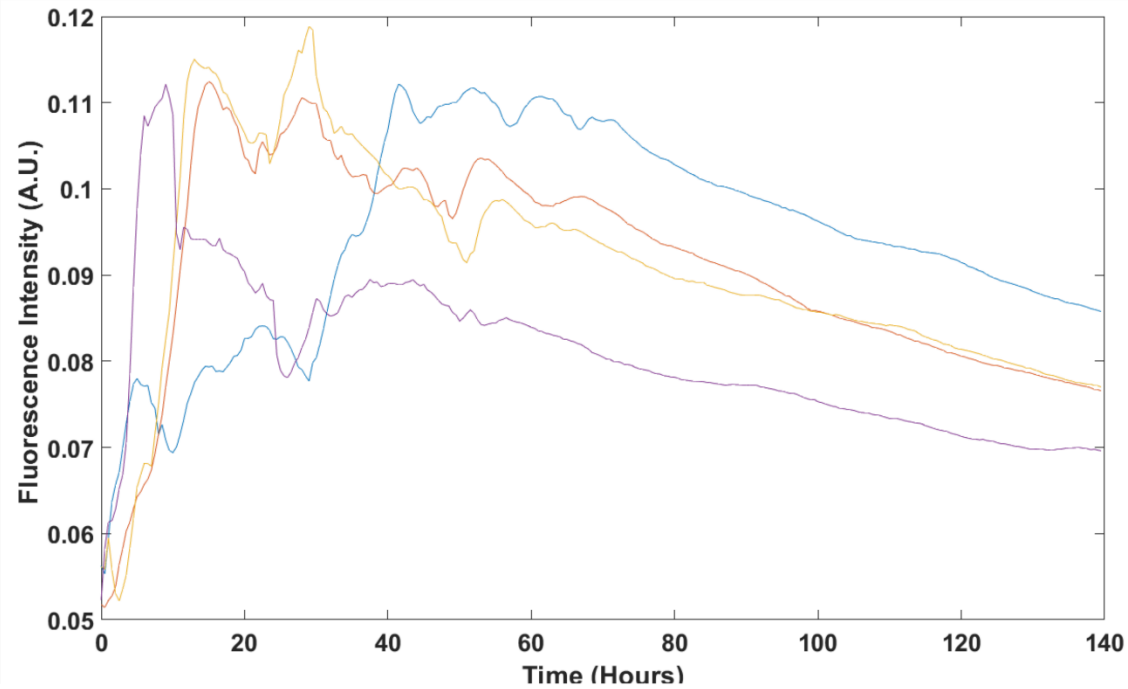
0.12
0.11
0.1
0.09
0.08
0.07
0.06
0.05
Fluorescence Intensity (A.U.)
0
20
40
60
80
100
120
140
Time (Hours)

b

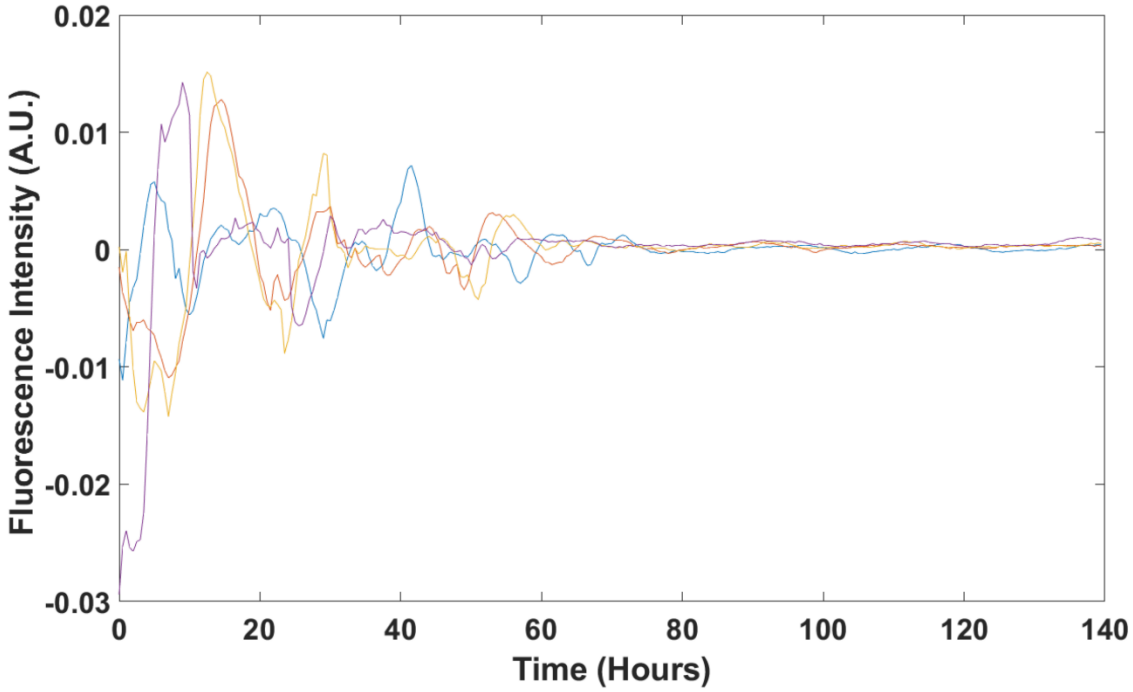
0.02
0.01
0
-0.01
-0.02
-0.03
Fluorescence Intensity (A.U.)
0
20
40
60
80
100
120
140
Time (Hours)

**Figure S2.4**. Fluorescence trajectories of four individual of hyphae in serpentine channels. (**a**) Raw fluoresence tracjectories of individual hypha growing in the channel (b) Detrended fluorescnece trajectories of four individual hyphae with a 24-hour detrending window.


**Figure S2.5.** Image of luminescence band in a race tube[4]. Numbers labeled in the image correspond to the bands tracked over time in **Fig 2.6**.


**Figure S2.6.** Image of the segment (segment 2) consisting of six serpentine channels tracked to calculate Kuramoto K values in **Table 2.2.**

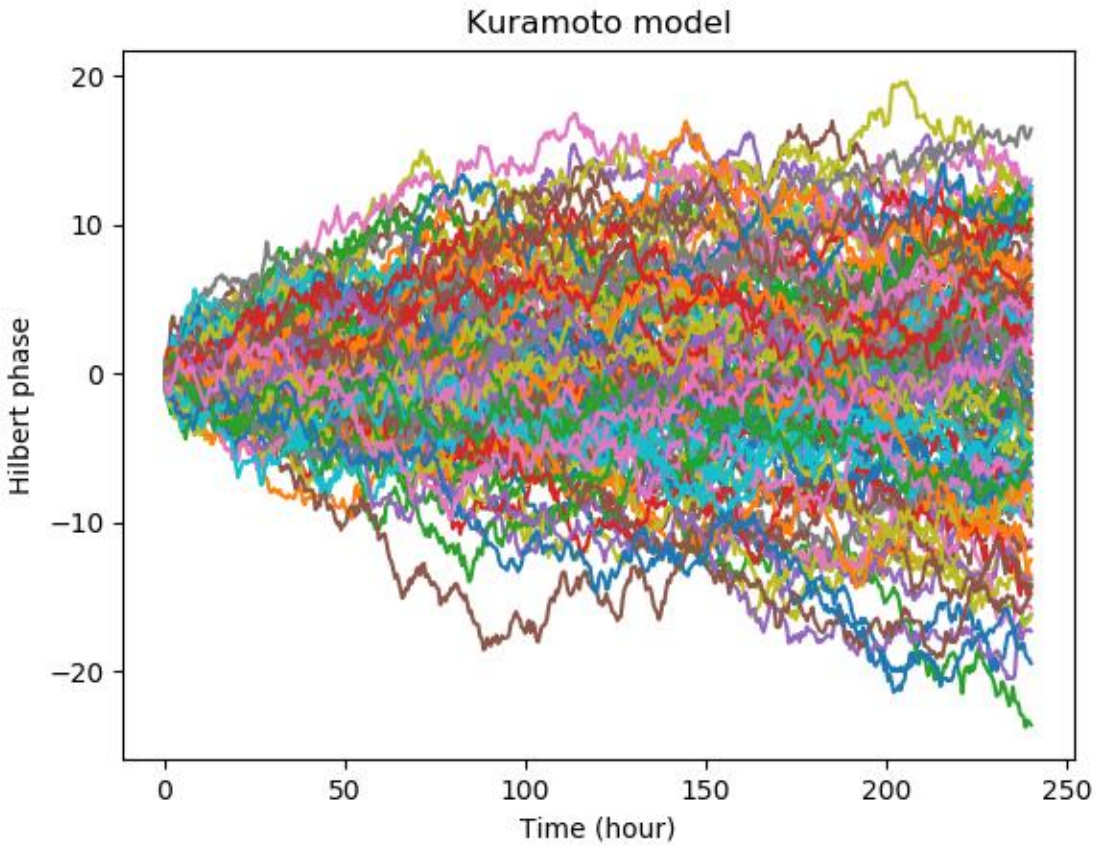


**Figure S2.7.** Hilbert phase[151] of 127 trajectories of generated white noise for a period of 240h. Hilbert phase was plotted to calculate the Kuramoto (K) number.

APPENDICES C

Supplementary Materials for

*In vivo* metabolomic and RNA profiling data support an aromatic alcohol as a quorum sensing signal for phase synchronization of the clock in single cells of *Neurospora crassa*

**Table S3.1** The rate coefficients of the quorum sensing model as null hypothesis are tabulated. Ensemble means and ensemble standard errors are reported for each rate coefficient in **Fig. 3.1**. The means and standard errors are computed from the accumulation run of the Monte Carlo Experiment.

| qa cluster genes | | | QA metabolic pathway | | |
|---|---|---|---|---|---|
| reaction coefficient | mean | standard error | reaction coefficient | mean | standard error |
| P1 | 4.92E-19 | 5.56E-36 | C1 | 2.39E-17 | 1.17E-17 |
| P2 | 5.27E-16 | 0.00E+00 | C2 | 1.75E-16 | 4.33E-17 |
| Af | 5.25E-01 | 0.00E+00 | C3 | 3.46E-16 | 1.54E-16 |
| Afbar | 8.07E+00 | 0.00E+00 | C4 | 6.79E-03 | 6.20E-05 |
| Bf | 8.17E+00 | 0.00E+00 | C5 | 1.93E-24 | 3.54E-25 |
| Sf | 2.41E+01 | 0.00E+00 | C6 | 1.46E-19 | 4.28E-20 |
| Sfw | 1.17E-22 | 1.36E-39 | C7 | 2.89E-29 | 9.40E-30 |
| Lf | 1.29E+00 | 1.28E-17 | C8 | 5.75E-05 | 1.04E-05 |
| As | 1.65E-01 | 1.60E-18 | C9 | 1.71E-33 | 3.38E-34 |

| | | | | | |
|---|---|---|---|---|---|
| Asbar | 3.56E-20 | 3.48E-37 | C10 | 2.78E-10 | 4.97E-11 |
| Bs | 2.13E-17 | 0.00E+00 | C11 | 6.24E-17 | 2.16E-17 |
| Ss | 1.84E+01 | 0.00E+00 | C12 | 1.49E-11 | 4.15E-12 |
| Ssw | 2.92E-21 | 2.17E-38 | C13 | 2.60E-04 | 3.88E-07 |
| Ls | 2.89E+00 | 5.13E-17 | C14 | 7.25E-03 | 2.06E-05 |
| Ay | 7.25E-01 | 1.28E-17 | C15 | 2.38E-02 | 2.01E-04 |
| A3 | 6.26E-20 | 0.00E+00 | C16 | 2.25E-03 | 1.91E-04 |
| A2 | 1.11E-22 | 1.36E-39 | C17 | 1.77E-07 | 4.38E-08 |
| A4 | 1.97E-21 | 0.00E+00 | C18 | 4.13E-10 | 8.01E-11 |
| Ax | 1.28E-20 | 1.74E-37 | C19 | 6.09E-02 | 4.74E-05 |
| Aybar | 1.16E-23 | 1.70E-40 | C20 | 2.70E-16 | 7.29E-17 |
| A3bar | 5.30E-01 | 0.00E+00 | C21 | 7.29E-01 | 2.27E-04 |
| A2bar | 7.33E-01 | 6.41E-18 | C22 | 5.81E-04 | 4.78E-07 |
| A4bar | 4.72E+00 | 1.03E-16 | C23 | 8.74E-11 | 3.08E-11 |
| Axbar | 4.88E+00 | 5.13E-17 | C24 | 1.70E-01 | 2.73E-04 |
| By | 2.49E+01 | 4.10E-16 | C25 | 7.80E-04 | 1.67E-04 |
| B3 | 2.80E+00 | 2.56E-17 | C26 | 6.99E-03 | 1.41E-03 |
| B2 | 3.29E+00 | 2.56E-17 | C27 | 2.32E-05 | 5.16E-08 |
| B4 | 1.70E+00 | 1.28E-17 | C28 | 3.31E-17 | 5.27E-18 |
| Bx | 1.66E+01 | 0.00E+00 | C29 | 2.45E-22 | 7.53E-23 |
| Sy | 6.20E+01 | 0.00E+00 | C30 | 3.60E-02 | 4.01E-19 |
| S3 | 1.49E+03 | 0.00E+00 | C31 | 7.59E-02 | 6.49E-03 |

| | | | | | |
|---|---|---|---|---|---|
| S2 | 1.76E+01 | 2.05E-16 | C32 | 3.01E-19 | 8.09E-20 |
| S4 | 2.21E+02 | 1.64E-15 | C33 | 3.42E-02 | 1.43E-04 |
| Sx | 2.65E+02 | 0.00E+00 | C34 | 7.56E-21 | 1.26E-21 |
| Syw | 5.14E-21 | 4.34E-38 | C35 | 6.63E-04 | 3.23E-06 |
| S3w | 6.37E-21 | 0.00E+00 | C36 | 9.63E-21 | 2.02E-21 |
| S2w | 2.79E-17 | 0.00E+00 | C37 | 2.67E-05 | 8.05E-06 |
| S4w | 2.52E-22 | 0.00E+00 | C38 | 2.69E-16 | 1.02E-16 |
| Sxw | 1.47E-20 | 1.74E-37 | C39 | 1.62E-26 | 8.00E-27 |
| Ly | 3.44E-20 | 3.48E-37 | C40 | 6.17E-03 | 5.46E-04 |
| L3 | 3.26E-20 | 3.48E-37 | C41 | 7.10E-04 | 1.23E-05 |
| L2 | 2.57E-19 | 0.00E+00 | C42 | 5.74E-02 | 3.11E-05 |
| L4 | 1.76E-21 | 0.00E+00 | | | |
| Lx | 1.23E-21 | 1.09E-38 | | | |
| D1 | 2.31E+00 | 3.60E-05 | | | |
| D2 | 3.68E+00 | 4.61E-04 | | | |
| D3 | 3.81E-32 | 8.48E-33 | | | |
| D4 | 6.81E+00 | 1.54E-16 | | | |
| D5 | 2.02E-15 | 4.38E-16 | | | |
| D6 | 2.33E+00 | 5.55E-04 | | | |
| D7 | 2.96E-34 | 6.99E-35 | | | |
| D8 | 7.73E+01 | 2.42E-02 | | | |
| D9 | 7.00E-42 | 2.80E-42 | | | |

| | | | | | |
|---|---|---|---|---|---|
| D10 | 2.01E+00 | 1.98E-04 | | | |
| D11 | 9.46E-35 | 1.64E-35 | | | |
| D12 | 2.19E+00 | 7.83E-04 | | | |
| D13 | 6.29E-37 | 1.42E-37 | | | |
| D14 | 4.12E+00 | 2.15E-03 | | | |
| D15 | 4.86E-35 | 1.61E-35 | | | |
| D20 | 2.49E-18 | 5.81E-19 | | | |

| quorum sensing regulation | | | TCA cycle | | |
|---|---|---|---|---|---|
| reaction coefficient | mean | standard error | reaction coefficient | mean | standard error |
| eta | 2.39E-20 | 7.03E-21 | T1 | 7.59E-02 | 9.24E-06 |
| etaext | 7.52E-25 | 1.53E-25 | T2 | 5.51E-02 | 4.01E-19 |
| adh | 7.66E+01 | 8.72E-02 | T3 | 5.34E-02 | 7.57E-05 |
| AN | 2.45E-21 | 6.89E-22 | T4 | 2.25E-03 | 4.08E-05 |
| ANbar | 4.36E-24 | 9.04E-25 | T5 | 0.00E+00 | 0.00E+00 |
| BN | 8.88E-24 | 2.74E-24 | T6 | 3.71E+00 | 4.64E-03 |
| SN | 4.14E-13 | 1.44E-13 | T7 | 4.63E-03 | 3.62E-06 |
| SNw | 1.86E-27 | 4.02E-28 | T8 | 0.00E+00 | 0.00E+00 |
| LN | 6.07E-27 | 1.79E-27 | T9 | 4.30E-04 | 1.28E-06 |
| R1 | 1.60E-18 | 3.23E-19 | T10 | 8.81E-03 | 3.15E-06 |
| R2 | 4.67E-03 | 2.34E-05 | | | |

| | | | | | |
|---|---|---|---|---|---|
| R3 | 3.99E-01 | 4.17E-04 | | | |
| R4 | 6.18E-04 | 7.32E-07 | | | |
| R5 | 1.53E-03 | 1.46E-06 | | | |
| R6 | 3.13E+00 | 8.04E-04 | | | |
| R7 | 1.80E-17 | 8.73E-18 | | | |
| R8 | 1.37E-24 | 5.52E-25 | | | |
| R9 | 8.29E-03 | 1.00E-19 | | | |
| R10 | 8.62E-03 | 2.83E-07 | | | |
| R11 | 7.63E-02 | 5.91E-05 | | | |
| D16 | 2.96E-02 | 1.45E-05 | | | |
| D17 | 1.07E-24 | 3.89E-25 | | | |
| D18 | 2.16E-19 | 4.13E-20 | | | |
| D19 | 1.39E-13 | 3.15E-14 | | | |
| D21 | 7.99E-22 | 1.88E-22 | | | |

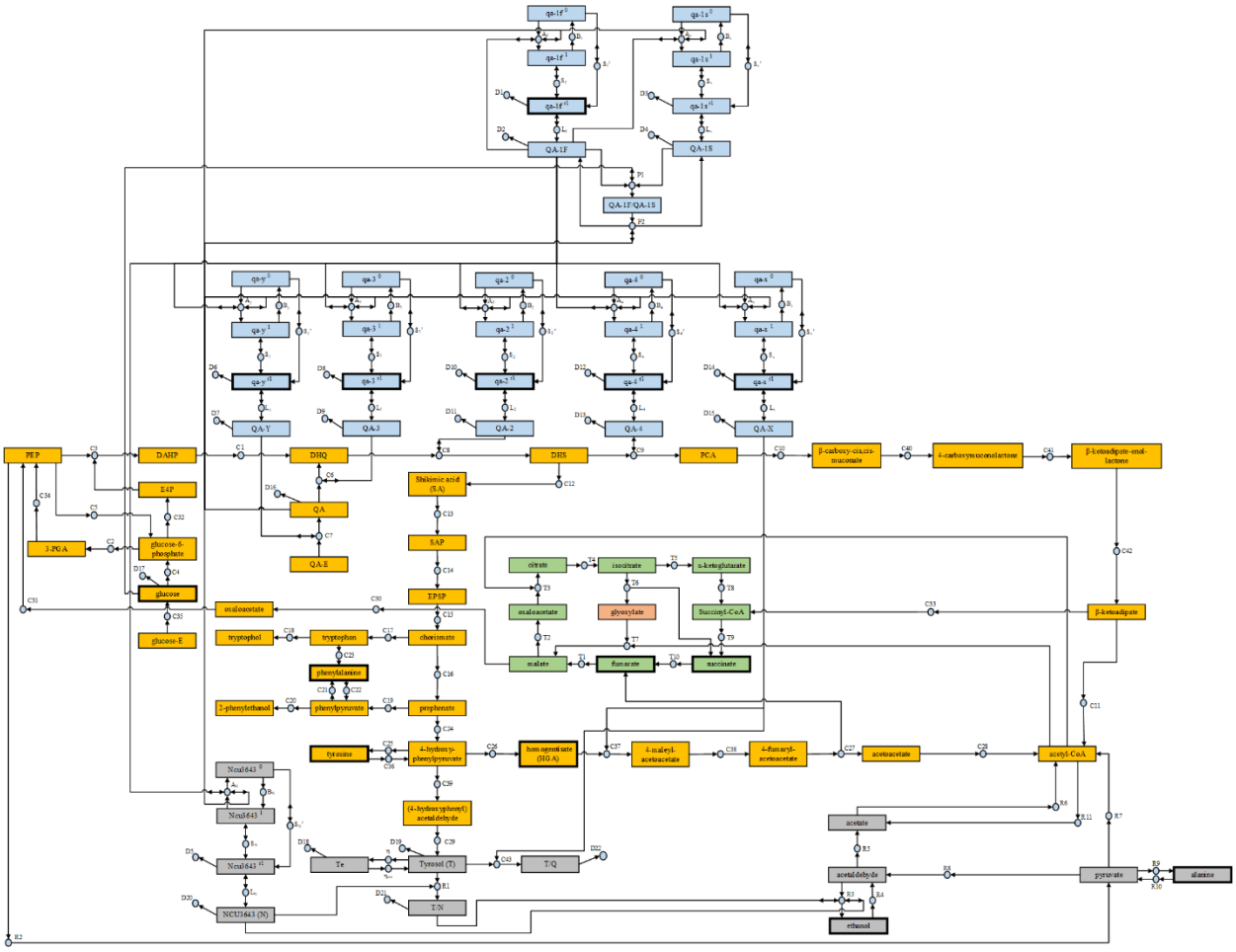


Fig S3.1. Metabolic model with QA-X as a regulator

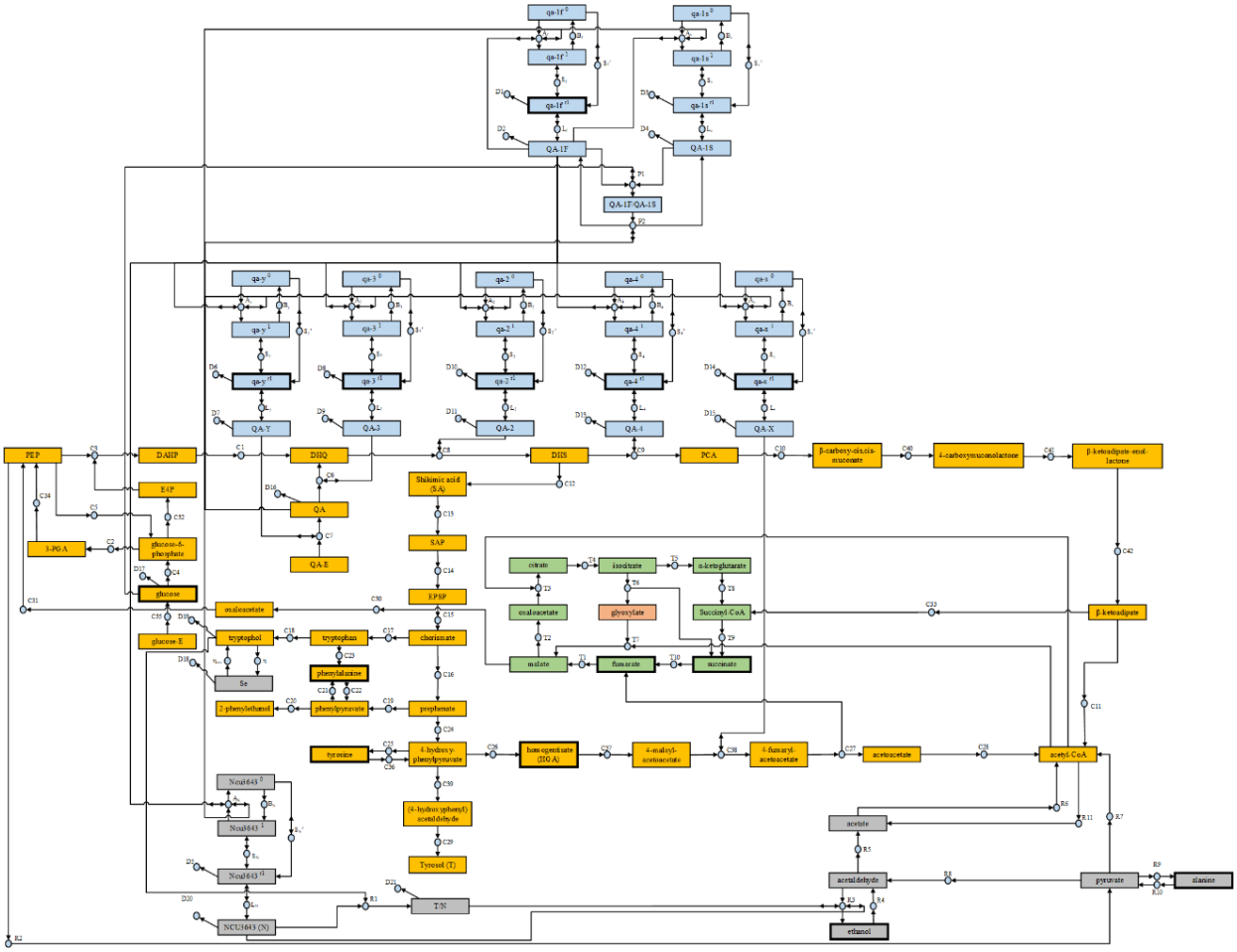


Fig S3.2. Metabolic model with phenylethanol as signaling molecule

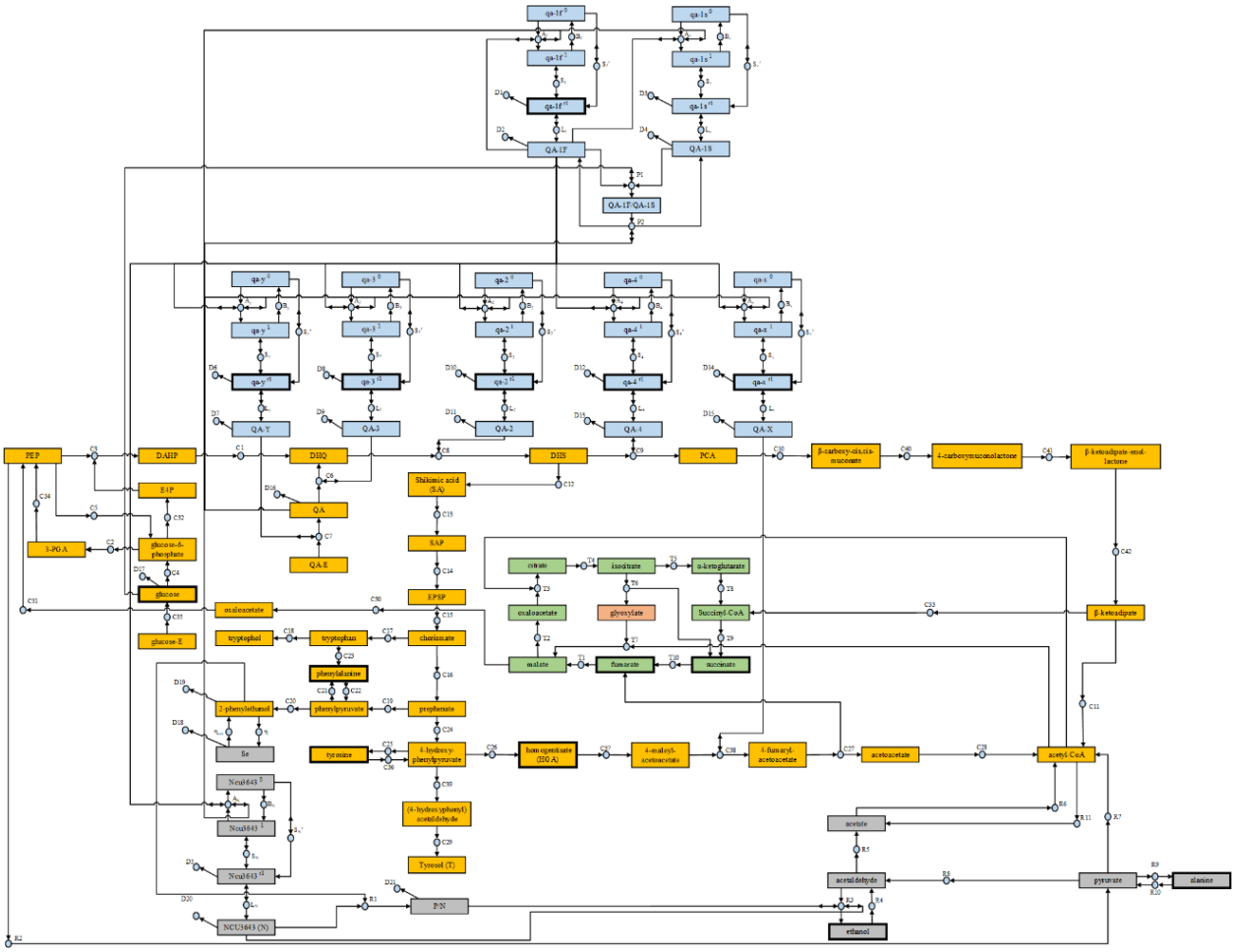


Fig S3.3. Metabolic model with tryptophol as signaling molecule

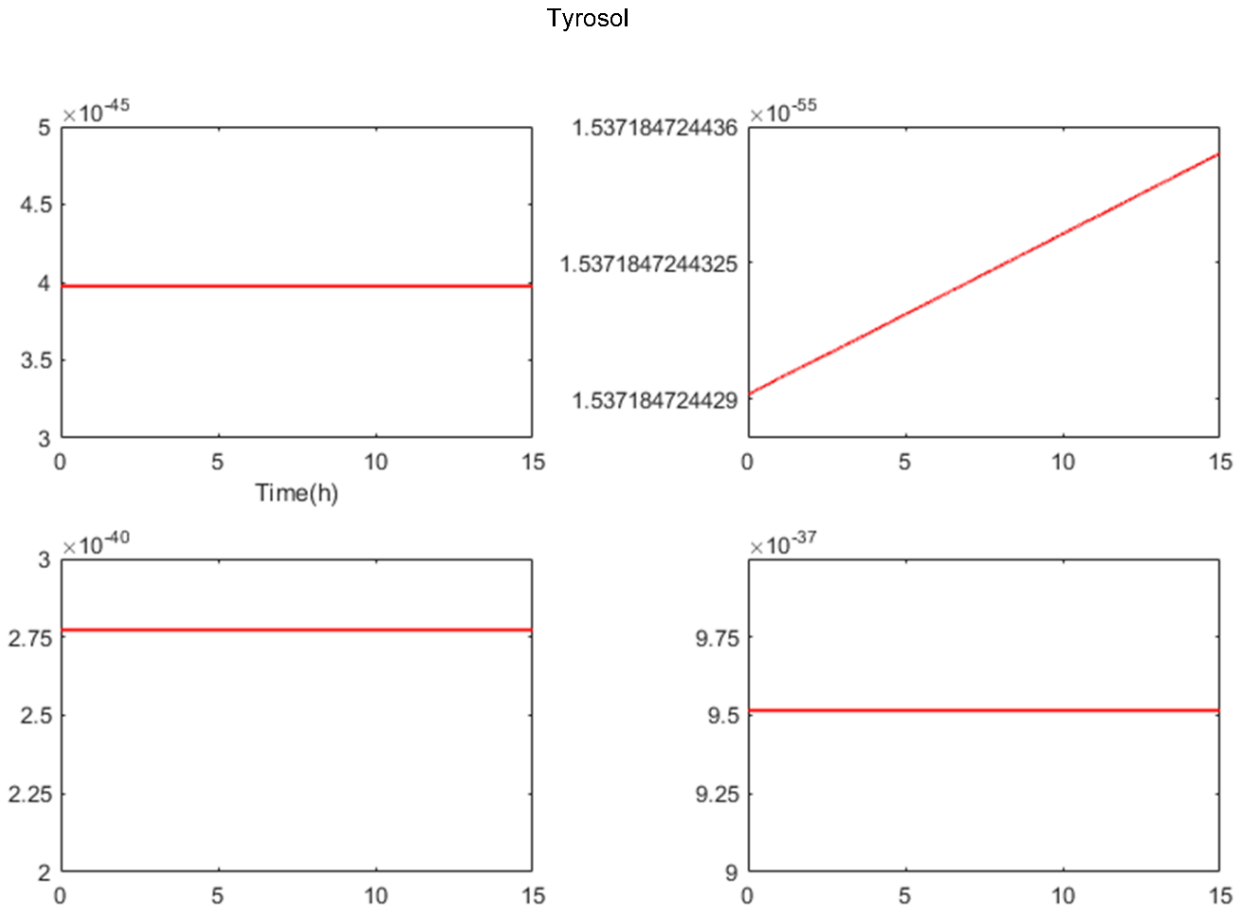


Fig S3.4. Ensemble simulation for Tyrosol.